Fall 2018

Numerical Modeling of Submarine Minibasin Flow and Morphodynamics

Elena Bastianon

NUMERICAL MODELING OF SUBMARINE MINIBASIN FLOW AND MORPHODYNAMICS

by

Elena Bastianon

Bachelor of Engineering
University of Trento, 2008

Master of Engineering
University of Trento, 2012

Submitted in Partial Fulfillment of the Requirements

For the Degree of Doctor of Philosophy in

Civil Engineering

College of Engineering and Computing

University of South Carolina

2018

Accepted by:

Jasim Imran, Major Professor

Enrica Viparelli, Major Professor

M. Hanif Chaudhry, Committee Member

Alessandro Cantelli, Committee Member

Cheryl L. Addy, Vice Provost and Dean of the Graduate School

DEDICATION

To my family and Chris.

ACKNOWLEDGEMENTS

I would like to gratefully acknowledge a number of people who have journeyed with me over the years and without whose support this thesis would not have been complete. First, I am extremely grateful to my advisors Jasim Imran and Enrica Viparelli, for giving me the opportunity to do a Ph.D., sharing their time and knowledge, and for helping me in so many ways throughout this path. Special thanks to my committee members: M. Hanif Chaudhry and Alessandro Cantelli for their suggestions and discussions during my studies. A special thanks to Enrica Viparelli for guiding me in periods of crisis.

This adventure wouldn't have been possible without the support of my friends here in South Carolina and elsewhere, and all the Water Resources Group at the University of South Carolina. I would like to thank my family for always standing by me even though they live thousands of kilometers away. I thank my sisters and my nephew, for cheering me up. I would like to deeply thank my parents for their support. My deepest gratitude to Chris for being always by my side and making me smile every day.

ABSTRACT

Intraslope basins, or minibasins, are important morphological features of the continental slope in both modern and ancient sedimentary systems. Minibasins have an elliptical or spherical shape with a steep inlet or proximal zone followed by an almost horizontal basin floor, and an overflow zone near the downstream basin lip. These basins are filled with sediment transported by successive events of turbidity currents and other types of submarine flows. The work presented here focuses on turbidity current sedimentation in intraslope minibasins, which is often described in terms of the 'fill-and-spill' conceptual model. The 'fill-and-spill' model has been used previously to describe the process by which the minibasins are filled creating sand rich deposits that constitute prime targets for hydrocarbon exploration. The objective of this study is to understand how the shape and the grain size distribution of the deposit changes with the characteristics of the turbidity current and the morphology of the basin-floor topography of the area. The flow characteristics, i.e., velocity and concentration in both the vertical and longitudinal directions, and the grain size distribution of the deposit are investigated at the laboratory and field scale in two and three dimensions. A stratigraphic model was implemented within a 3D numerical modeling system of turbidity currents by accounting for storage and access to the grain size distribution of the deposit. A Morphological Acceleration Factor (MORFAC) for morphodynamic upscaling was also implemented to reduce computational

costs. The model was validated at laboratory scale against available 2D and 3D data from experiments conducted in constant width flumes and 3D minibasins. The model prediction showed a satisfactory agreement between measured and simulated deposit geometries, vertical profiles of suspended sediment concentration and spatial distributions of sediment sizes in the deposit. The field-scale application involving the present seafloor bathymetry of the Brazos-Trinity system in the Gulf of Mexico showed that deposition in intraslope minibasins varies depending on the current magnitude and duration, and the geometric configuration. The field-scale simulations were performed on two linked minibasins. Most of the sediment deposited in the upstream basin and the rest was transported to the downstream basin through submarine canyons. The deposition in the downstream basin was characterized by current reflection of the downstream flank and preferential deposition of sediment in the proximal and central parts of the basin. Model runs conducted to study the effect of MORFAC demonstrated small values of MORFAC from two to five could capture bed evolution and stratigraphic architecture of the deposit, while large values of MORFAC could only capture the overall trend of the deposition process. Thus, caution should be exercised in the choice of the proper MORFAC value.

TABLE OF CONTENTS

LIST OF TABLES

LIST OF FIGURES

CHAPTER 1

INTRODUCTION

Turbidity currents are a class of sediment gravity flows where turbulence is the dominant mechanism for grain support. They are sediment-laden underflows characterized by higher sediment concentration compared with the ambient water. Turbidity currents play an important role in moving coarse and fine-grained material from the margins to the deep part of oceans (Bouma, 1981; Bouma, 1982; Normark et al., 1993; Kneller and Buckee, 2000), and they are responsible for a range of morphological features on the seabed. For example turbidity currents are responsible for carving deep submarine canyons, carrying sediments far into the ocean and reservoirs, forming expansive submarine fans by silicoclastic sediment deposition. As they decelerate, the turbidity currents leave deposits characterized by a predictable geometry and internal structure (e.g., Bouma 1962; Lowe 1982; Mutti 1992). For these reasons, turbidity currents are of interest to geologists and oceanographers as well as civil, petroleum and ocean engineers.

Turbidity currents on the continental slope of the Gulf of Mexico have created interesting morphological and stratigraphic records. As turbidity currents move into the deep ocean they can meet counter or lateral slopes (e.g., Kneller et al. 1991; Haughton 1994; Winker 1996; Sinclair 2000; Al Ja'Aidi et al. 2004; Amy et al. 2004; Jobe et al.

2012), and when the topography is of the same scale or more significant than the current thickness it interacts with it (Bursik and Woods 2000; Alexander and Morris 1994, Van Andel and Komar 1969). A distinct aspect of deep-water sedimentation in the Brazos-Trinity depositional system located offshore Texas (e.g., Suter and Berryhill, 1985; Winker, 1996; Beaubouef and Friedmann, 2000), is the presence of intraslope minibasins or basins (Bryant et al., 1990; Bouma and Bryant, 1994; Diegel et al., 1995) that have trapped thick sediment layers, some of which contain sand bodies with excellent hydrocarbon reservoir properties (Mahaffie 1994; Holman and Robertson 1994; Badalini et al. 2000).

Minibasins in the Gulf of Mexico

The Brazos-Trinity system is a point-source, linked series of intraslope minibasins, late Pleistocene sediment gravity flow depositional system (Suter and Berryhill, 1985; Abdulah, 1995; Anderson et al., 1996; Winker, 1996). The system is located between 150 and 1,450 m water depth, and it consists of onlap-fill successions in three minibasins (Basin I, II and IV) and a graben (Basin III). A deeply incised channel connects Basin I with Basin II and III (Winker, 1996; Beaubouef and Friedmann, 2000; Pirmez et al., 2000). The updip basins (I-III) are filled to the spill point, whereas the most downdip (IV) is still underfilled. Basin II is located 20 km downstream of Basin I with water depth ranges between 660 m and 993 m (Satterfield and Behrens, 1990; Winker, 1996; Beaubouef et al., 1998; Badalini et al., 2000; Beaubouef and Friedmann, 2000; Beaubouef and Abreu, 2006). Basin III, a graben, with water depth ranges between 892 m and 1,267 m, is located east of Basin II, and it captured the drainage from Basin II during the formation of the eastern channel connecting Basin II with Basin IV (Winker, 1996; Badalini et al., 2000; Beaubouef and

Friedmann, 2000). The morphology of the eastern channel changes rapidly as it enters the basin to a complex of low-relief channels; and a western channel, shallow and with rough topography, connects the distal part of Basin II to the proximal part of Basin IV by following a straight path. The western channel becomes deeply incised in the area between Basins II and IV, and it does not show connections with other channels (Badalini et al., 2000). The most distal basin (Basin IV) has a water depth ranging between 1,102 m and 1,479 m and it is underfilled (Satterfield and Behrens, 1990; Winker, 1996; Beaubouef et al., 1998; Badalini et al., 2000; Beaubouef and Friedmann, 2000; Beaubouef and Abreu, 2006; Mallarino G. et al., 2006). The dimensions of these basins range between kilometers to tens of kilometers. Only Basins II-III-IV are considered in this study.

Turbidity current and sedimentation in minibasins

A conceptual model has been developed to describe how turbidity currents fill minibasins and it is called 'fill-and-spill' model (Winker 1996, Prather et al. 1998, Toniolo et al. 2006). First, the turbidity current must reach the continental shelf and then the minibasin system. When the turbidity current enters an empty minibasin, it reflects on the distal flank creating an upstream migrating bore (Kneller et al., 1991; Edwards, 1993). A sharp interface separates the clear water above from the turbidity current when the duration of the flow is longer than the timescale for the migrating bore eventually stabilizes, and in the case that the downstream flank of the minibasin is high enough (same order of the flow depth) to create an obstacle for the current (Rottman et al., 1985; Woods et al., 1998). At this stage, a zone characterized by highly Froude-subcritical flow within the basin develops (ponded zone) and sediments are deposited at a lower elevation with respect to the lowermost point of the basin (spill point, ponded deposit). In phases in which sedimentation

exceeds subsidence, the thickness of the ponded deposit increases, the space between the minibasin floor and the spill point decreases, and the turbidity currents eventually overspill (Sinclair and Tomasso, 2002). At this stage the depositional pattern changes with preferential sediment deposition in the proximal part of the minibasin and the formation of what is called a perched apron (Prather et al., 1998; Booth et al., 2000; Prather, 2000; e.g., Booth et al., 2003; Prather, 2000; Pirmez et al., 2012; Prather et al., 2012; Bohn et al., 2012).

Field studies

One approach to study the minibasins filling process and understand the mechanism of transporting coarse clastic sediment to the basin far downdip of the shelf edge, is the analysis of the modern seafloor and the first few hundred meters below, using conventional exploration data, e.g., acoustic images of the bathymetry, cores, 2D and 3D seismic analysis, and well logs (Damuth et al. 1983; Malinverno et al. 1988; Bouma and Bryant 1994; Gardner et al. 1996; Winker 1996; Liu and Bryant 2000; Pirmez et al. 2000; Badalini et al. 2000, among many others).

Suter and Berryhill (1985) first described the presence of four minibasin in offshore Texas, and Winker (1996) described the system as a structurally ponded fan (Basin I-II-IV, and a graben-III) where each basin is filled with onlapping deposits, and that only Basin I-III are filled to their topographic spill point in a progressive basin-ward direction ('fill-and-spill' model). The basins are found filled during the same period (Badalini et al. 2000) with coarse fractions (sand) retained preferentially in the updip part while fine material (mud) overspills and fills the minibasin downstream. Sand fraction can bypass the updip areas and be transported with the mud accumulated laterally on the levees in the presence

of channels that connects subsequence minibasins (Winker, 1996; Badalini et al., 2000; Beaubouef and Friedmann, 2000) and supply sediments to the next minibasin downslope (Holman and Robertson 1994; McGee et al. 1994; Winker 1996).

Prather et al. (2000) used a stratigraphic model and calibrated the depositional process of the minibasin in the Gulf of Mexico, defining the accommodation spaces across the slope and its stratigraphic architecture. The sedimentary fill process of the basin generally develops in three subsequent stages that, in order, are a) a 'ponded' fill stage, b) a 'perched' fill stage, c) a complete bypass stage (Beaubouef and Friedmann, 2000). The terms of 'ponded aprons', for deposit created below the geometric spill point of the basin during the first phases of the filling process, and 'perched aprons' for those located above the spill point, characterized by the presence of bypass channels and knick-points have been introduced. The ponded aprons have been further distinguished by Prather et al. (2012) in 'low-relief' ponded apron for those with a maximum thickness at the center of the basin, and 'high-relief' ponded aprons for the deposits that are in the ponded accommodation space of the basins, but have maximum deposit thickness at the updip part of the basin.

Experimental modeling

More recently, experimental and numerical modeling has been conducted to understand the dynamics of turbidity currents in minibasins. The process of deposition in a minibasin is not directly observable in the field. It can, however, be modeled at laboratory scale.

Lamb et al. (2004) investigated the relationship between the dynamics of turbidity currents and the architecture of the deposit in a minibasin. In the case of sustained turbidity

currents, the ponded zone was located between either the headgate or a hydraulic jump, and the downstream lip. Lamb et al. (2006) investigated the trapping efficiency of a ponded zone and found that concentration and the geometric mean of the suspended sediment in the ponded zone vary only weakly in the ponded zone creating a weak pattern of downstream fining of the deposit. By upscaling their results, Lamb et al. (2006) concluded that many intraslope minibasins should trap most of the incoming sediment. Violet et al. (2005) did experimental work on a 3D model of subsiding minibasin. They made an interesting observation of the morphology of the deposit. The resulting deposit in their experiment was predominantly aggradational, but erosion occurred in the proximal and medial zone. They observed the formation of current ripples and post-depositional sediment deformation. Toniolo et al. (2006a) developed a theory to describe the sediment deposition in minibasin of ponded turbidity currents with uniform sediment size, that has been tested experimentally and numerically (Toniolo et al., 2006b). As the concentration in the ponded zone should be constant in the streamwise direction, the deposit should be spatially uniform in the streamwise direction.

Numerical modeling

Numerical modeling is used for a more in-depth understanding of the characteristics and features of the phenomenon, without facing some of the experimental limitations, e.g., cost, the time required to design and conduct the experiments and scale issues, allowing to explore a wide range of conditions (flow, geometry, sediment). Beaubouef et al. (2003a-b) simulated a turbidity current to highlight the significant differences in the depositional process during both, the ‘ponding’ and the ‘perched’ phase of the basin filling. They

observed that internal controls, i.e., bathymetry, affect the positions, extension, and pattern of the deposit.

A layer-integrated model has been developed by Toniolo et al. (2006b) to describe the sediment deposition inside the minibasins. The layer-integrated model does not provide information on the vertical structure of the flow field. To overcome the limitations of layer-integrated and depth-averaged models, Khan and Imran (2008) developed a two-dimensional numerical vertical-structure-resolving model of turbidity currents to illustrate the dynamics of the flow as well as morphological effects when a turbidity current enters two minibasins in series, both at experimental and field scale.

Long-term prediction of sediment transport and morphology is critical to understand the evolution of the morphology and the stratigraphy of submarine minibasins. The numerical simulation of three-dimensional field scale geometry, however, can be computationally expensive. One of the key issues in long-term modeling is to bridge the gap between the short-term hydrodynamics (timescale varies from hours to days) and the morphological changes, taking place over a very long period. For this reason, the model used in this study has been implemented with a Morphological Acceleration Factor that enables the morphology to evolve at a faster rate.

Objective

The primary focus of this research is to simulate turbidity currents at a laboratory scale for validation, and then apply the validated model to the cases of field-scale simulation of minibasins in the Gulf of Mexico to study the velocity and concentration field, and the morphology and grain size distribution of the sediment deposits. The results of this work will allow us to (a) understand how the shape and the grain size distribution

of the deposit changes according to the characteristics of the turbidity current entering the system and the morphology, geometry, and basin-floor topography of the area; (b) investigate the flow characteristics (velocity and concentration) and how the flow develops in both vertical and longitudinal directions inside minibasins, and (c) compute the grain size distribution of the deposit. Subsidence is not considered in this study.

CHAPTER 2

2D AND 3D NUMERICAL MODEL

Huang et al. (2005, 2007) developed a numerical model (TC-SOLVER) for turbidity currents with a deforming bottom boundary that can predict the vertical structure of the flow and sediment deposition and erosion under a wide variety of boundary conditions. The model, developed in-house at the University of South Carolina, is used to study the evolution of turbidity currents. The model uses a multiphase approach, and it solves the Reynolds-Averaged Navier-Stokes (RANS) equations for a suspension along with a mass conservation equation for solute as well as sediment mixture. A finite-volume scheme is used to discretize the governing equations on a structured non-orthogonal grid, which updates according with the deposit and entrainment rate of the sediment at every time step.

The Ashida and Michiue (1972) relation is used for bedload transport, and the Smith and McLean (1991, 1992) formulation is used for the suspended sediment. The grid can deform and adjust in response to sediment deposition and entrainment. An entrainment-deposition rate is used to address the moving bed boundary. The bed evolution is modeled by solving the Exner equation for individual grain size classes. The buoyancy-modified k-ε model is used for turbulence closure.

2.1. GOVERNING EQUATIONS

The Reynolds-averaged Navier-Stoke equations for mass and momentum conservation for a flow driven by a density difference due to sediment in suspension or a solute are:

$$\frac{\partial(\rho u_i)}{\partial x_i} = 0$$

$$\frac{\partial(\rho u_i)}{\partial t} + \frac{\partial(\rho u_i u_j)}{\partial x_j} = -\frac{\partial p}{\partial x_j} + \frac{\partial}{\partial x_j}\left(u\frac{\partial(u_i)}{\partial x_i} - \rho\overline{u'_\iota u'_J}\right) + (\rho_s - \rho)cg_i$$

where u_i, u_j = Reynolds-averaged velocities in the coordinate direction (x_i, x_j) respectively, p = Reynolds-averaged pressure, ρ_s = sediment density and ρ = the water density, c = Reynolds-averaged concentration of the solute or sediments, g_i = acceleration of gravity. The Reynolds stresses $(-\rho\overline{u'_\iota u'_J})$ can be modeled as:

$$\rho\overline{u'_i u'_j} = \mu_t\left(\frac{\partial(u_i)}{\partial x_j} + \frac{\partial(u_j)}{\partial x_i}\right) - \frac{3}{2}\rho k\delta_{ij}$$

where δ_{ij} = Knonecker delta, μ_t is the eddy viscosity obtained from:

$$\mu_t = C_\mu \rho\frac{k^2}{\varepsilon}$$

C_μ = constant of the $k-\varepsilon$ model, k = turbulent kinetic energy, and ε = turbulent energy dissipation rate. The transport equations for k and ε are:

$$\frac{\partial(\rho k)}{\partial t} + \frac{\partial(\rho u_j k)}{\partial x_j} = \frac{\partial}{\partial x_j}\left[\left(\mu + \frac{\mu_t}{\sigma_k}\right)\frac{\partial k}{\partial x_j}\right] + G_{ij} - \rho\varepsilon + G_b$$

$$\frac{\partial(\rho\varepsilon)}{\partial t} + \frac{\partial(\rho u_j \varepsilon)}{\partial x_j} = \frac{\partial}{\partial x_j}\left[\left(u + \frac{\mu_t}{\sigma_\varepsilon}\right)\frac{\partial\varepsilon}{\partial x_j}\right] + C_{\varepsilon 1}\frac{\varepsilon}{k}\left(G_{ij} + G_{\varepsilon 3}G_b\right)$$

where the generation term is express as:

$$G_{ij} = -\rho\overline{u_i' u_j'}\frac{\partial u_i}{\partial x_i} = \rho v_t\left(\frac{\partial u_i}{\partial x_j} + \frac{\partial u_i}{\partial x_i}\right)\frac{\partial u_i}{\partial x_j}$$

and the buoyancy term (rate of work done against buoyancy forces by turbulent motion) is:

$$G_b = -gi\frac{v_t}{\sigma}\frac{\partial \rho}{\partial x_i}$$

v_t = kinematic eddy viscosity, and the model uses the Rodi (1984) standards values of turbulence ($C_\mu = 0.09; C_{\varepsilon 1} = 1.44; C_{\varepsilon 2} = 1.92;\ \sigma_k = 1.00; \sigma_\varepsilon = 1.30; \sigma = 0.85$)

The coefficient associated with the buoyancy term is calculated according to Henkes et al. (1991) $C_{\varepsilon 3} = \tanh\left|\frac{u_2}{u_1}\right|$ where u_1, u_2 are the local horizontal and vertical component respectively. The eddy viscosity is calculated as follow where C_μ in an empirical constant having a value of 0.09:

$$\nu_t = C_\mu\frac{k^2}{\varepsilon}$$

The mass conservation equation for solute or suspended sediment load, as a function of the Reynolds averaged concentration c is:

$$\frac{\partial(\rho c)}{\partial t} + \frac{\partial(\rho u_j(u_j - v_s\delta_{j2})c)}{\partial x_j} = \frac{\partial}{\partial x_j}\left[\left(\rho D_m + \frac{\mu_t}{Sc_t}\right)\frac{\partial c}{\partial x_j}\right]$$

where δ_{j2} is the Knonecker (2 indicating the opposite direction of gravity); D_m is the diffusion coefficient and Sc_t the turbulent Schmidt number.

The Exner equation for bed sediment continuity is:

$$(1-\lambda)\frac{\partial y}{\partial t} = D - E$$

where y is the bed elevation, λ is the sediment porosity, assumed as constant and set equal to 0.5 during the simulation, D and E are the sediment deposition and entrainment rate. In

the case of mixtures, considering the contribution of a grain size i characterized by a fraction F_i on the bed level change y_i, the Exner equation would take the form of (Huang et al., 2001):

$$\rho_i(1-\lambda)\frac{\partial y_i}{\partial t} = -\nabla\cdot(\rho_i F_i \vec{q}_i) + \rho_i D_i - \rho_i F_i E_i$$

The variation of the bed elevation (term on the left-hand side) is equal to the sum of the net bedload flux, the deposition due to suspension and the entrainment of sediment from the bed. At each time step, once the flow and concentration fields are solved, the model computes the contribution to the change in bed elevation by each grain size class, and the sum for all size classes would give the total bed level change for that time step. The sediment deposition rate is a function of the fall velocity of the sediment particles, estimated by Dietrich's empirical equation (Dietrich, 1982) and the near bed concentration as:

$$D_i = v_{si} c_{bi}$$

The entrainment rate for sediment in suspension is computed using the Smith and McLean (1977) formulation in the case of uniform material:

$$E = 0.65\,\gamma_0 \frac{\left(\frac{\tau_{bs}}{\tau_{bc}} - 1\right)}{\left[1 + \gamma_0\left(\frac{\tau_{bs}}{\tau_{bc}} - 1\right)\right]} \quad , \quad \gamma_0 = 0.0024$$

with τ_{bs} the bed shear stress due to skin friction and τ_{bc} the critical bed shear stress. In the case of mixtures (McLean 1991, 1992), the dimensionless rate of entrainment of bed sediment from the *i-th* grain size range into suspension is:

$$E_i = p_{sbi} E_T$$

where p_{sbi} is the fractions in the *i-th* grain size range in the sediment entrained from the bed, described as:

$$p_{sbi} = \frac{\varphi_i \, p_i}{\sum_{i=1}^{N} \varphi_i \, p_i} \qquad \varphi_i = \begin{cases} 1, & for \dfrac{u_{*s}}{v_{si}} > 1 \\ \dfrac{u_{*s} - u_{*c}}{v_{si} - u_{*c}}, & for \dfrac{u_{*s}}{v_{si}} < 1 \end{cases}$$

where $u_{*s} = \sqrt{\tau_{bs}/\rho}$ is the shear velocities due to skin friction and $u_{*c} = \sqrt{\tau_{bc}/\rho}$ is the critical shear velocity, evaluated using the D_{50} of the bed material. The total entrainment rate E_T is:

$$E_T = (1-\lambda)\gamma_0 \frac{\left(\frac{\tau_{bs}}{\tau_{bc}} - 1\right)}{\left[1 + \gamma_0 \left(\frac{\tau_{bs}}{\tau_{bc}} - 1\right)\right]} \quad , \quad \gamma_0 = 0.004$$

The bedload transport is quantified using the Ashida and Michiue (1972) formulation as a function of the dimensionless Einstein bedload number $q_b^* = q_b/\left(\sqrt{RgD}D\right)$:

$$q_b^* = 17(\tau^* - \tau_c^*)(\sqrt{\tau^*} - \sqrt{\tau_c^*}) \quad , \quad \tau_c^* = 0.05$$

where τ^* is the Shields number, while the direction on the sloping bed is calculated considering the composite effect of bed shear, bed slope and shape factors of the particles (Huang et al., 2012).

The model uses a simplified version of the active layer scheme proposed by Karim and Kennedy (Huang et al., 2007) to track the change of the sediment fraction in the *i-th* grain size, and the new fraction of particle size i at timestep *t* can be expressed as:

$$F_i^t = \frac{H^t p_i^{t-1} + \delta_i^t - \delta^t p_i^{t-1}}{\sum_i H^t p_i^{t-1} + \delta_i^t - \delta^t p_i^{t-1}}$$

H represents the thickness of the mixing layer, δ_i^t and $\delta^t$are the thickness of the deposit (negative for erosion) during the time interval respectively for the *i-th* grain size and for the total grains.

2.2. BOUNDARY CONDITIONS

A number of boundary conditions is implemented in the numerical model, e.g., inlet, outlet, symmetry, and solid wall. The inlet conditions are defined in the upstream side of the domain, by defining the inlet velocity of the turbidity current, the sediment and solute concentrations and current thickness, the inlet turbulent kinetic energy and dissipation rate are estimated as $k_{in} = (0.1\ u_{in})^2$ and $\varepsilon_{in} = 4\ {k_{in}}^{\frac{3}{2}}/h_{in}$ where u_{in}, k_{in}, are the averaged velocity, turbulent kinetic energy and thickness of the current at the inlet. The variables are assumed completely developed in space at the outlet and their gradient is set equal to zero in the direction perpendicular of the outlet boundary.

The free surface is typically well above the density current so that it does not interfere with it, and it is therefore, described by a symmetry boundary condition, which means zero fluxes across the boundary. The velocity profile at the wall is estimated accordingly with the logarithmic law. The bottom of the grid system is updated during each time step according to the change in bed level due to bedload, sediment entrainment and deposition calculated from the solution of the Exner equation.

2.3. SOLUTION PROCEDURE

The governing equations are discretized using an implicit finite-volume scheme for a non-orthogonal grid system (Ferziger and Peric, 2002). The non-orthogonality is addressed directly in the process of approximating the convective and diffusive flux through the cell instead of transforming the grid to orthogonal curvilinear coordinates, with the advantage of the model equations in the original forms.

The model uses the collocated arrangements in which the same control volume is used for all the variables. For the unsteady term, discretization is used as an implicit three-

time level scheme of second-order accuracy for any dependent variable ϕ in the control volume $\Delta\Omega$

$$\left[\frac{\Delta(\rho\phi)}{\Delta t}\Delta\Omega\right]_P = \left[\frac{\rho\Delta\Omega}{2\,\Delta t}(3\phi_i^{n+1} - 4\phi_i^n + \phi_i^{n-1}\right]_P$$

with P the center of the nodes in the control volume at which the governing equation is approximated, and n is the time level. The values at the cell face is obtained through linear interpolation.

The discretization of the convective and diffusive terms is approximated using a deferred-correction approach, by blending the first-order upwind scheme (UDS) with the second-order central difference scheme (CDS) (Ferziger and Peric, 2002)

$$F^{UDS} + \alpha(F^{CDS} - F^{UDS})$$

where the convective flux approximated respectively with the upwind and central difference scheme are F^{UDS} and F^{CDS} and the blending factor is assumed as $\alpha = 0.1$ so that the scheme is overall close to the second order accuracy. Approximation of the convective flux through a cell face (face "e" with P and E the cell centers neighboring the face is calculated) of a scalar variable, ϕ, is:

$$\min(m_e, 0)\,\phi_E + \max(m_e, 0)\,\phi_P + \{m_e[\lambda_e\phi_E + (1-\lambda_e)\phi_P] - \min(m_e, 0)\,\phi_E + \max(m_e, 0)\,\phi_P\}^{n-1}$$

where m_e is the max flux through face "e" and λ_e is a linear interpolation coefficient calculated from grid geometry, and n is the iteration number. Approximation of the diffusive flux is calculated as

$$D_e\left[\frac{\phi_E^n - \phi_P^n}{|r_{PE}|}S_e + (\nabla\phi)_e^{n-1}(\boldsymbol{n} - \boldsymbol{i}_\xi)S_e\right]$$

where D_e is the dispersion coefficient, S_e is the absolute value of the area normal to the face cell; $|r_{PE}|$ is the distance between the two neighboring cell's center values. The non-orthogonal part of the diffusion transport is corrected by explicitly using the values from the preceding iteration. $\boldsymbol{i}_{\xi}$ is the unit direction vector from cell center P to E and $\boldsymbol{n}$ is the cell face unit normal vector, $(\nabla\phi)_e^{n-1}$ is obtained explicitly with Gauss theorem from values of the preceding iteration step.

This study adopts the pressure implicit with the splitting of operators' algorithm for solving the RANS equations: first, the velocity components and pressure are solved, then, the scalar transport equations for turbulent kinetic energy, dissipation rate, and sediment concentration are solved. The bed gets adjusted accordingly with bed elevation changes due to sediment entrainment and deposition by uniformly distributing the bed level change Δy_{bed} to all the grid points above it except the one that represent the free surface (most top grid point), ensuring the original smoothness of the entire grid system.

2.4. ACTIVE-LAYER FORMULATION

Rivers can carry sediment for long distances, create areas of erosion and deposition, and change the sediment distribution on the bed surface and the floodplain. Similar processes can also occur in the submarine environment due to turbidity currents.

As the bed aggrades, the current deposits sediment creating a new substrate; when it degrades, the flow erodes and selectively entrains and transports the various grainsizes downstream. The process changes the grain size distribution in the vertical as well as the horizontal direction of the bed, creating a "stratigraphy." The active-layer concept of Karim and Kennedy (1982) has been implemented in the numerical model, assuming that the upper layer of the bed (few grain sizes thick or of the order of the average height of the

bedforms) is actively involved in the sediment transport process and that the change in bed material composition on the bed surface is calculated assuming that different sediment size fractions are homogeneously distributed in the mixed layer.

2.5. STRATIGRAPHIC MODEL

During morphological changes of a channel bed in response to a flow, the amount leaving the mixing layer depends on degradation while the amount becoming part of the mixing layer depends on aggradation; if the bed elevation and the mixing layer thickness do not change in time, then the amount of material entering (or leaving) the mixed layer from below (or above) equals the amount of degradation (or aggradation). When the bed degrades, sediment enters the mixed layer from below; when the bed aggrades, part of the material located in the mixed layer becomes part of the inactive bed below.

A wide variety of experiments have been conducted and numerical models have been developed to study the structure of the deposit due to aggradation and degradation, but few of them are designed for storing the spatial variation of the deposit due to aggradation, and then re-access this information computationally when the bed degrades. Viparelli et al. (2010) developed one of the few morphological models that can store and access stratigraphy. We implemented the approach of Viparelli et al. (2010) here for turbidity currents.

A new subroutine is added to the 3D model of turbidity currents described earlier to allow the model to preserve stratigraphy in a text file as it is created by aggradation, and access the information if and when the flow degrades into the deposit.

The computational domain for the bed is discretized into N number of j-nodes (same number of nodes of the computational domain) in the streamwise direction, and M points (k) in the vertical direction:

$$M_j\big|_{t=0} = int\left(\frac{\eta_j\big|_{t=0} - L_{m,j}\big|_{t=0}}{L_s}\right) + 2$$

where *int* is a function that gives output as an integer value. All storage layers have thickness Ls, and the mixing layer has thickness Lm. Small values for storage layer thickness (Ls) allow to record a finer stratigraphic structure. The initial grid for the stratigraphy domain is defined accordingly with the initial longitudinal bed profile, the thickness of the storage layers and the number of vertical nodes. The storage grid is updated at every time-step by adding or removing computational nodes, accordingly with the process of aggradation or degradation of the bed (Figure 2.2).

When the bed aggrades at a generic node, *j*, a new layer of thickness, $\Delta\eta_j = \Delta\eta_j\big|_{t+\Delta t} - \Delta\eta_j\big|_t$, computed solving the Exner equation, is deposited on top of the initial bed, and accordingly with the Karim and Kennedy active layer formulation, the bottom part of the deposit becomes part of the substrate. When the amount of aggradation within one time step is not enough to fill the storage layer, a new storage point is created as:

$$\eta_j\big|_{t+\Delta t} \leq \left(M_j\big|_{t+\Delta t} - 1\right) L_s = \left(M_j\big|_t - 1\right) L_s.$$

The new sediment deposited is mixed into the antecedent sediment layer in volumetric proportion, so that the sediment fraction in the layer does not have a vertical structure, but it is uniformly mixed within the *k*-layer, at the generic node *j*.

When the amount deposited on top of the uppermost storage layer reaches the thickness, Ls, one or more new storage layers are created accordingly with the thickness of the deposit. The grainsize distribution of the antecedent storage layer is computed as the volume average of the sediment previously located there and the new sediment deposited,

while the sediment composition of the new layer on top is characterized by the grain size distribution deposited by the flow.

In the case of degradation, the flow erodes material from the bed. According to the amount of bed eroded, $\eta_j\big|_{t+\Delta t}$, the storage layer $L_{s,k}$ that has been reached and from where the sediment is taken is determined. Knowing that, the information of the grain size characteristics that have been stored for that specific layer are accessed and used to describe the now new topmost storage layer.

2.6. THE MORPHOLOGICAL ACCELERATION FACTOR (MORFAC)

Morphodynamic models are tools that allow for the study and prediction of the evolution of coastal, river and estuarine systems, analysis of sediment transport and erosional problems, and aid in the design of coastal defenses. In these scenarios, while the hydrodynamic evolution varies from hours to days, the morphological changes may take place over a much longer timescale.

Lesser et al. (2004) and Roelvink (2006) introduced the Morphological Acceleration Factor (MORFAC), a technique to perform morphological simulations by using hydrodynamic simulations of only a fraction of the required duration. The MORFAC approach decouples the time-scale of the morphological model from the time-scale of the hydrodynamic and sediment transport models, and so it can be viewed as a form of model reduction:

$$\Delta T_{morphology} = MORFAC \cdot \Delta T_{hydrodinamic}$$

One must realize that the most critical time-scale of the model is now the morphodynamic timescale and that the hydrodynamic and sediment transport models are only run to provide updates (in terms of residual sediment transport vectors) to the

morphological model (Lesser, 2009). When fluctuating boundary conditions are applied to the hydrodynamic model, it is essential to conceptually separate the hydrodynamic and morphological models and their associated timescales. In the case of fluctuations of boundary conditions (e.g., tidal) are applied at hydrodynamic time scales, the impact of these fluctuations is applied by MORFAC before being applied to the morphological model.

According to the Morphological Acceleration Factor technique, at each hydrodynamic time step the fluxes of suspended sediment and the bedload sediment transport components to and from the bed are multiplied by MORFAC: if MORFAC is greater than 1.0, then the morphological time step is effectively made longer than the hydrodynamic time step, and the bed change is upscaled accordingly. The updated new bathymetry is then used in the next hydrodynamic step (Figure 2.3).

There are limits on the applicability of this method, depending on the characteristics of the location under consideration, and the selection of a suitable Morphological Acceleration Factor remains a matter of judgment.

The appropriate morphological acceleration factors must be chosen and tested on a case-by-case basis. One of the limits of this method is that it upscales the bed dynamics by a constant factor, but, the bed can experience vertical growth and horizontal propagation.

2.7. 2D MODEL VALIDATION DEPOSITIONAL TURBIDITY CURRENTS

The model is validated by simulating three experiments (DAPER6, GLASSA2, MIX5) of Garcia (1993) for depositional turbidity currents in an idealized model submarine canyon-fan system. The objective of the experiments was to study the hydrodynamic, depositional, and erosional characteristics of turbidity currents in a flume characterized by a slope change.

Garcia (1993) conducted the experiments in a 30 cm wide, 78 cm deep and 11.6 m long flume. The upstream section of the flume (5 m from the entrance) with a 0.08 slope represented a canyon, the following horizontal bed was used to represent the fan. The flow in all the experiments entered the flume as supercritical turbidity current, created an internal hydraulic jump at the slope break and transitioned to subcritical conditions.

Initial conditions

The inlet current thickness for all the experiments was set at 3 cm, while other parameters changed as reported in Table 2.1. The inlet Richardson numbers for all the simulations are below one at the entrance to ensure the generation of supercritical conditions. The sediment grain size distribution and initial concentration for the poorly sorted experiment (MIX5) is reported in Table 2.2. The model grid for the numerical simulations have a resolution of 109 x 81 nodes with 5 mm near bed grid size, which is found to give converged simulation results.

Results

Flow field: The sediment concentration profiles for the poorly sorted case (DAPER6) have been normalized with the corresponding layer-averaged values of concentration and current thickness. The comparison of the normalized velocity and sediment concentration profiles between the simulation DAPER6 and the measurements from Garcia (1993) experiments are shown in Figure 2.4. Overall match of the profiles is good. For the profile under the supercritical condition in the sloping part of the flume, the measured values show a good similarity collapse, unlike in the downstream subcritical zone. The numerical profiles follow the experimental profiles, especially under the supercritical condition.

Figure 2.6 displays the initial stages of the flow evolution in time of the turbidity current for the experiment MIX5. The turbidity current interface is represented by the 1,000 kg/m^3 contour line. The turbidity current enters the domain (t = 40 s) in supercritical conditions. At 100 s the front reaches the horizontal part of the flume, and the current thickness increases in this downstream zone (t = 160 s). Once the current front leaves the downstream end of the domain (t = 220 s), the changes of the current thickness in time are slow (t = 300 s).

Deposit thickness: The deposit thickness at the end of each simulation with poorly sorted sediments is reported in Figure 2.5. The simulated profiles of the deposit thickness do not show any discontinuity at the slope break, in agreement with the experimental profiles. The turbidity current driven by finer diameter particles (DAPER6) shows a deposit that is almost uniform in thickness along the flume, and a weak depositional tendency. For this case, the turbidity current depositional capacity is not affected by the slope break or the hydraulic jump at the transition between supercritical and subcritical conditions. There is a good agreement between the simulated and the measured values for the deposit thickness.

The turbidity current with coarser grain (GLASSA2) show an exponential decrease in the deposit thickness. In this case, the simulated profile shows a good agreement in the downstream part of the flume, after the slope break (Figure 2.5).

The simulated depositional profile for MIX5 is compared with the experimental data in Figure 2.7. Similar to the case of well-sorted sediment, there is no discontinuity in the deposit profile at the slope break. The deposit thickness decreases exponentially in the streamwise direction for both numerical and experimental simulations.

2.8. 2D MODEL VALIDATION ON MINIBASIN AT LABORATORY SCALE

The experiments performed by Toniolo et al. (2006a) are characterized by water detrainment in the ponded area of the minibasins - area between the internal hydraulic jump and an elevation barrier located at the downstream end of the setup. Turbulence in the ponded zone was dying or dead, and the turbidity current formed a settling interface. Upstream of the hydraulic jump the turbidity current was fully turbulent, and because it was Froude-supercritical it could entrain water from above; downstream, the flow was slow and thick with a densimetric Froude number well below unity (subcritical).

In the experiments performed by Toniolo et al. (2006a), all the current was captured in the ponded zone, and so there was no overflow over the downstream lip of the domain even in the case of continuous flow.

Initial conditions

The flume used in these experiments was 0.304 m wide, 0.76 m deep and 12.80 m long, and it was filled with sediment-free water up to 0.60 m deep. Upstream of the flume, water and sediment were mixed in a tank, a dumping tank was located at the downstream end to collect the turbid water and prevent reflection of the turbidity current. The basin was 4.06 m long, and it was built inside the flume (Figure 2.8), with constant entrance slope (S_{b1}= 0.298) and a nearly horizontal central region (S_{b2} = 0.017); the maximum relief downstream is Δh_b = 0.46 m.

Two different experiments that differ in duration and sediment characteristics were conducted by Toniolo et al. (2006a); only Experiment 1 is simulated to validate the numerical model. The median size D_{50} used in the experiment was 45 μm, the geometric mean size D_g was 42 μm and the standard deviation σ_g was 1.25 (Figure 2.9). The

computational domain of the basin consists of 81 x 66 nodes, near bed cell size is 4 mm. The experimental conditions are reported in Table 2.3.

Results

The final bed, at time 58 minutes is compared with results from the numerical simulation (Figure 2.10). The simulation underestimates the bed deposit at the entrance, and over estimates it in the ponded area, but the error is within the 10%.

Toniolo et al. (2006a) collected the vertical profiles of the volume sediment concentration in suspension at time 16 minutes, 38 minutes, and at the end of the experiment (58 minutes) at different locations along the basin, using siphon rakes. The comparison between laboratory and numerical simulation results is presented in Figure 2.11. The samples from the siphons farther upstream show profile of the suspended sediment concentration that decay roughly exponentially in the vertical direction, a typical pattern observed in gradually-varied turbidity currents (Toniolo et al. 2006a). The two profiles located in the ponded zone are vertical, which means that the sediment concentration is uniform in the vertical direction and, furthermore, the two locations exhibit almost the same value for the concentration. The results from the simulations show a good agreement with the experiments.

Table 2.1: Initial conditions of the 2D experimental runs used to validate the model (Garcia 1993)

Parameters	DAPER6	GLASSA2	MIX5
Inflow velocity, u_0 [m/s]	0.083	0.083	0.11
Inflow current thickness, h_0 [cm]	3	3	3
Inflow sediment concentration, c_0 10^{-3} [m^3/m^3]	3.72	3.39	7.28
Particle geometric mean size diameter, D_g [μm]	9	30	26
Total simulation time, [min]	40	30	30

Table 2.2: Sediment grain size distribution for poorly sorted turbidity current experiment (MIX5)

k	Diameter, D_k [μm]	Fraction, F_k [%]	Concentration, C_k [m^3/m^3]
1	5.00	5.12	3.73E-04
2	8.00	7.59	5.53E-04
3	12.70	15.14	1.10E-03
4	20.20	23.27	1.69E-03
5	32.00	34.38	2.50E-03
6	50.80	14.28	1.04E-03
7	80.60	0.22	1.60E-05

Table 2.3: Initial parameters for the 2D basin model validation at laboratory scale (Toniolo et al. 2006a)

Parameter	Value
Discharge Q_u [l/s]	0.33
Flow thickness h_u [cm]	1.00
Concentration C_u	0.05
Sediment fall velocity [cm/s]	0.14
Duration [min]	58
D_{50} [μm]	45

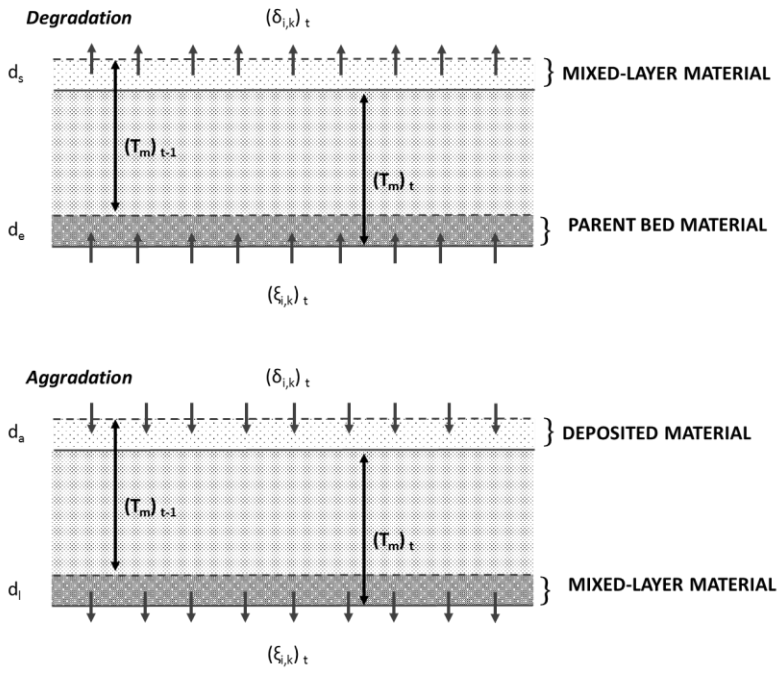

Figure 2.1: Active –layer formulation from Karim and Kennedy (1982) where:

$(T_m)_{t-1}$: mixed layer thickness at interval (t-1)

$(\delta_{i,k})_t$: depth of aggradation / degradation for sediment interval k in reach i during time interval t

$(\xi_{i,k})_t$: amount of material in size interval k which enters the mixed layer in reach i during the time interval t for degradation, and leaves it for aggradation

d_s: depth of degradation, during interval t

$d_e = (T_m)_t + d_s - (T_m)_{t-1}$: depth of parent bed material entering the mixed layer, during interval t

d_a: depth of deposition, during interval t

$d_l = (T_m)_{t-1} + d_a - (T_m)_t$: depth of material leaving the mixed layer, during interval t

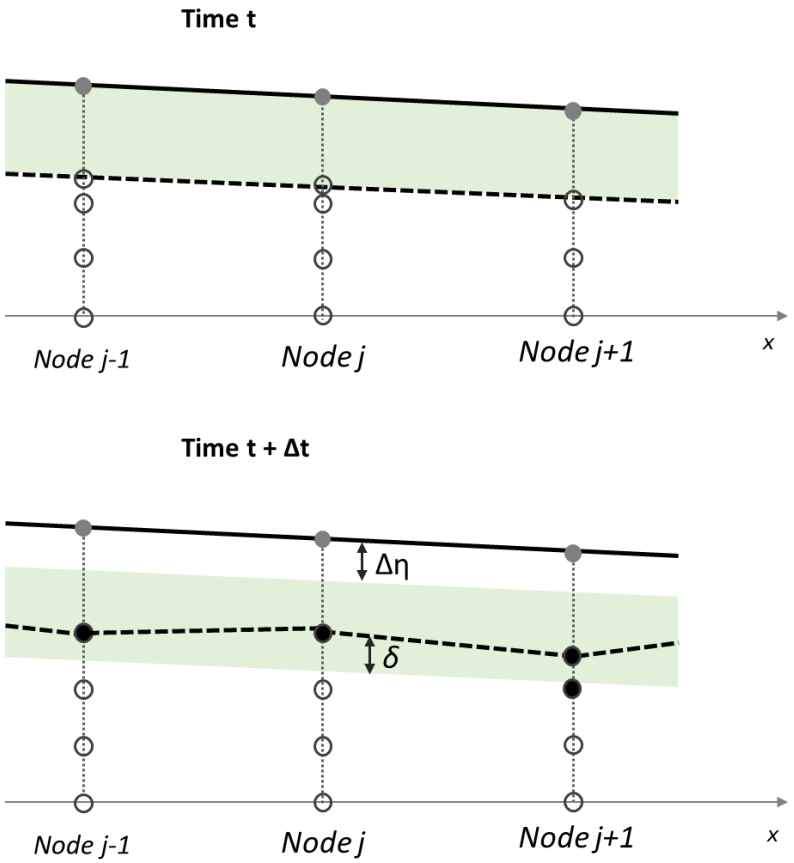

Figure 2.2: Grid extension as the bed aggrades to store stratigraphy information from the time (t) to (t+Δt) (Viparelli et al., 2010). At nodes (j-1) and (j) the grid points moved upward of the same amount of the deposit thickness at that node. At node (j+1) a new grid point is added in the vertical direction as the distance from the updated grid point (at t+ Δt) and its location at the previous time step (t) exceed the grid size

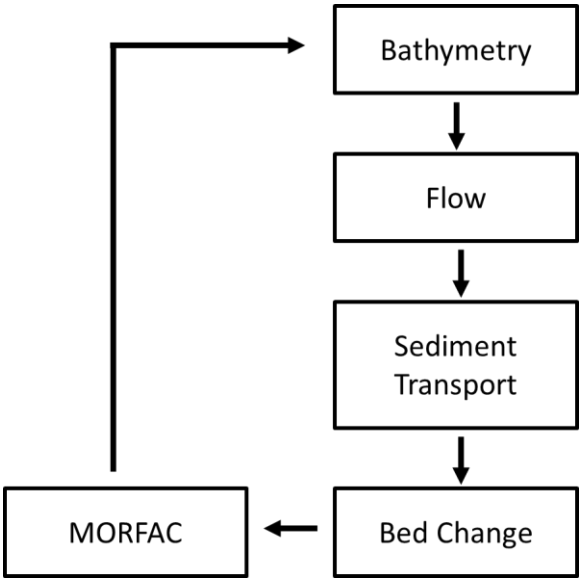

Figure 2.3: General structure of the coastal morphodynamic models that apply the Morphological Acceleration Factor concept (MORFAC)

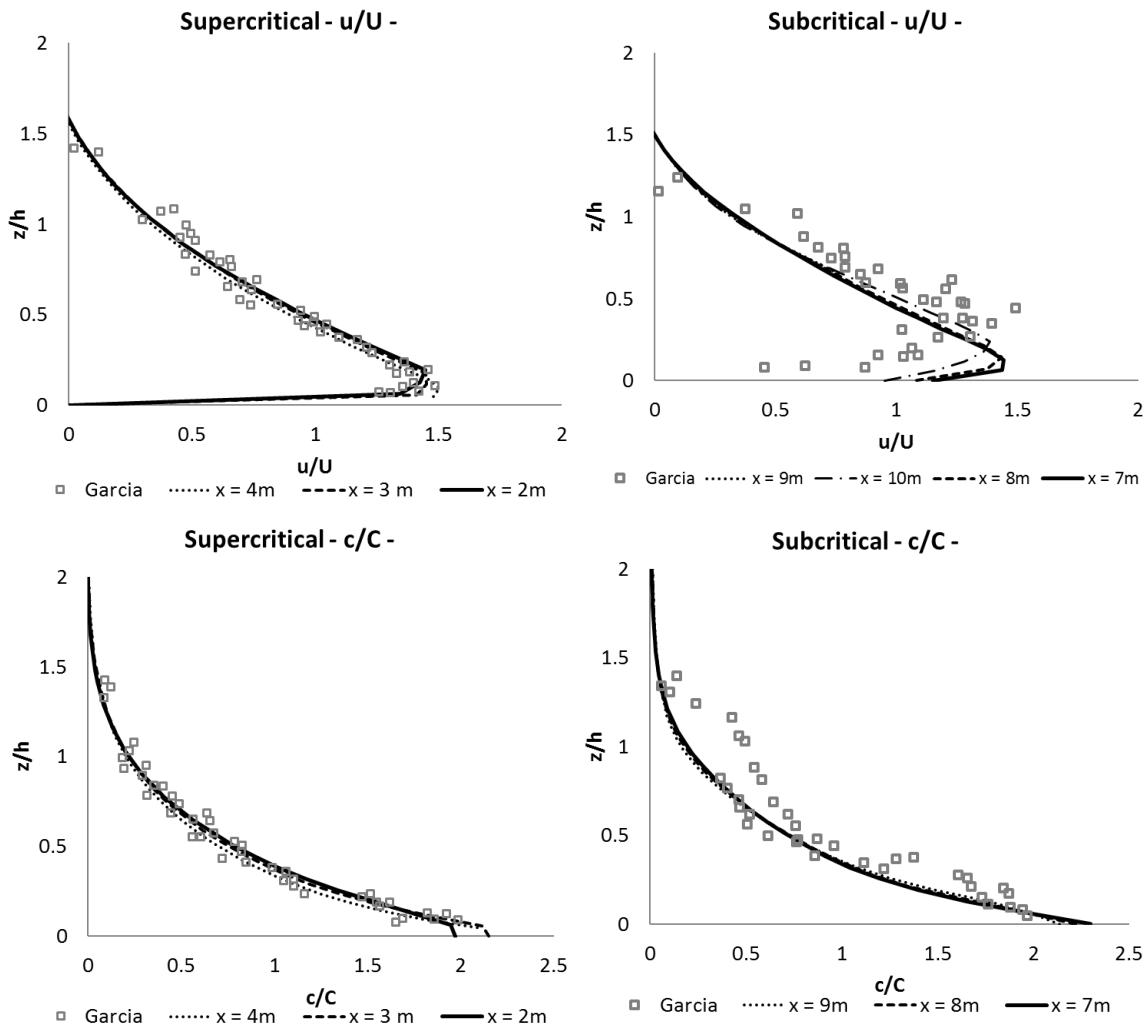

Figure 2.4: Normalized velocity and concentration comparison in the supercritical and subcritical zone for the set of experiment with poorly-sorted sediment (DAPER6). Markers represent the measured values (experimental simulations) and the lines represent the numerical simulated profiles at different locations in the supercritical (x = 2, 3, 4 m) and subcritical zone (x = 7, 8, 9 m)

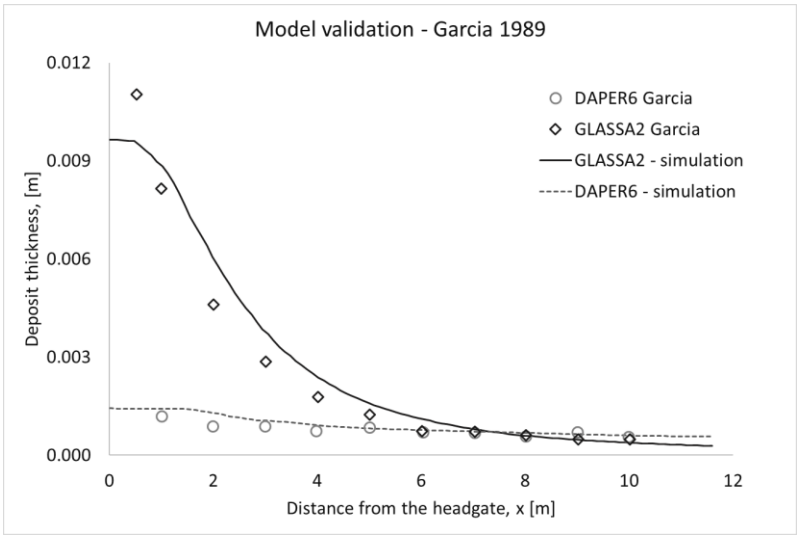

Figure 2.5: Comparison of the simulated and measured deposit thickness versus distance for the poorly sorted experiments (Garcia 1993 – GLASSA2 and DAPER6). Markers represents the experimentally measured values of the deposit thickness, while the lines represent the numerically simulated profiles

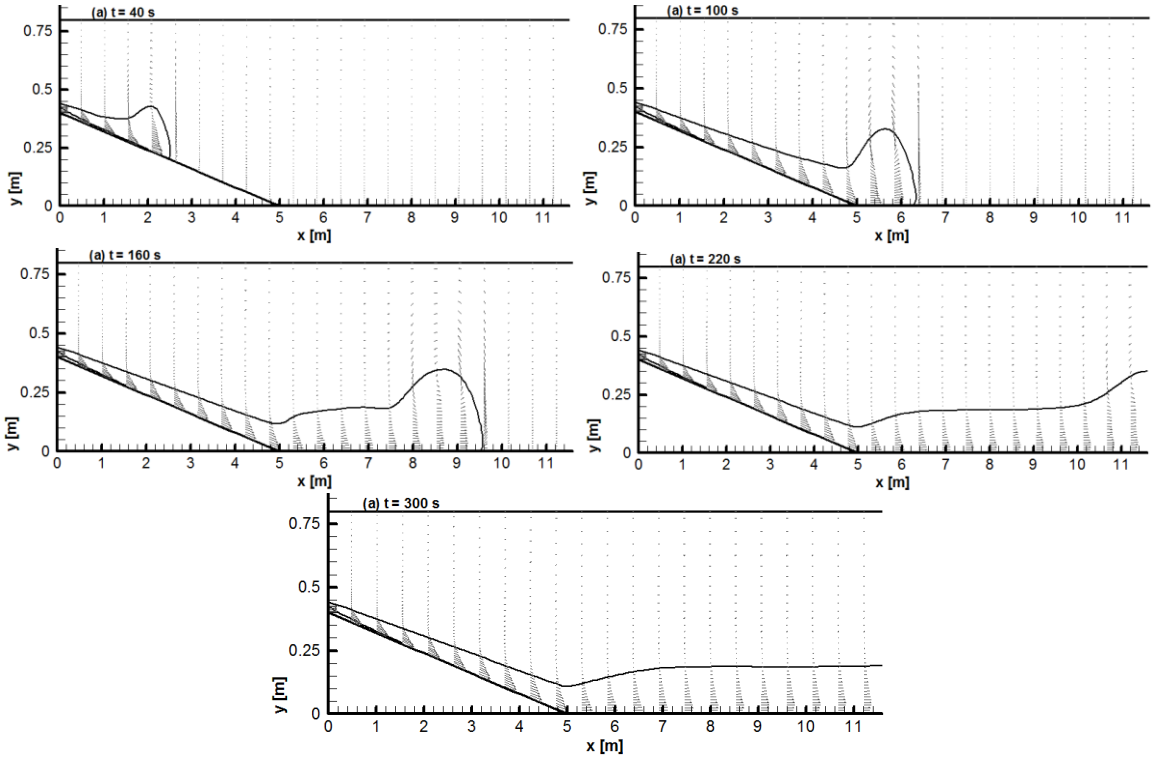

Figure 2.6: Simulated propagation of a turbidity current in time for the experimental run MIX5 (Garcia 1993) at different time (40, 100, 160, 220, 300 s from the beginning of the simulation)

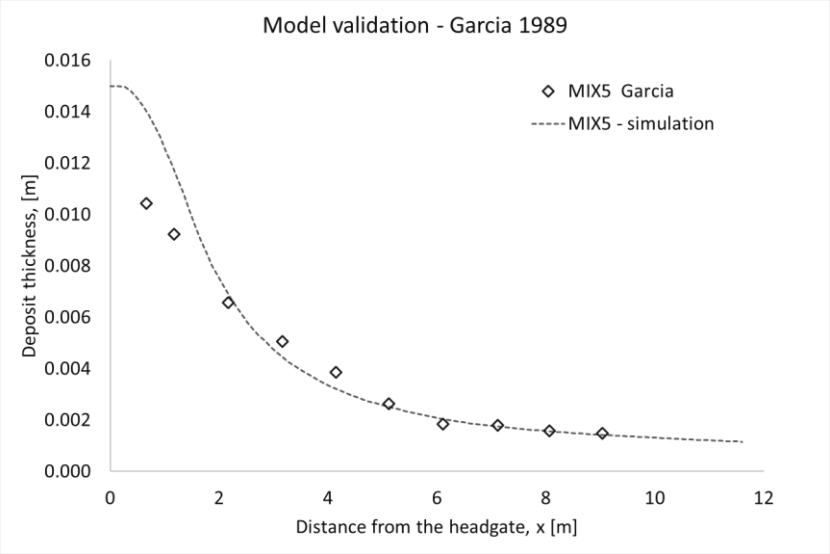

Figure 2.7: Comparison of the simulated (dashed line) and measured (markers) deposit thickness versus distance for the well sorted experiments (MIX5 – Garcia 1993)

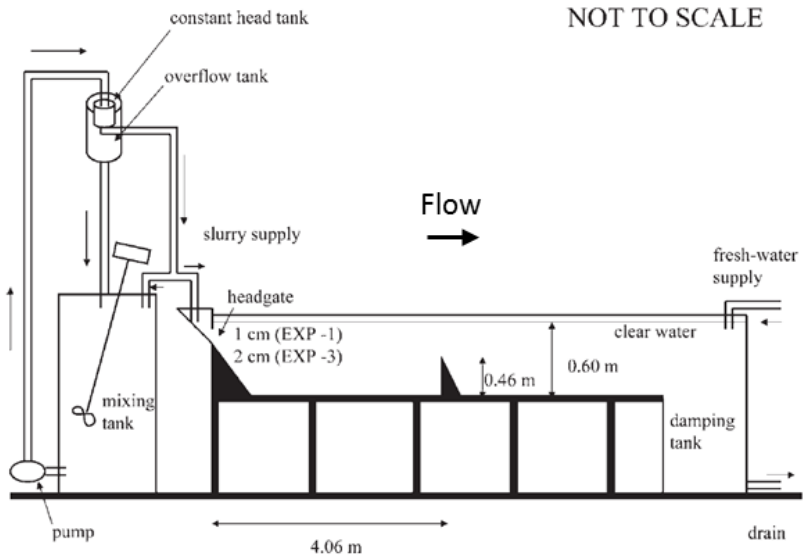

Figure 2.8: Experimental setup used by Toniolo et al. (2006a) to simulate two-dimensional basin flow and deposits. The data collected during these experiments have been used for the model validation (modified from Toniolo et al., 2006a)

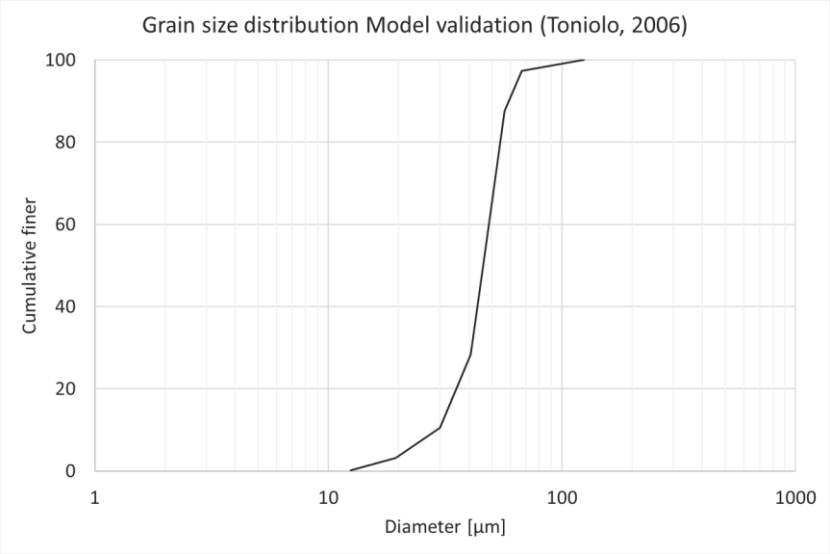

Figure 2.9: Grain size distribution of the turbidity current used for the 2D model validation simulation (Toniolo, 2006a)

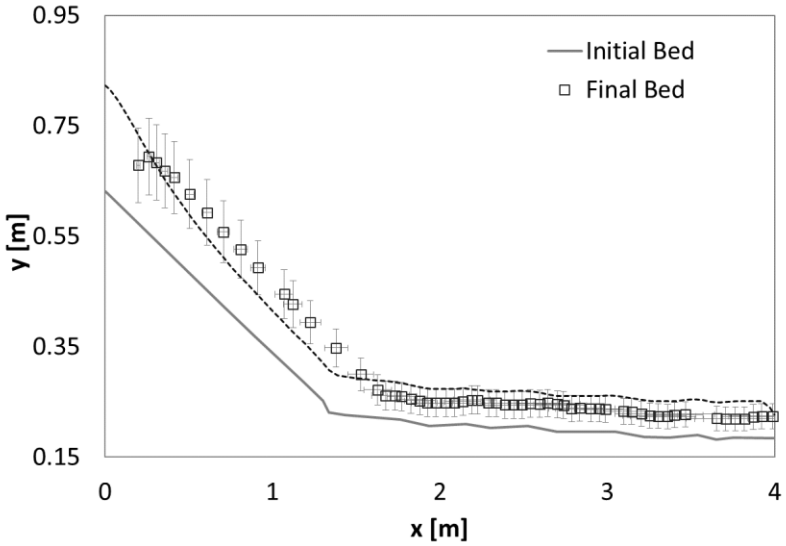

Figure 2.10: Comparison of the experimental measured (markers, Toniolo et al., 2006a) and the numerical simulated bed elevation profile versus distance, at 58 minutes

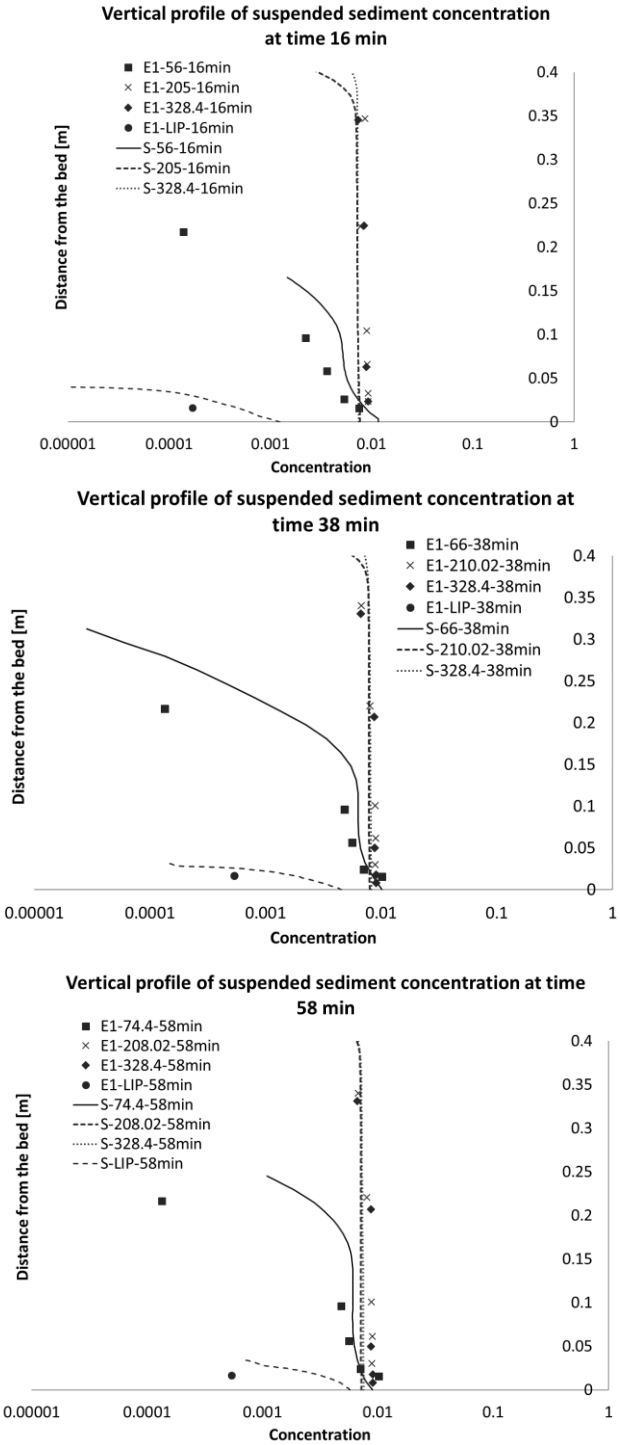

Figure 2.11: Vertical profiles of the suspended sediment concentration at various time (16-38-58 minutes) from the beginning of the 2D laboratory scale simulation of minibasin flow. In each case the vertical concentration profile is plotted at three stream wise locations and at the lip, accordingly with the laboratory measurements made by Toniolo et al. (2006a)

CHAPTER 3

MODELING MORPHODYNAMIC ACCELERATION AND SEDIMENTARY STRATA FOR TURBIDITE

3.1. INTRODUCTION

Predicting the long-term morphology with a physical based model is still uncertain and time consuming. Running real-time model which reproduce time processes that require a long term of simulated hydrodynamic modeling, leads to computations very time consuming. In the last decades, several techniques have been implemented to overcome this limitation, and to accelerate the computation. The idea behind these ideas is the same: bridge the gap between morphological and hydrodynamic timescale. The timescale of the morphological changes can be very long compared with the evolution of the flow characteristics and its adaptations to changes.

The aim of this work is to i) systematically study the effect of the Morphological Acceleration Factor (MORFAC) on the flow and bed evolution, at field and laboratory scale, ii) study the evolution of sediment grain size distribution of the deposited sediment strata. Most, if not all the morphodynamic phenomenon experience a transition time before reaching equilibrium conditions. When a morphological acceleration approach is used this transitional time can become key on the final morphological development.

Furthermore, the model used in this study has been implemented with a subroutine that stores the stratigraphy of the deposit. In this study, two-dimensional cases at field scale and a three-dimensional case at laboratory scale have been investigated to analyze the effect of the morphological acceleration on the deposit architecture.

3.2. 2D AND 3D MODEL APPLICATION AT LABORATORY AND FIELD SCALE

The model has been found to be able to simulate the flow structure and deposit thickness of two-dimensional laboratory experiments on turbidity currents with multiple grain size fractions.

In this section, the model is applied to laboratory and field scale turbidity currents over two and three-dimensional geometries to investigate the effects of MORFAC on the amplification of the bed amplitude. To that end, MORFAC equal to 2 and 5 is applied for the different cases considered. Furthermore, a higher value of MORFAC (10) is applied for the 2D field scale and the 3D laboratory scale simulations.

By continuously exchanging sediment with the bed and entraining clear water from above, turbidity currents never really reach a true equilibrium state. However, turbidity currents with steady inflow can eventually reach a quasi-steady state at a location, when the front has passed that specific location (Huang et al., 2005). For this reason, the effect of the morphological acceleration factor on the bed elevation is compared between the cases in which the parameter has been applied from the beginning of the simulation (MORFAC2-I, MORFAC5-I, MORFAC10-I) with the cases in which it has been applied when the current reaches quasi-equilibrium conditions (MORFAC2-II, MORFAC5-II, MORFAC10-II). The benchmark case is called MORFAC1, which means that the morphological acceleration factor is not applied

In all the simulations, a porosity equal to 0.4 and the submerged specific gravity of the sediment (R) equal to 1.65 are considered.

Two-dimensional laboratory-scale application

The first two test cases that have been simulated are from the laboratory experiments performed by Garcia (1993) using well (GLASSA2) and poorly (MIX5) sorted sediments (these cases are the same ones used for the validation of the numerical model, Figure 2.5 and Figure 2.7). Morphological acceleration factors equal to 2 and 5 are used for these tests, in the case that they are applied from the beginning of the hydrodynamic simulation (MORFAC2-I and MORFAC5-II) or when the front reaches the end of the domain (MORFAC2-II and MORFAC5-II).

The initial conditions are reported in Table 2.1 (Chapter 2). The initial geometry is the same for both cases. The turbidity current front reaches the end of the domain at 300 s for the well-sorted sediment case (GLASSA2), while for the other test (MIX5) it reaches the end at 200 s.

The comparison of the bed deposit thickness at the end of the simulations is reported in Figure 3.1 and Figure 3.2. From the measured laboratory profiles, GLASSA2 deposits more sediment than MIX5. The application of the morphological acceleration factor after the front reaches the end of the domain (MORFAC2-II and MORFAC5-II) results in an overestimate of the bed deposit thickness, which is greater for the case of thicker deposit of the benchmark case. The cases of MORFAC applied from the beginning of the simulation show a good agreement with the benchmark case for both the tests.

Two-dimensional field-scale application – slope change

A 2D field scale simulation on slope change has been performed. The channel is 1,000 m long and it is characterized by a slope change at 500 m where the slope decreases from 4% to 1% (Figure 3.3). The near bed grid size is 5 cm and the spatial resolution of the computational grid is 3 m. The total simulated time is 15 hours and the time step used is 0.5 seconds. The turbidity current enters the domain with uniform velocity of 0.8 m/s and it reaches quasi-steady conditions after 40 minutes of flow. The grain size distribution of the turbidity current reported in Figure 3.4 is characterized by a mean grain size diameter of 60 μm and median diameter of 62.7 μm.

The current is initially simulated without applying the Morphological Acceleration Factor (MORFAC1). The result of this benchmark case is then compared with the combinations of different conditions that consist of different values of MORFAC (2 – 5 – 10), applied either at the beginning of the simulation (MORFAC-I) or when the front reaches the end of the domain (quasi-equilibrium condition: MORFAC-II), i.e. the morphodynamic time step is equal to the hydraulic time step when the turbidity current front is in the model domain, and it is larger than the hydraulic time step when the turbidity current body occupies the entire computational domain.

The thickness of the deposit between the benchmark case (MORFAC1) and the resultants after the applications of different values of MORFAC are reported in Figure 3.5. Overall there is a good agreement between the different applications of the model. In the case that MORFAC is applied after quasi-equilibrium conditions, the model slightly overestimate the deposit at the entrance of the domain for all the values of MORFAC. Figure 3.6 shows a zoom of the comparison of the bed elevation at the entrance of the

channel (first 100 m from the channel entrance) for the two test conditions considered in this study (MORFAC-I and MORFAC-II), for different values of MORFAC. The first figure (on top) shows the bed elevation at 15 hours, in the case that MORFAC is applied from the beginning of the simulation (MORFAC-I). For values of MORFAC equal to 2 and 5 there is a good agreement with the benchmark case, in the case of large values of the acceleration factor (MORFAC = 10), the model overestimate the final bed elevation. In the figure on the bottom are plotted the bed profiles for the cases in which MORFAC is applied after the current front reaches the end of the domain (MORFAC-II). In this case, for all the values of MORFAC, the model slightly over estimates the bed level.

The median diameter (D_{50}) of the deposit at the end of the simulations is shown in Figure 3.7 for all cases investigated. The first figure on the top is the benchmark case (MORFAC1), while on the left panel are the simulations in which MORFAC is applied from the beginning of the simulations (MORFAC-I) and the right panel are the stratigraphy profiles with MORFAC applied after the front reaches the end of the domain. The model for all the simulated cases is able to capture the downstream sediment fining tendency. Small values of MORFAC shows a better agreement with the stratigraphy of the benchmark case.

Two-dimensional field-scale application – wavy bed

In this case a 1,000 m long two-dimensional channel with wavy bed for the first 500 m from the inlet and plane bed downstream is considered. The initial bathymetry is shown in Figure 3.8. The computational domain has a resolution of 3 m and the near-bed grid size is 5 cm; the time step is chosen as 0.2 s. A constant turbidity current enters the domain with longitudinal velocity of 0.8 m/s and total sediment concentration of 3%, the

initial grain size distribution is reported in Table 3.1. The turbidity current reaches quasi-equilibrium conditions after 24 minutes of flow. The total simulation time is 12 hours.

The simulated bed elevation profile after the application of a morphological acceleration factor of 2 shows a very good agreement with the benchmark condition of MORFAC1 (Figure 3.9). The deposit thickness for the other cases with higher values of MORFAC deviates from the benchmark case (MORFAC1). In particular, the case of MORFAC 5-I, the model shows a better agreement with the expected profile compared with the case of high value of MORFAC (MORFAC10-I) when the bedform has shifted and its amplitude attenuated.

Figure 3.10 shows the bed elevation profiles at the end of the simulations near the entrance of the channel (x = 0 to 200 m) for MORFAC equal to 2, 5 and 10. The top panel of Figure 3.10 shows results for Case-I. As it has reported before, MORFAC 2 results in good agreement with the expected bed profile (MORFAC1); MORFAC = 5 or MORFAC = 10 results in profiles that are both shifted farther downstream in the longitudinal direction. Applying the acceleration factor after reaching quasi-equilibrium conditions in the domain results in better agreement with the benchmark profile for both MORFAC2-II and MORFAC5-II, while the case of MORFAC10-II causes the bed to shift to the downstream direction.

The bed evolution in time and the flow field after ten hours of flow is shown in Figure 3.11. The water surface is in phase with the bed and the bedforms are migrating upstream.

The grain size stratigraphy of the deposited strata is compared in Figure 3.12 for all the cases at 12 hours (end of the simulation). The turbidity current deposits coarser material

near the entrance and a strong tendency of downstream fining is observed. Coarse sediment is also deposited locally on the bedforms crest, as it can be observed from the stored stratigraphic record of the benchmark case. The model can successfully capture the downstream fining of the grain sizes of the deposited sediment. At the entrance of the channel, the bedforms growth rate is high enough to show that there is a formation of coarse deposit on top of the bedform crest and as the bedform moves upstream, the coarse sediment follows its shape. All the simulations capture this phenomenon.

Three-dimensional application at laboratory scale – minibasin

Results from the application of MORFAC to a laboratory-scale three-dimensional basin is presented here. This case is especially important because of the highly transient characteristics of the phenomenon by which the flow develops inside the basin. When the flows reach a basin, it reflects from the downstream end creating an upstream migrating bore, which eventually stabilizes (Lamb et al., 2004). For this case, the current is considered at quasi-equilibrium conditions then when the hydraulic jump stabilizes (after 15 minutes from the beginning of the simulation). The initial velocity of the turbidity current is 0.23 m/s and the inlet height is 5 cm. Initial conditions of the sediment mixture are reported Table 3.2. The basin has a circular diameter of 0.4 m and it is 0.3 m deep at the center (Figure 3.13). The computational domain is 1.22 m wide and 1.3 m long, with grid resolution 0.04 m and 0.03 m respectively. The near-bed grid cells have dimensions of 2 mm.

At the end of the simulation (60 minutes), there is a sharp increase of the bed elevation at the entrance of the basin of (Figure 3.14 – benchmark case). The bed elevation at the end of the simulation without the application of the morphological acceleration factor

(MORFAC1) is compared with the different cases of MORFAC application (Figure 3.15). The comparison is done by computing the difference in bed elevation after applying the MORFAC and the benchmark case.

The cases of MORFAC 2-I and MORFAC5-I shows satisfactory agreement with the benchmark deposit thickness. The deposit thickness is underestimated especially near the entrance when MORFAC 2-II, 5-II and 10-II are applied.

The turbidity current deposits coarse sediment along the entrance of the basin, and at the ponded area the deposit becomes finer and it follows the shape of the basin floor. The median diameter (D_{50}) of the deposit at the bed for all the tests is presented in Figure 3.16. The distribution of D_{50} of the deposited sediment is similar in all the cases.

3.3. SUMMARY

The morphological component of a 3D model of turbidity currents has been modified to incorporate a Morphological Acceleration Factor and storage of grainsize information in the deposited sediment. The morphological model has been applied to coastal (Esser at al., 2004; Roelvink, 2006), and fluvial processes, but not to turbidites.

Overall, the morphological acceleration approach implemented in this model gives a good agreement with laboratory measured results, when the factor is applied from the beginning of the simulation. On the other hand, field scale simulations show that applying MORFAC when the system reaches a quasi-equilibrium state would give a better match with the benchmark solution and a better agreement on the depositional pattern and its architecture. Based on the cases considered in this study, values of the morphological acceleration factor greater than 5 are not suggested.

Table 3.1: Grain size distribution of the turbidity current simulated for the test case of a wavy bed

Diameter [µm]	Fraction [%]
40	40
80	40
120	20

Table 3.2: Grain size distribution and concertation of the turbidity current for the 3D laboratory scale simulation on minibasin

Diameter, D [µm]	Fraction [%]	Concentration, C [%]
4.27	10.83	1.18
10.25	17.18	1.88
21.21	25.59	2.79
47.43	43.40	4.73
86.60	3.00	0.33

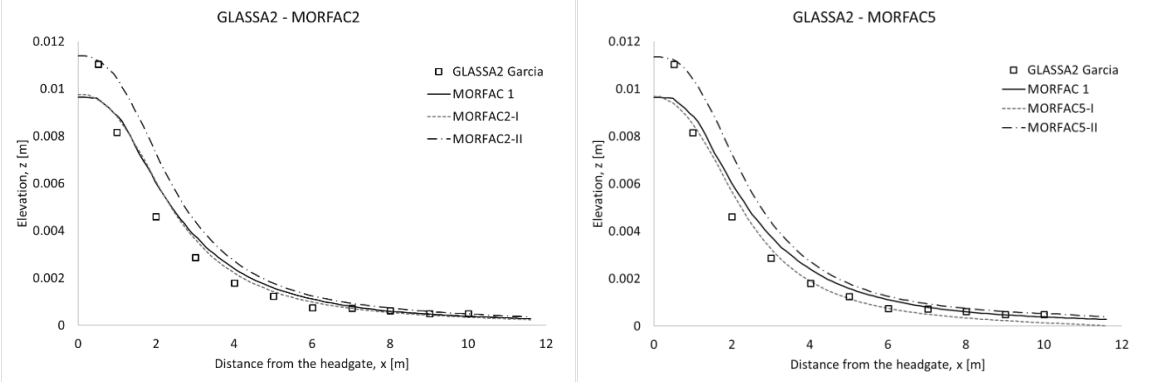

Figure 3.1: Final deposit thickness of a well-sorted turbidity current (GLASSA2, Garcia, 1993 – laboratory scale application). Left panel comparison with simulation result using MORFAC = 2, right panel using MORFAC = 5. MORFAC-I is when it is applied at the beginning of the hydrodynamic simulation (MORFAC2-I and MORFAC5-I); MORFAC-II when the front reaches the end of the domain (MORFAC2-II and MORFAC5-II)

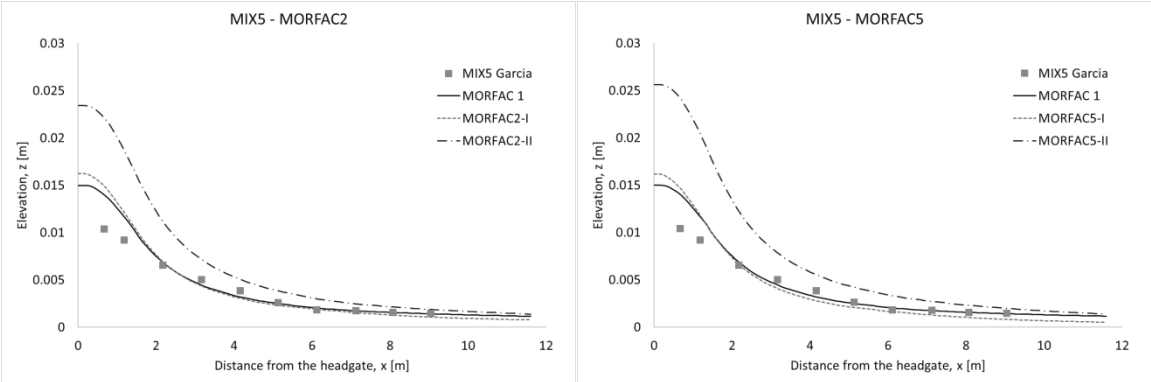

Figure 3.2: Final deposit thickness of a poor-sorted turbidity current (MIX5, Garcia, 1993 – laboratory scale application). Left panel comparison with simulation result using MORFAC = 2, right panel using MORFAC = 5. MORFAC-I is when it is applied at the beginning of the hydrodynamic simulation (MORFAC2-I and MORFAC5-I); MORFAC-II when the front reaches the end of the domain (MORFAC2-II and MORFAC5-II)

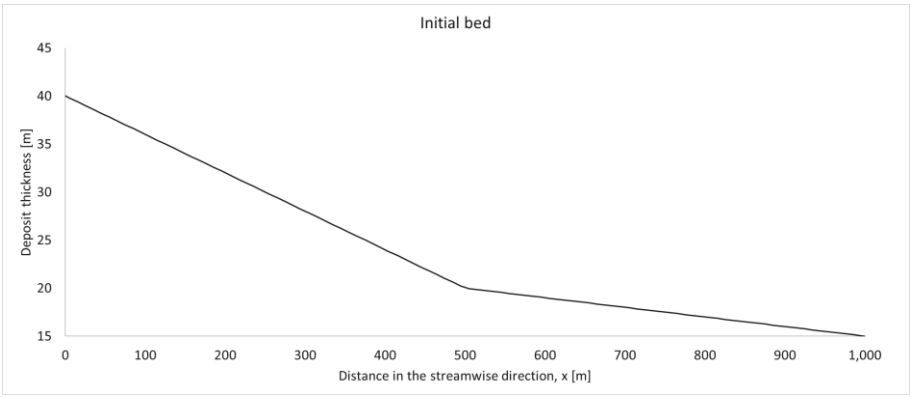

Figure 3.3: Initial bed profile for the simulations of the slope change

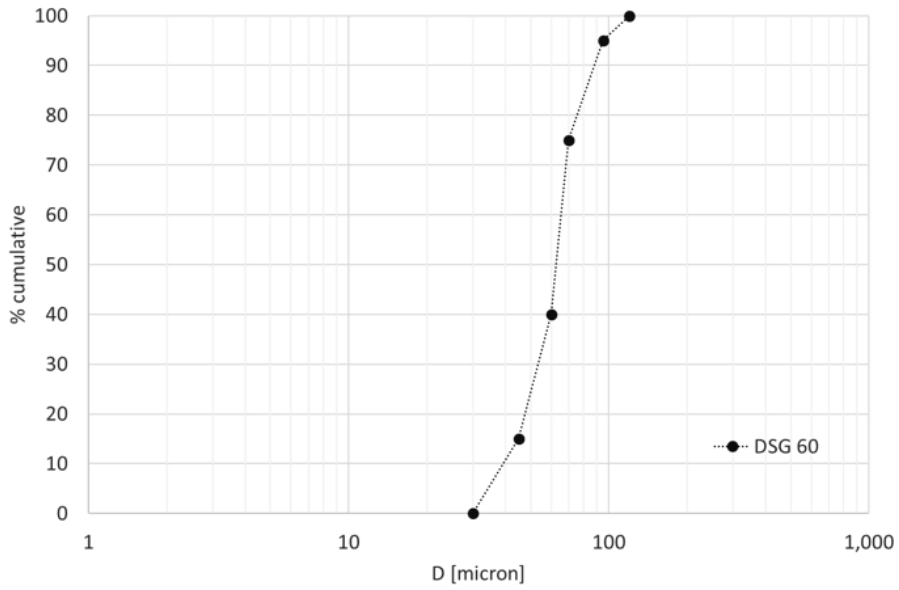

Figure 3.4: Sediment grain size distribution of the turbidity current characterized by mean grain size diameter of 60 μm, used for the 2D simulation of slope change

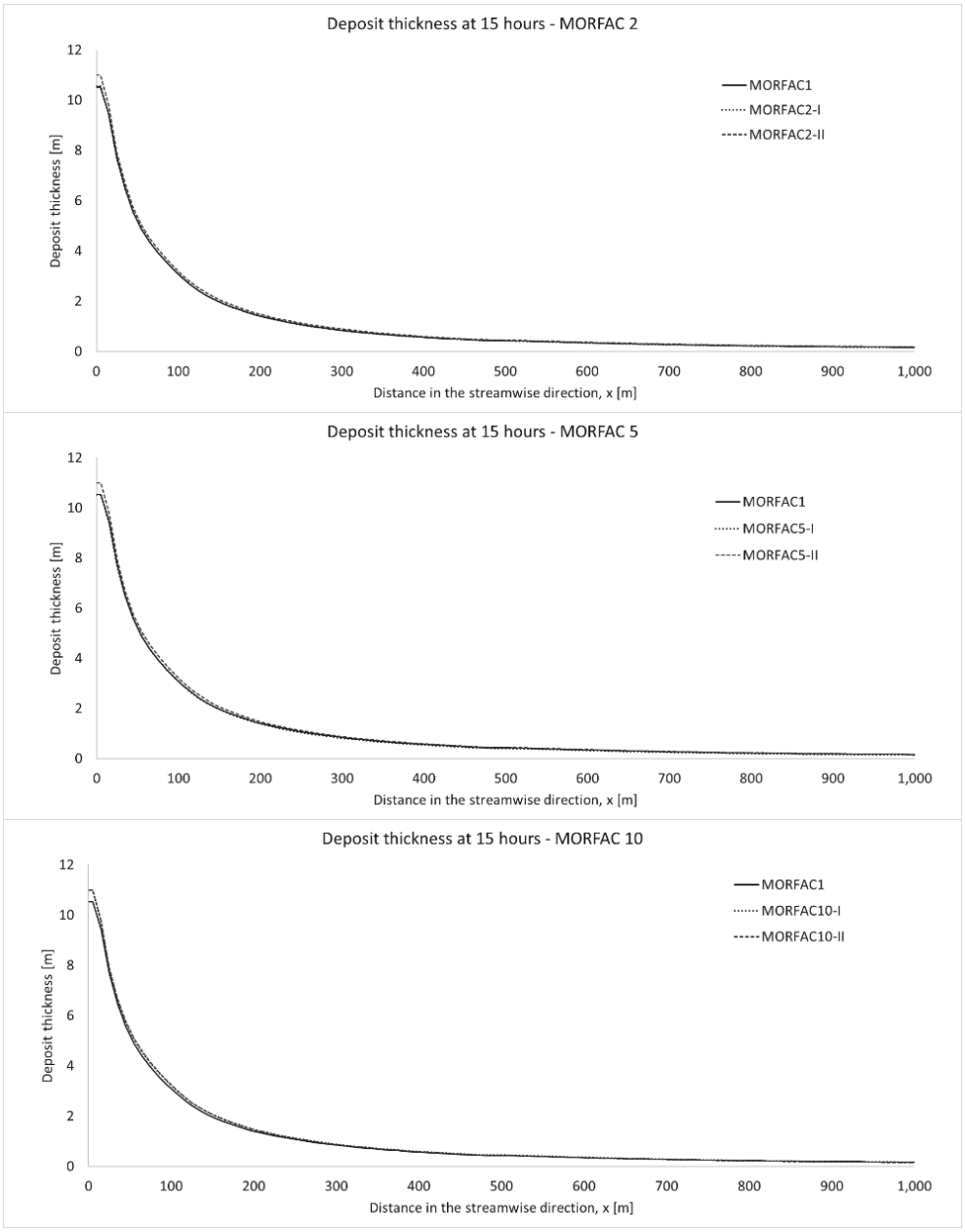

Figure 3.5: Deposit thickness in the case of slope change geometry, after 15 hours of simulated flow. MORFAC values are 2, 5 and 10. Comparison of the effect of the application of the morphological acceleration factor when the front reaches the end (dashed line, MORFAC-II), to the case of applying it from the beginning (dotted line, MORFAC-I)

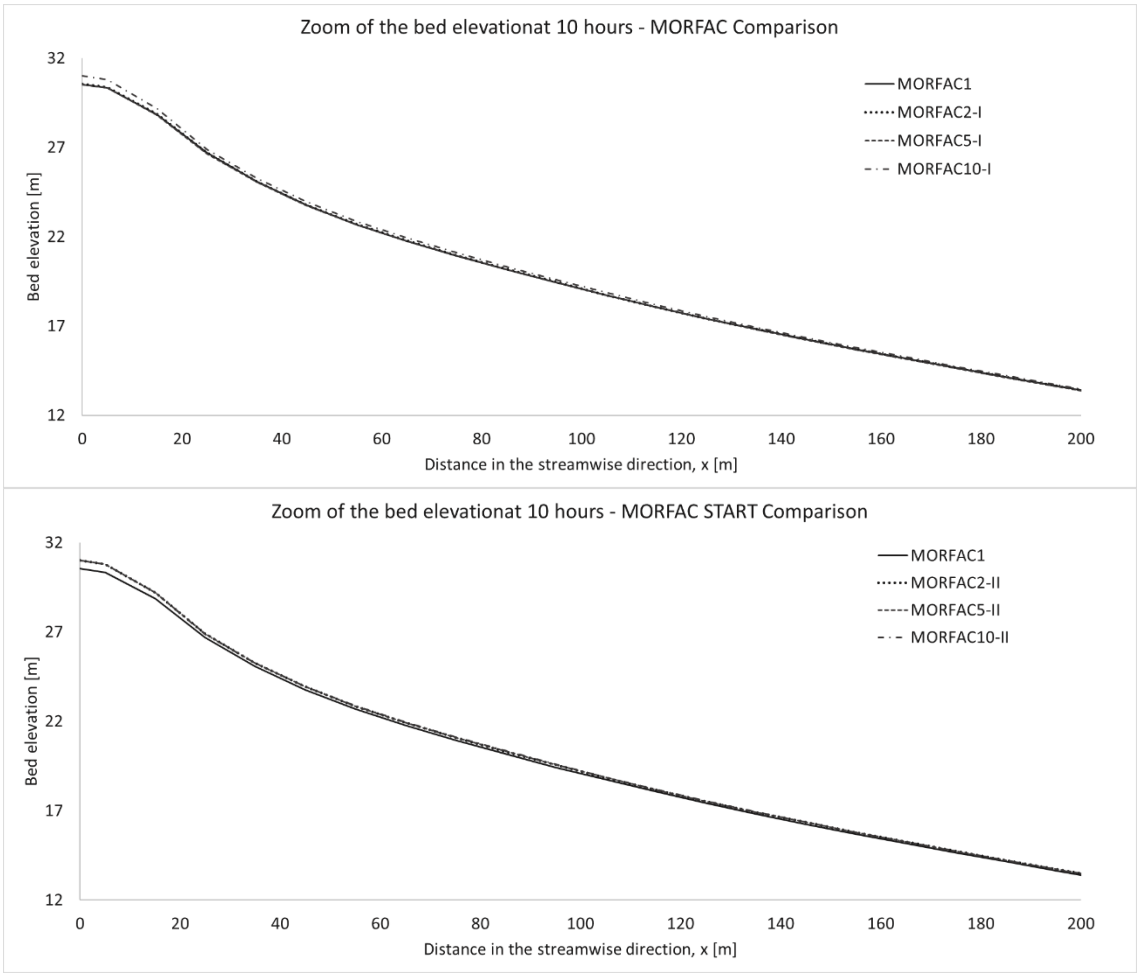

Figure 3.6: Comparison of the bed elevation profiles after 15 hours (zoom of the area between the channel entrance and x = 200 m) in the case of using MORFAC from the beginning (top, MORFAC-I) and when MORFAC is applied after the front reaches the end (MORFAC-II), for values of MORFAC equal to 2, 5 and 10

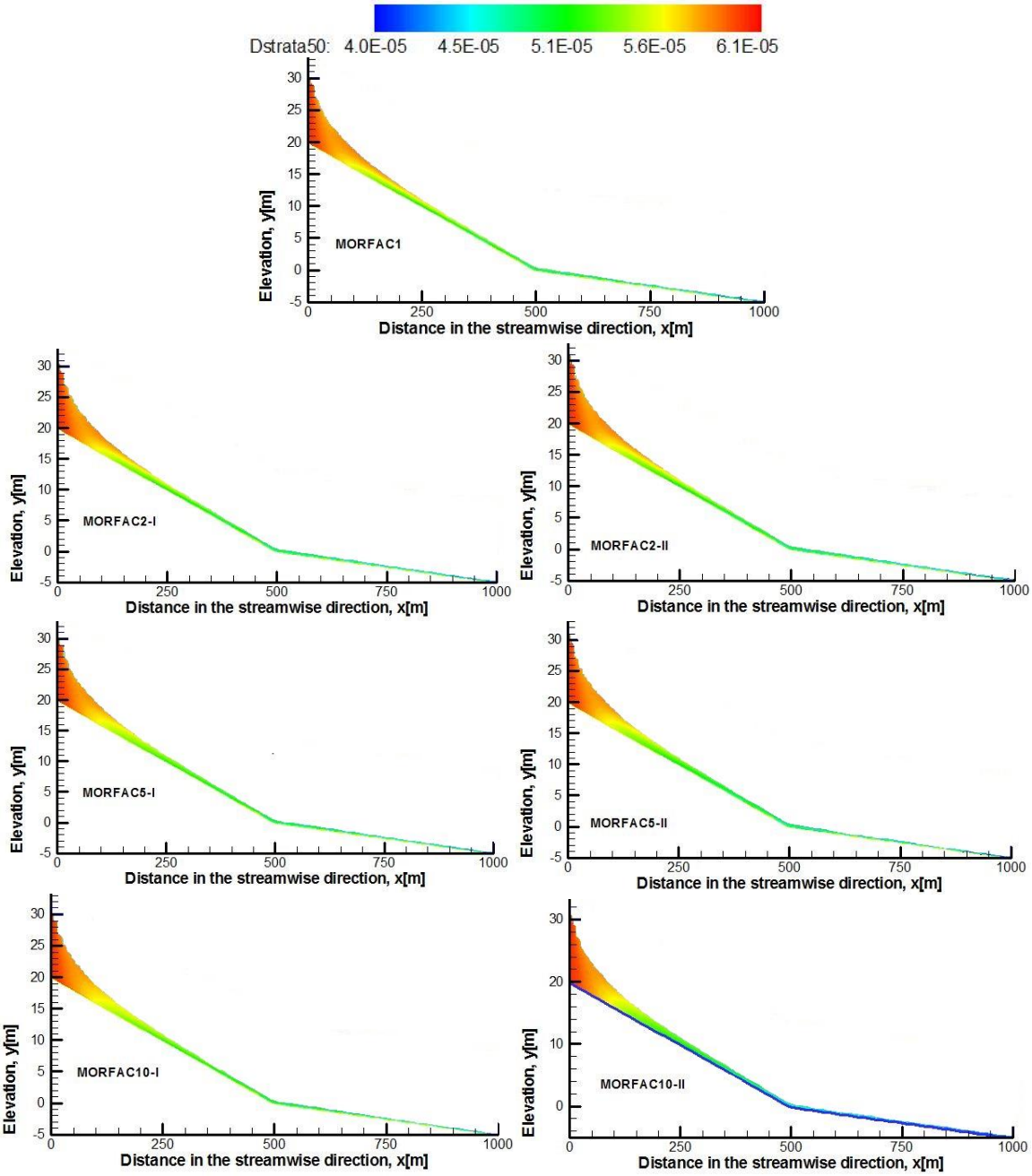

Figure 3.7 Median diameter of the stratigraphy of the deposit (D_{50}) after 15 hours. Left panel are the profiles in which MORFAC is applied from the beginning of the simulation (MORFAC-I), on the right panel MORFAC has been applied after the front reaches the end of the domain (MORFAC-II)

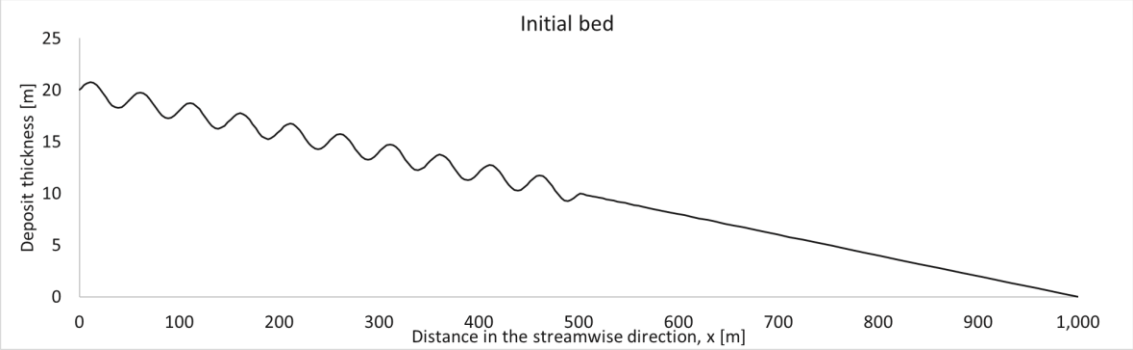

Figure 3.8: Initial bed profile for the 2D field scale simulation of wavy bed

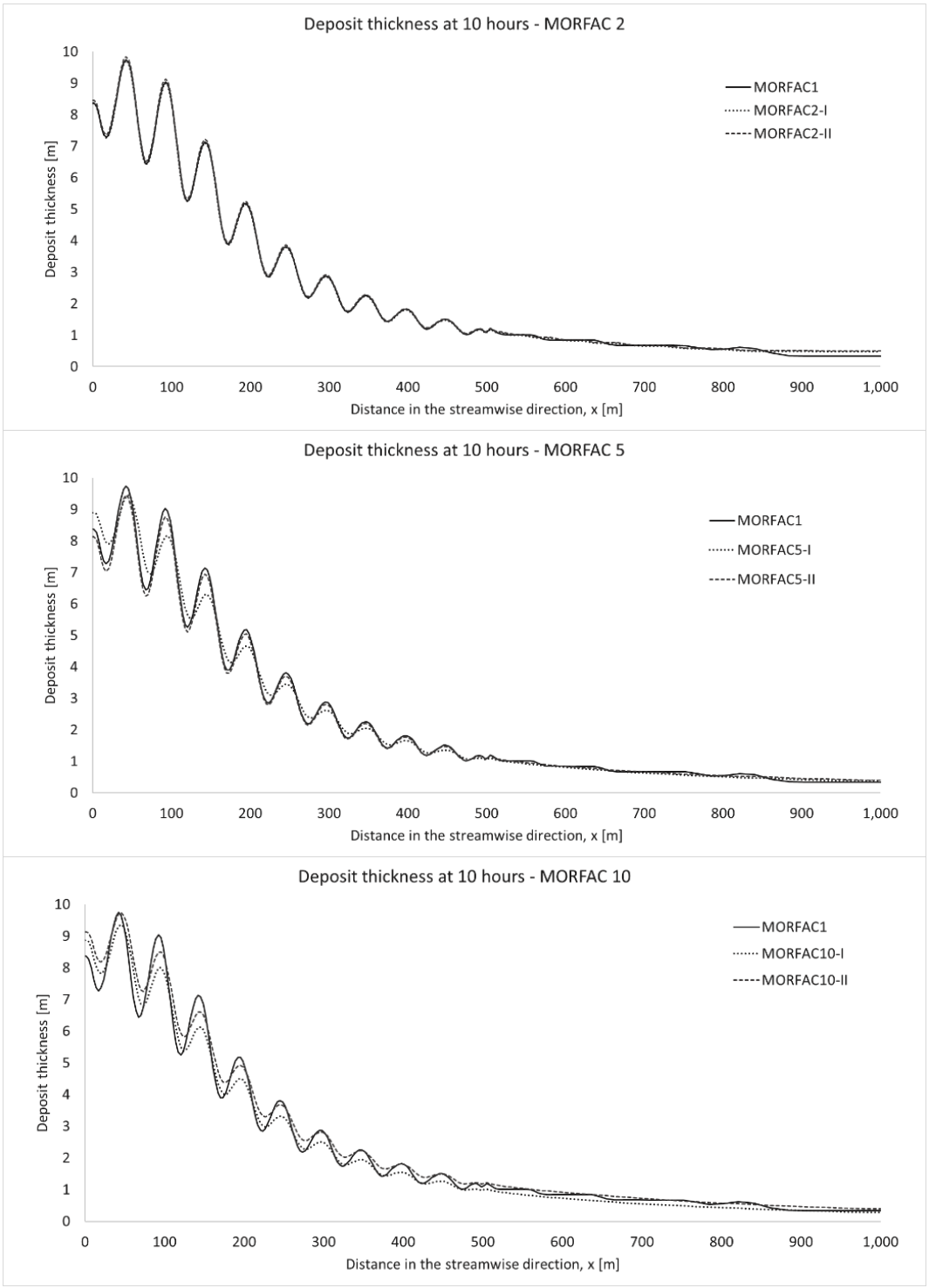

Figure 3.9: Comparison of the deposit thickness after 10 hours of simulated flow on a wavy bed. MORFAC values are 2, 5 and 10. Comparison of the effect of the application of the morphological acceleration factor when the front reaches the end (dashed line, MORFAC-II), to the case of applying it from the beginning (dotted line, MORFAC-I)

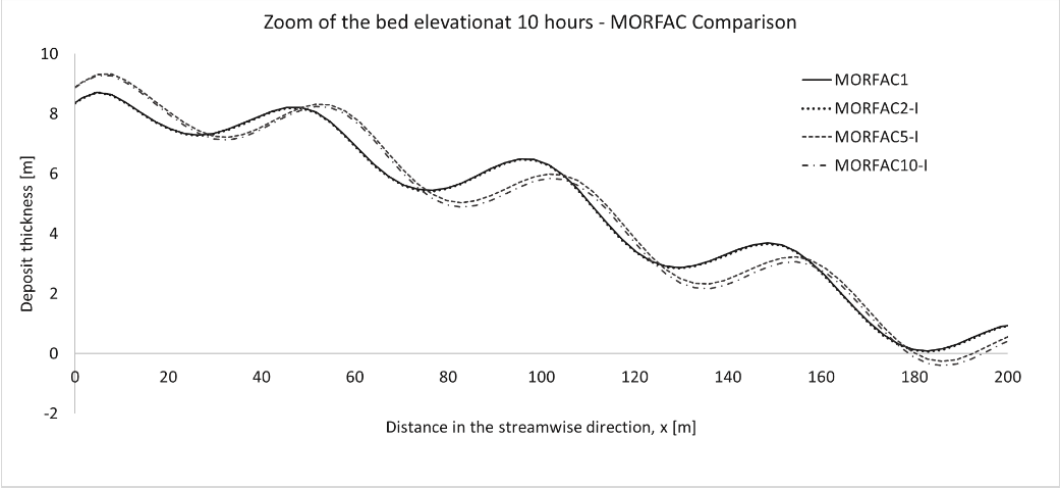

Figure 3.10: Comparison of the bed elevation after 10 hours of simulated flow on a wavy bed (zoom of the area between the channel entrance and x = 200 m) in the case of using MORFAC from the beginning (top, MORFAC-I) and apply MORFAC when the front reaches the end (MORFAC-II), for values of MORFAC of 2, 5 and 10

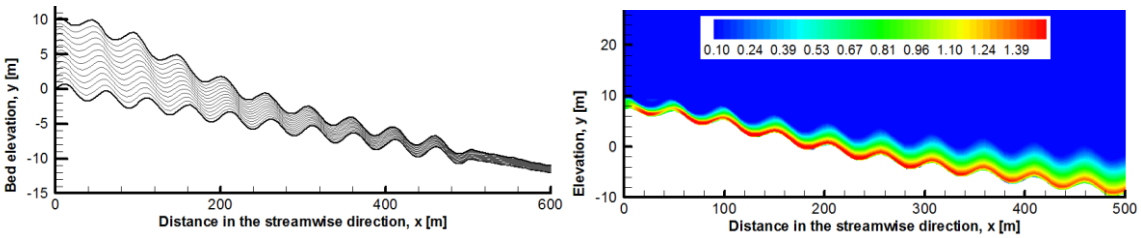

Figure 3.11: Bed elevation evolution and flow field of the simulation on a wavy bed, after 10 hours of simulated deposit (benchmark case)

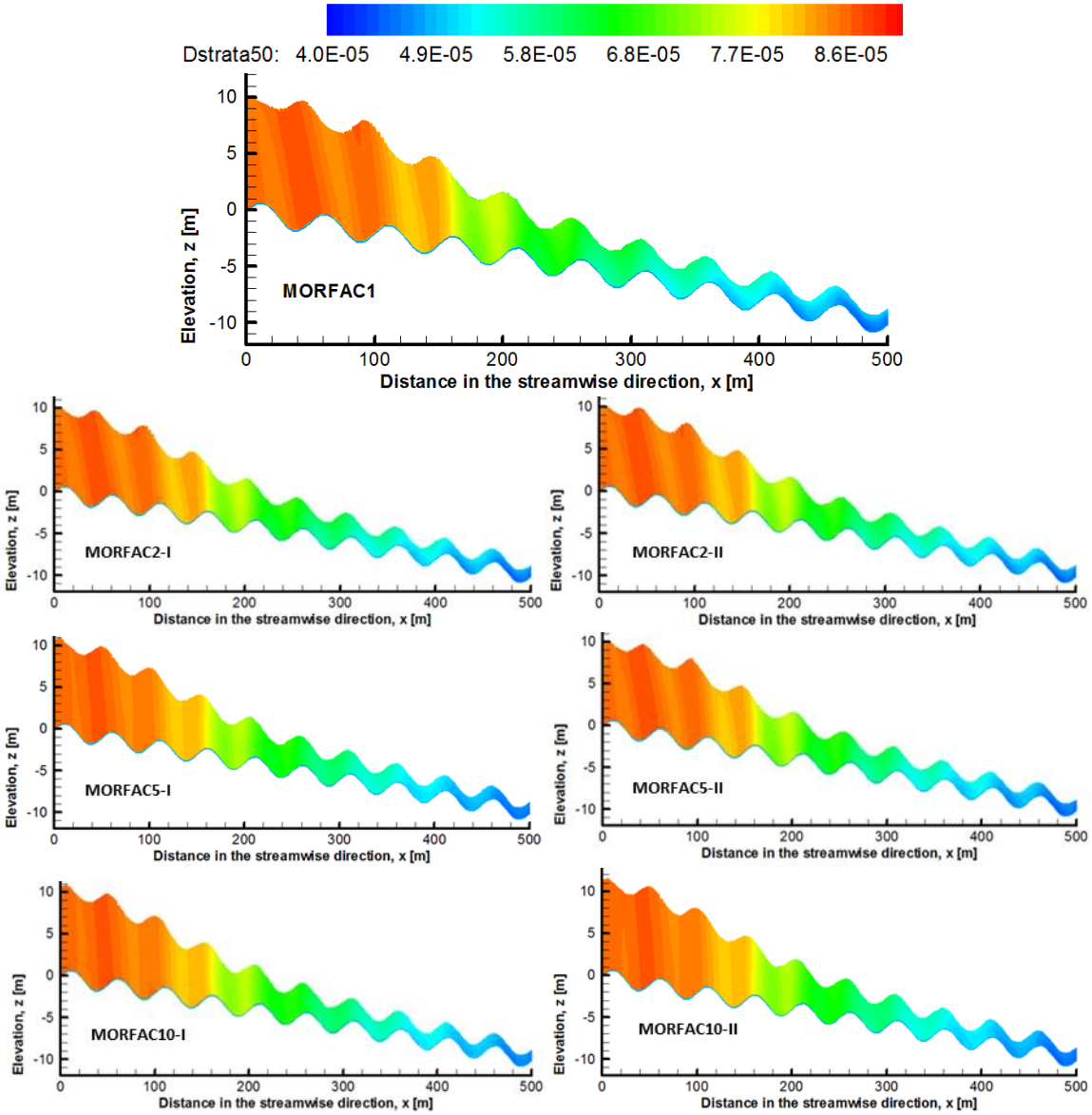

Figure 3.12: Stratigraphy of the deposit (D_{50}) after 10 hours of simulated flow. Zoom from the channel entrance to x = 600 m. On the left panel are simulations in which MORFAC is applied from the beginning (MORFAC-I), on the right panel MORFAC has been applied after the front reaches the end of the domain (MORFAC-II)

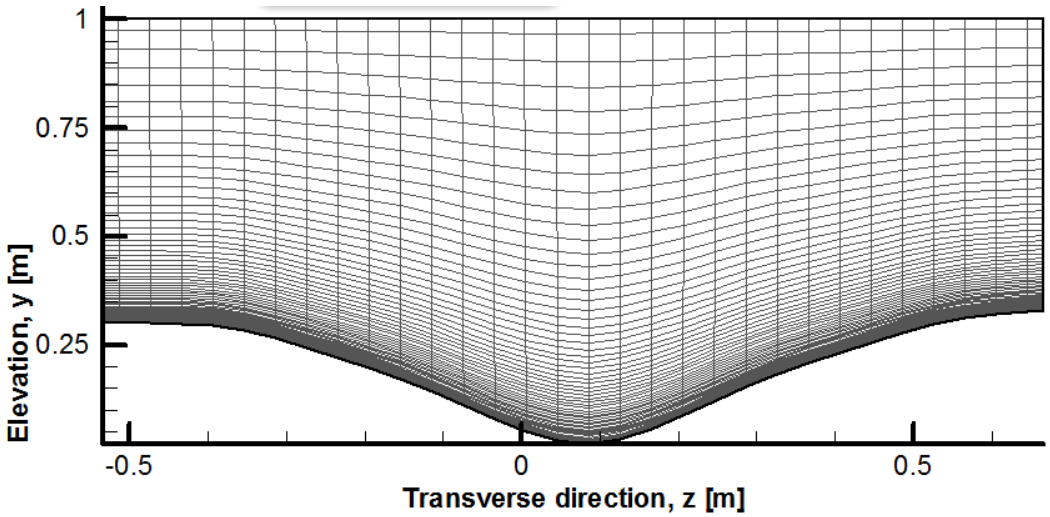

Figure 3.13: Initial computational domain of the simulation on a three-dimensional basin, at the deepest cross section (x = 3.1 m)

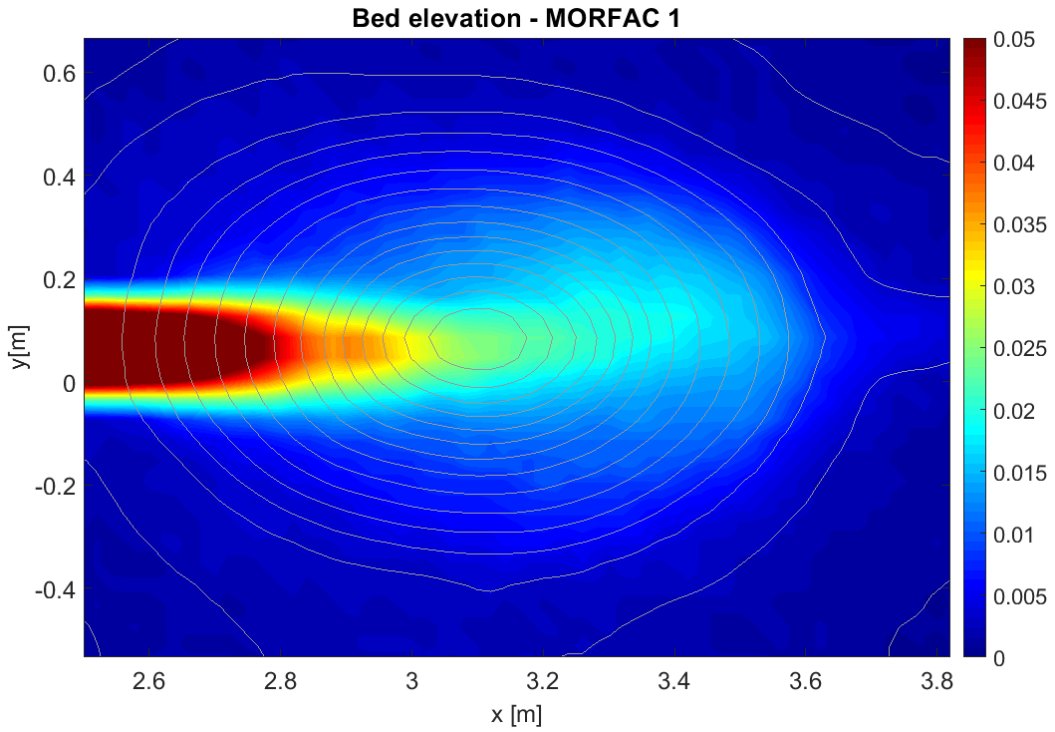

Figure 3.14: Bed elevation at the end of the three-dimensional basin (t = 60 minutes), at laboratory scale

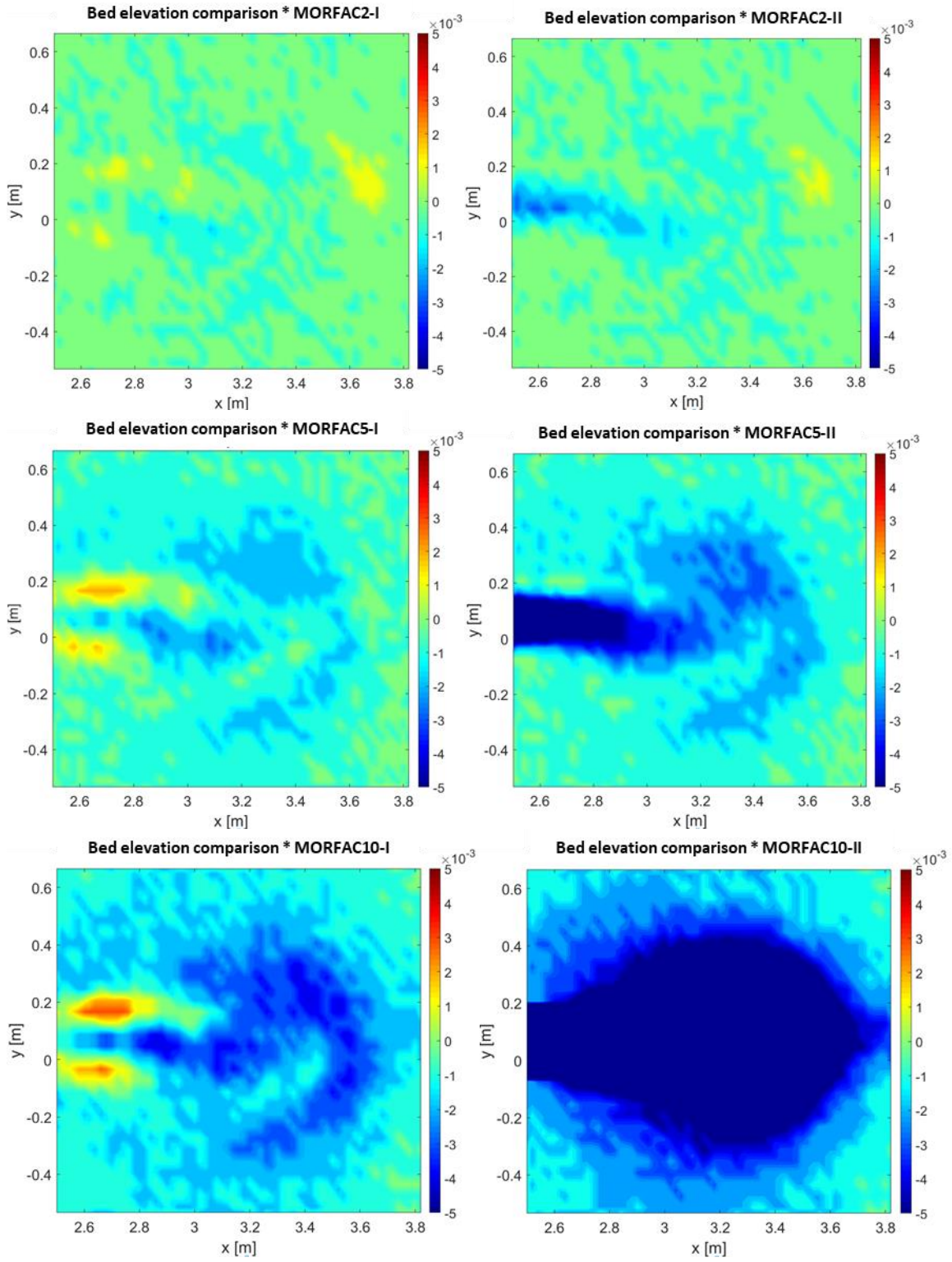

Figure 3.15: Comparison of the bed elevation at the end of the simulation (60 minutes) using different values for MORFAC. In the left panel are the simulations where MORFAC has been applied since the beginning (MORFAC-I), while on the right panel MORFAC has been applied after the hydraulic jump stabilize in the basin (MORFAC-II)

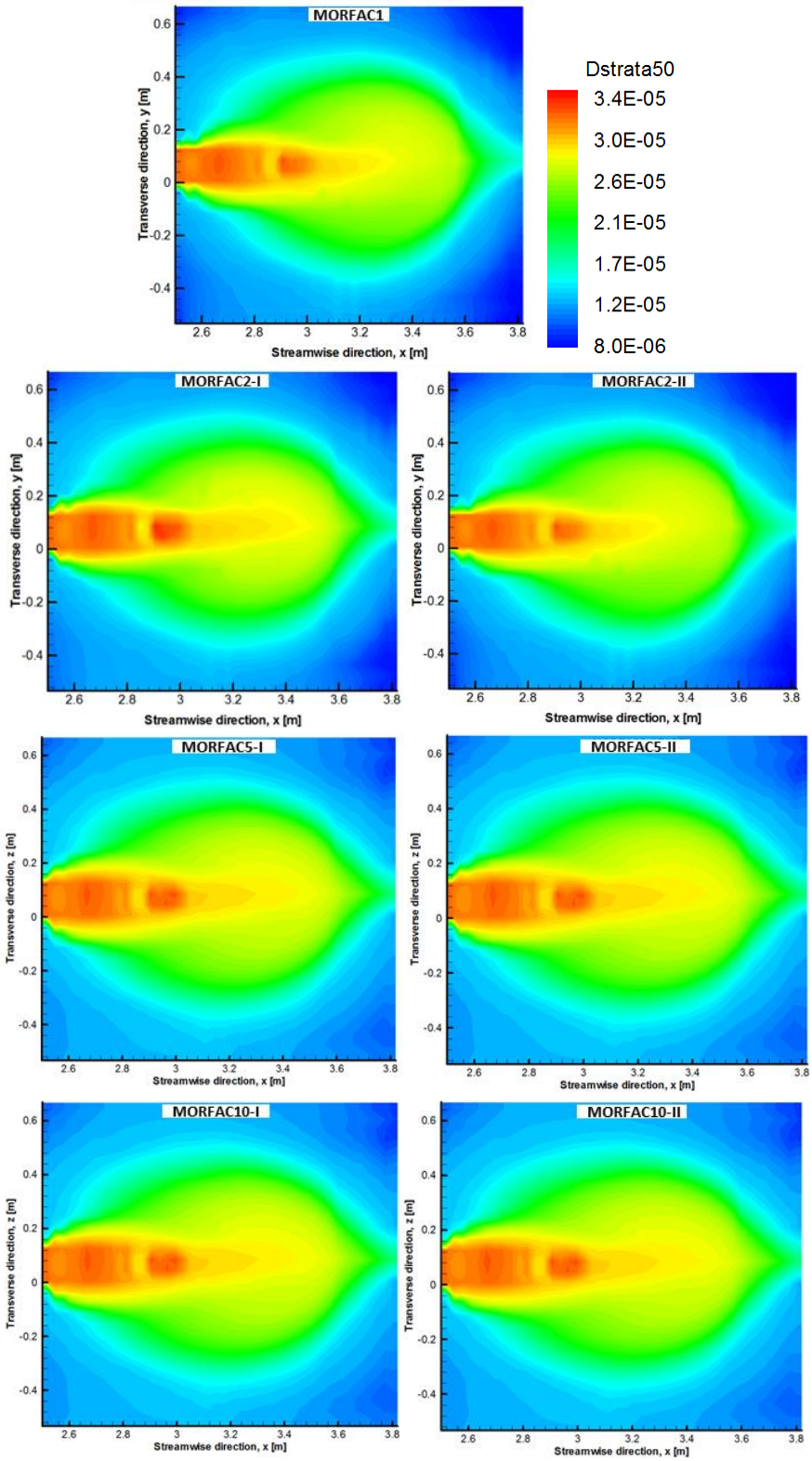

Figure 3.16: Spatial median diameter (D_{50}) of the deposit, for the laboratory scale basin at the end of the simulation (45 minutes). MORFAC (2, 5, 10) is applied from the beginning of the hydrodynamic simulation (left panel) and after the flow reaches quasi-equilibrium condition (right panel)

CHAPTER 4

THE 'FILL-AND-SPILL' MODEL IN SUBMARINE MINIBASINS

Minibasins can be found on the continental slope around the world. The continental slope of the Gulf of Mexico contains numerous mimibasins. They have an elliptical or spherical shape with a steep inlet or proximal zone followed by an almost horizontal ponded or basin zone. They are characterized by an overflow zone near the downstream basin lip, and they may or may not be connected by submarine canyons. Turbidity currents play an important role in moving coarse-grained material from the margins to the deep part of oceans and they are responsible for a range of morphological features on the seabed by siliciclastic sediment deposition. Minibasins have trapped thick sedimentary sections, some of which contain sand deposits with excellent hydrocarbon reservoir properties and for this reason the minibasins are economically important (e.g., Mahaffie 1994; Holman and Robertson 1994; Winker 1996; Beaubouef and Friedman 2000; Badalini et al. 2000). When turbidity currents reach a minibasin, they pond and start to deposit, developing a zone of very slow-moving flow, characterized by highly Froude-subcritical flow within the basin, where overflow may or may not occur (Lamb et al., 2006).

A variety of data sets are available from modern and ancient siliciclastic depositional system in the deep marine setting (outcrop and subsurface) to allow better understanding of the depositional process and the stratigraphic architecture of the deposit.

Traditionally, petroleum industry research on deep-water sandstone has been carried out by using conventional exploration data (2D and 3D seismic, well logs, cores) to better understand the formation and development of subsurface system and outcrops of ancient system (Badalini et al. 2000; Beaubouef and Friedman 2000; Pirmez et al. 2000). Most of these studies have been focused to develop a depositional concept, in part driven by the recognition that the deep-water Gulf of Mexico is a prolific petroleum province. These analyses allowed to combine the information of the shallow slope settings with the deeper subsurface formation, leading to a better understanding of controls on the stratigraphic evolution of this region (Prather et al., 1998). The process by which the turbidity currents fill the basins and erode channel is described by the 'fill-and-spill' conceptual model (Winker, 1996).

More recently, experimental and numerical modeling have been used to simulate the bed evolution in the submarine environment. Controlled laboratory and numerical modeling can overcome the limitations of direct field observation, due to the unpredictability and magnitude of these events. The objectives of these studies were to develop a better understanding of the submarine flow and morphdynamic processes by gathering more information on the turbidity current characteristics, and to investigate how geometry and concentration affect the depositional process. Lamb et al. (2004, 2006), Patacci et al. (2015), and Toniolo et al. (2006) conducted laboratory experiments to study fully ponded current within the minibasin (surge versus continuous current). They investigated characteristics and evolution of the turbidity current, and the effect of basin geometry on the depositional process.

The numerical simulations performed by Toniolo et al. (2006) had some inherent limitations associated with layer-integrated formulation, especially regarding the vertical structure of the flow. Khan and Imran (2008) developed a two-dimensional vertical-structure resolving model to overcome these limitations. They solved the Reynolds-Averaged Navier-Stoke equations using a finite volume method. They observed that the current inflow characteristics (flow velocity and suspended sediment concentration) can strongly influence the morphology of the deposit, and that larger sediment particles lead to deposition while finer particles lead to erosion (by keeping the other parameters constant).

Notwithstanding the progress made during the past decade, the dynamics of turbidity currents within minibasins and their depositional evolution are still poorly understood. The objective of the present work is to combine the information from field studies and seismic data on the depositional processes inside the minibasins, with the information from laboratory simulations on the 'fill-and-spill' process and conduct numerical simulations to study the evolution of the deposit in a minibasin, by systematically changing the flow conditions. The generalized 3D numerical model described in Chapter 2 is applied in 2D.

4.1. THE 'FILL-AND-SPILL' MODEL AND ACCOMMODATION SPACES

The 'Fill-And-Spill' Model

Turbidity currents are one of the principal agents by which clastic sediment have been transported and deposited in deep-marine environments. Turbidities – deposits created by turbidity currents – contain major hydrocarbon reserves in deep-marine sedimentary sequences (Weimer and Link, 1991, Mahaffie 1994; Holman and Robertson 1994; Pettingill, 1998a, 1998b; Barley, 1999, Badalini et al. 2000). A simplified conceptual model called 'fill-and-spill' has been used to describe the process by which the minibasins

are filled (Winker 1996; Beaubouef and Friedman 2000), creating sand-rich deposits. When a turbidity current enters a minibasin, it dives to the minibasin floor, moves forward eventually hitting the downstream end; part of the turbidity current can overspill while the rest creates an upstream migrating bore. A sharp interface separates the turbidity current from the sediment-free water above. The hydraulic jump created by the upstream migrating bore eventually stabilizes in space and the current starts to pond and deposit sediment inside the basin. Concentration and grain-size distribution of the sediment in suspension in the ponded zone tend to be relatively uniform in vertical and streamwise direction, resulting in a weak tendency toward downstream fining and an almost uniform deposit thickness in the basin (Lamb et al. 2006). When the accommodation space inside the basin decreases due to the deposition process, the turbidity current starts to overspill from the downstream lip and can create a localized area of erosion (Figure 4.1).

Accommodation spaces and sediment characteristics of the deposit fills

More recently, the discovery of hydrocarbon reservoirs in the deep waters, e.g., Campo Basin, Gulf of Mexico, West Africa, and Northwest Borneo, has led to significant research on the continental slopes facilitated by high-quality marine 3D seismic volumes (Beaubouef et al, 2003a-b; Prather et al., 2012). These data have enabled the development of depositional models by integrating seismic stratigraphy of the sea floor.

The characteristics of the flow and the geometry of the minibasin system played an essential role on the depositional process and on the shape of the deposit in submarine minibasins. Different accommodation spaces are defined as the spaces between various graded depositional profiles and they represent the amount of space available for sediment deposition. Line-sourced slope system can be described with the term ‘apron’ (Prather et

al., 2012), which in geomorphology is a laterally extensive deposit located at the base or in front of its source.

When a turbidity current reaches a basin, reflects at the downstream lip and starts to pond, the deposit is mostly located in the ponded accommodation space, which is the space confined by elevated margins on all sides, below the three geometrical maximum points of the basin (Figure 4.1). These deposits are mostly flat or gently sloping, and they result from the containment of the flow in the minibasin (Beaubouef et al., 2003a; Beaubouef and Friedmann, 2000; Beaubouef et al., 2003b; Toniolo et al., 2006a; Toniolo et al., 2006b). The ponded deposits are further sub-divided in 'low-relief' and 'high-relief' ponded apron. The 'low-relief' ponded apron occurs at a lower elevation relative to the spill point, and has the maximum thickness of the deposit at the center of the basin (Prather et al., 2012). Phases, in which sedimentation exceeds subsidence or when the accommodation space inside the basin decreases due to deposition, the space between the minibasin floor and the spill point decreases, and the turbidity currents eventually overspill. The depositional pattern changes with preferential sediment deposition in the proximal part of the entrance of the minibasin, with high deposit thickness located towards the entry-point channel (Prather et al., 2012). This type of deposit is called 'high-relief' ponded apron. 'High-relief' ponded aprons have reflectors that converge by baselap and thinning, and isochore planform with maximum thickness offset toward the entry-point channel.

Above the steeped-equilibrium profile formed across a series of filled ponded basins develops the perched apron, which is the deposit located in the healed-slope accommodation space (Prather, 2000). The maximum thickness of these deposits are offset updip from the basin center, they have a thinner deposit both seaward and landward, and

they are characterized by the presence of a bypass channel, sharp change of the slope (knick-points), and/or a “gather zone” at the basin exit point which distinguish them from the high-relief ponded aprons (Prather et al., 2012). On top of the healed-slope accommodation space, up to the highest stable graded-slope angle, is the slope accommodation space, which is influenced by the pore pressure within muds deposited on the slope and so it varies spatially. Slope accommodation space is not been investigated in this study.

4.2. LABORATORY SCALE APPLICATION OF THE MODEL TO SIMULATE THE ‘FILL-AND-SPILL’ PROCESS

The validated model (Toniolo et al., 2006a, Figure 2.10 and Figure 2.11) is applied at two-dimensional laboratory scale to investigate the depositional pattern and the current characteristics (concentration and velocity) inside the basin as the basin fills. A turbidity current with initial sediment concentration of 5% by volume is simulated for 5 hours, using the initial conditions (Table 4.1) and geometry (Figure 4.2) analogous to the one used for the validation of the model (Chapter 2).

The turbidity current enters the basin and reaches the downstream end creating an upstream migrating bore (Figure 4.3A), which eventually stabilizes (Figure 4.3B). A hydraulic jump separates the entrance zone characterized by super-critical flow and the ponded area downstream, in sub-critical condition. The sediment concentration inside the basin is almost constant in the vertical direction, a sharp interface separates the turbidity current from the clear water above (Figure 4.3B), and in this phase the current density increases in the basin. The turbidity current is strongly depositional inside the basin, depositing preferentially in the ponded zone and in the upstream part of the basin, reaching equilibrium conditions for the slope. As the bed elevation increases, the available

accommodation space inside the basin decreases, and the interface between the turbidity current and the clear water above moves in the upward direction, until the current eventually starts to overspill from the downstream lip (Figure 4.3C).

As the turbidity current overspills from the downstream lip, the hydraulic jump moves in the downstream direction (Figure 4.3D), and the concentration in the ponded zone is less uniform in the vertical direction compared with the previous ponded phase. The turbidity current reaches an equilibrium slope by depositing sediments at the entrance of the basin (Figure 4.4). In the ponded area the deposit is tabular. As the turbidity current starts to overspill from the downstream lip (red line in Figure 4.4 marks the bed elevation at the time when the current starts to overspill from the basin), the thickness of the deposit inside the basin decreases.

In this laboratory scale simulation, the geometry and the turbidity current characteristics do not allow the clear formations of the aprons described by Prather et al. (2012). It has been observed that one of the conditions for laboratory scale simulations to be able to give a good representation of the field condition is that the water generated by detrainment does not affect the flow field in the ambient fluid above the submerged turbidity, and therefore, it can be assumed to be negligible (Toniolo et al., 2006a). In the numerical simulations at laboratory scale, the clear water above the turbidity current is less than 1 m deep, while in the field the turbidity current is usually submerged by kilometers of clear water. This might be one of the reasons why the accommodation spaces fail to develop. Furthermore, the scale of the laboratory scale applications compared with field conditions can affect the development of the turbulence, and therefore, the deposit.

4.3. FIELD SCALE APPLICATION

Field scale applications are critical to overcome the limitations of laboratory scale simulations (Lamb et al., 2006) and to gain a better understanding of turbidity current dynamics. Two-dimensional simulations have been performed in the intraslope salt-withdrawal basins or minibasins in the Brazos – Trinity Rivers system, in the Gulf of Mexico. This area can be described as a structurally-ponded sediment body within three salt-withdrawal minibasins (I, II, IV), a graben (III) (Winker 1996). This study has considered turbidity currents entering Basin II and developing in Basin IV, by moving through the western channel that connects Basin II with Basin IV.

A deep series (series 10, series boundary are high-amplitude reflectors, used to determine the depth and orientation of rock formations) of the transect through Brazos-Trinity Basin II and Basin IV, and the western channel that connects the two basins (Prather et al. 2012), has been used for these simulations, as shown in Figure 4.5.

Different initial conditions (Table 4.2) have been considered to investigate the effects of the grain size distribution and of the discharge on the deposit shape, and in specific the formations of ponded and perched aprons (Prather et al. 2012). Uniform and mixture conditions for four different sediment grain size diameters (D = 20, 40, 60, and 80 μm) have been considered for a total simulation time of two days. The grain size distributions of the turbidity current used for the case of sediment mixture are shown in Figure 4.6.

The current thickness (8 m) has been chosen based on the morphology of the upstream basin (Basin II) to archive a half-filled upstream cross section. A benchmark inflow velocity has been chosen (2 m/s) for all the simulations involving different grain size distribution (Figure 4.6, uniform material: uni20, uni40, uni60, and uni80; and

mixture: mix20, mix40, mix60, and mix80). In order to investigate the effect of the discharge also a small (u = 1.5 m/s, simulations: uni60-s and mix60-s) and a large inlet velocity (u = 2.5 m/s, simulations: uni60-l and mix60-l) have been considered.

The computational domain has been defined by 196 x 101 nodes, the grid size in the longitudinal direction being 200 m and the near bed grid size = 0.5 m in the vertical direction.

Results and discussions

In this section the results of the simulations reported in Table 4.2 are presented for both uniform sediment and sediment mixture. First, the results of the investigation of the effect of different mean diameter of the sediment in turbidity currents are presented. Then, the comparison of the benchmark case of mean size diameter of 60 μm (uniform and sediment mixture) for a small and a large current is shown.

Effect of the grains size

Figure 4.7 reports the total sediment concentration after two days for the four mean sediment diameters. The total concentration in the color map ranges between 0 and 0.005%. Both the conditions of turbidity current with uniform material (left panel Figure 4.7) and sediment mixture (right panel) are presented, with characteristic diameters of 20, 40, 60, and 80μm. The inlet velocity (2 m/s) and the total initial concentration (5%) for all the simulations were the same. The black line represents the initial bed level.

The concentration of the turbidity current with the finest grainsize (uni/mix20) after two days, is high in both Basin II and Basin IV (Figure 4.7A), which indicates that the system does not trap sediment, and the current bypasses the basins. The upstream migrating

bore generated from the reflection off the downstream flank of the basin, stabilizes at a location that is in the proximal entrance for both the basins.

In the case of characteristic diameter of 40μm (uni40 and mix40), the concentration in Basin II is higher than in Basin IV. A considerable amount of sediment reaches Basin IV and the current overspills from the downstream end of Basin IV (Figure 4.7B). Hydraulic jumps form in both basins and are located downstream compared with the previous case (uni20 and mix20).

With the increase of the sediment characteristic diameter (D_g = 60 μm) the hydraulic jump in Basin II moves farther in the downstream direction (Figure 4.7C). The concentration in both Basins decreases considerably. In the case of sediment mixture (mix60), a more sediment reaches Basin IV compared to the case with uniform sediment due to the presence of finer sediment in the mixture at the inlet.

In the case of coarse turbidity currents (80μm, Figure 4.7D), the sediments are mostly trapped in Basin II for both cases (uniform and sediment mixture).

Figure 4.8 presents the bed profiles every 12 hours, until the end of the simulation (2 days). The deposit from the turbidity current driven by the finest sediment is very thin in Basin II, creating the so-called 'low-relief' ponded apron (Figure 4.8A), which is in accordance with the fact that most of the sediment leaves the system (Figure 4.7A).

The deposit pattern in Basin II from turbidity currents with characteristic diameter of 40 μm is similar for the cases of uniform and sediment mixture. Thick deposit is mostly located in the ponded zone of Basin II (Figure 4.8B) until one day of simulated flow ('low-relief' ponded apron). Afterwards, the formation of thick deposits is observed in the

upstream part of Basin II ('high-relief' ponded apron). The deposit thickness in Basin IV, also for this case, is very modest.

In the case of turbidity current driven by uniform sediment of D_g = 60 μm (uni60) the deposit is mostly located in the ponded zone of Basin II, with relatively thick deposit at the entrance after one day of simulated flow (Figure 4.8C). With time, morphological features appear on the deposit, which develops as a localized increase of the bed elevation in the proximal flank of Basin II occurs creating a slope discontinuity. In the case of sediment mixture (mix60), the deposit is thick and tabular, located on the proximal flank of Basin II. Small morphological features developed after two days of simulated flow.

Figure 4.8D represents the evolution of the bed elevation for the case of turbidity currents with characteristic sediment diameter of 80 μm (uni80 and mix80). In agreement with the concentration field (Figure 4.7D), the sediment primarily deposits at the entrance of the Basin II, creating tabular deposits.

As described, turbidity currents with uniform material of 40 μm and 60 μm (uni40 and uni60), and the turbidity current with sediment mixture with characteristic diameter of 40 μm (mix40) initially create a deposit that is thicker in the deepest part of the basin (Figure 4.8B and C) until 24 hours, which can be identified as a 'low-relief' ponded apron. With time, the deposit thickness increases in the proximal flank of the basin creating 'high-relief' ponded aprons. On the other hand, coarse turbidity currents (uni80 and mix80) deposit preferentially at the entrance of Basin II creating tabular deposits.

Figure 4.9 shows the grain size distribution of the deposit (median diameter, D_{50}) in Basin II for the cases of turbidity currents driven by sediment mixture, after two days of

simulated flow. The thin layer below the constructed stratigraphy represents the information of the initial grain size distribution at the bed.

For the case run with fine sediment (mix20, Figure 4.9A), the deposit is mostly 'low-relief' ponded apron and coarser than the parental material. The case of turbidity current with characteristic diameter of 40μm (mix40), shows fine deposit at the entrance and in the downstream end of Basin II (downstream of the hydraulic jump, ponded zone - Figure 4.7). Coarse and thick deposit is located at the deepest part of Basin II (Figure 4.9B). As mentioned earlier, morphological features form at the bed characterized by coarse sediment, which moves in the upstream direction.

The deposit created by a turbidity current driven by characteristic diameter of 60 μm (mix60) is mostly tabular, with fine material in the ponded zone (downstream of the hydraulic jump) and coarse deposit at the proximal flank of the basin (Figure 4.9C), with a tendency of downstream fining.

The stratigraphy of the deposit of the coarsest sediment case investigated in this study (mix80) is reported in Figure 4.9D. Coarse deposit is preferentially located at the entrance of Basin II, with tendency of downstream fining.

Effect of the discharge

In order to investigate the effect of the inflow discharge on the depositional pattern, three different values of inflow velocity have been considered (u = 1.5 m/s, 2 m/s and 2.5 m/s). The characteristic sediment grain size diameter considered in these model runs is D_g = 60 μm, for both cases of uniform and sediment mixture. Total flow duration is two days. Initial bathymetry and all other parameters are kept equal to the previous section.

The total concentration field of the sediment is reported in Figure 4.10. The left panel shows the cases of uniform material, the right panel shows the cases of runs made with sediment mixture. The top panel is the result of a simulation after two days, with small velocity (u = 1.5 m/s), the panel in the middle is the result of the cases with medium velocity (u = 2 m/s), and the bottom panel represents the case with high velocity (u = 2.5 m/s). The increase of the current velocity, and as a consequence the discharge, significantly increases the sediment concentration is the domain (Figure 4.10). Turbidity currents with sediment mixtures result in overspilling basin II with a higher concentration and reaching Basin IV (Figure 4.10 – left panel), compared with the case of uniform material (Figure 4.10 –right panel).

In the case of small inflow velocity (u = 1.5 m/s; uni60-s and mix60-s), most of the sediment is trapped in Basin II and only a small amount of turbidity current reaches Basin IV (Figure 4.10A). With increasing of the inflow velocity and as a consequence the current discharge, the sediment concentration in Basin IV increase (Figure 4.10B). Only for the largest discharge case (mix60-l, u = 2.5 m/s, Figure 4.10C), there is significant overspill of the current from the downstream lip of Basin IV (Figure 4.10C, right panel). The location of the bore in Basin II does not change with the increase of the turbidity current intensity.

The deposit profiles are reported in Figure 4.11. For all the cases, the deposit is preferentially located in Basin II. The deposits of the small turbidity currents (Figure 4.11A, u = 1.5 m/s; uni60-s and mix-60-s) is located mostly at the entrance of Basin II and in its deepest part. With the increase of the inflow velocity there is an increase of the deposit thickness in the ponded zone, compared with the previous case. In particular, the depositional pattern of the medium turbidity current (uni60) until one day of simulated flow

of uniform material, show the formation of ‘low-relief’ ponded apron. After that the maximum deposit thickness moves in the upstream part of the ponded accommodation zone, creating ‘high-relief’ ponded apron. In the case of sediment mixture (mix60), the deposit is located at the proximal zone of Basin II; it is thick and tabular.

The uniform turbidity current with large inflow velocity (uni60-l, Figure 4.11C) creates ‘low-relief’ ponded apron during the first day of simulated flow; after that (up to two days), the maximum deposit thickness increases in the upstream part of Basin II, creating ‘high relief’ ponded apron. After two days of simulated flow the deposit at the entrance of Basin II increases in thickness, reaching above the spill point. This type of deposit can be identified with perched aprons. The case with same inflow conditions, but characterized by sediment mixture (Figure 4.11C – right panel), creates thick and tabular deposit that is mostly located at the entrance of Basin II.

The grain size stratigraphy of the deposit (Figure 4.12) shows a tendency of downstream fining for all the cases (mix60-s, mix-60 and mix60-l). As Basin II fills with sediment, coarse sediments are deposited following an upstream migrating pattern.

4.4. SUMMARY

The process by which submarine minibasins are filled by turbidity currents is called the ‘fill-and-spill’ model. Conventional exploration data (2D and 3D seismic, well logs, cores) are used to develop depositional models to describe the evolution of the bed deposit inside the minibasin. A two-dimensional numerical model is applied at laboratory and field scale application to develop insight into the depositional pattern and stratigraphy of minibasin turbidite.

The laboratory scale numerical simulations show the evolution of the ‘fill-and-spill’ scenario, the creation of the hydraulic jump that moves in the upstream direction until it

stabilizes, creating a zone of constant concentration in the vertical direction (ponded zone). The turbidity current starts to overspill when the accommodation space inside the basin decreases. As the current starts to overspill the thickness of the deposit inside the basin decreases, following the depositional model developed for the minibasins in the Gulf of Mexico.

The model has been applied at field scale using a two-dimensional initial bathymetry from Prather et al. (2012). The model has been applied with uniform and sediment mixture. The turbidity current, similar to the laboratory scale simulations, develop a hydraulic jump after it reflects from the downstream lip of the basin. A zone characterized by small or negative velocities develop near the bed (reflection zone). As the turbidity current fills the basin the hydraulic jump moves in the downstream direction. When accommodation space inside the basin decreases, the turbidity current starts to overspill from the downstream end, and it may create a zone of erosion. The turbidity current initially creates a 'low-relief' ponded apron in Basin II. As it starts to overspill the deposit is preferential in the upstream part of the ponded accommodation space, the so called 'high-relief' ponded apron, until it creates perched aprons which are deposits located above the basin spill point.

The upstream basin traps most of the turbidity current sediment, especially the ones containing coarser sediments. In the case of fine sediment mixture, the fine sediments overspill from the downstream lip of the domain. Turbidity currents with larger characteristic diameter deposit preferentially at the entrance of the basin, compared with those with a smaller diameter. Overall, the grain size distribution of the deposit in Basin II does not change much in the vertical and longitudinal direction. The deposit thickness

increases with an increase of the current intensity, but the shape and the grain size distribution of the deposit do not change. In the case of smaller grain sizes (40 μm and 60 μm) there is a formation of morphological features at the bed, due to the formation of 'low-relief' and 'high-relief' ponded aprons. Coarser turbidity currents create a thick and tabular deposit at the entrance of the computational domain (Basin II).

Table 4.1: Initial conditions of two-dimensional laboratory scale application to simulate the 'fill-and-spill' model

Parameters	
Inflow current thickness, h_{in} [cm]	1.00
Inflow velocity, u_{in} [m/s]	0.10
Inflow sediment concentration, c_{in} [m^3/m^3]	0.05
Geometric mean size of particles, D_g [μm]	45.00
Submerged specific gravity, R	1.65
Inflow Fr_d	1.11
Total simulation time [min]	60.00

Table 4.2: Initial conditions of two-dimensional field scale simulations

Parameters	**mix/uni 20**	**mix/uni 40**	**mix/uni 60**	**mix/uni 80**	**mix/uni 60-s**	**mix/uni 60-l**
Inflow current thickness, h_{in} [m]	8	8	8	8	8	8
Inflow velocity, u_{in} [m/s]	2	2	2	2	1.5	2.5
Inflow sediment concentration, c_{in} [m^3/m^3]	0.05	0.05	0.05	0.05	0.05	0.05
Geometric mean size of particles, D_g [μm]	20	40	60	80	60	60
Geometric standard deviation, σ_g	1.6	1.33	1.32	1.27	1.32	1.32
Submerged specific gravity, R	1.65	1.65	1.65	1.65	1.65	1.65
Total simulation time [day]	2	2	5	2	2	2

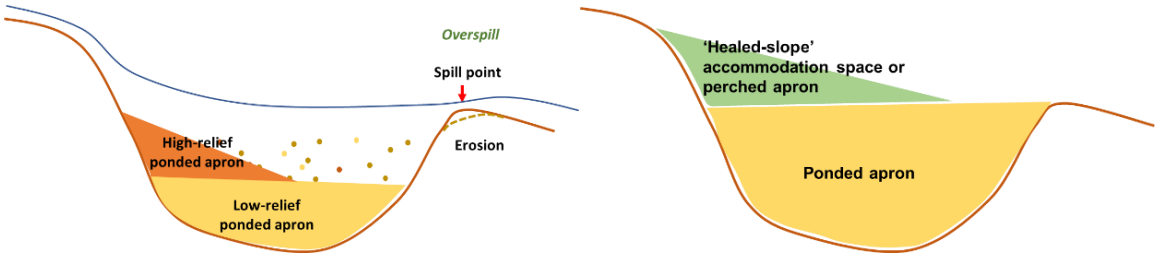

Figure 4.1: Evolution in time of the formation of the deposit inside the minibasin according with the 'fill-and-spill' model.

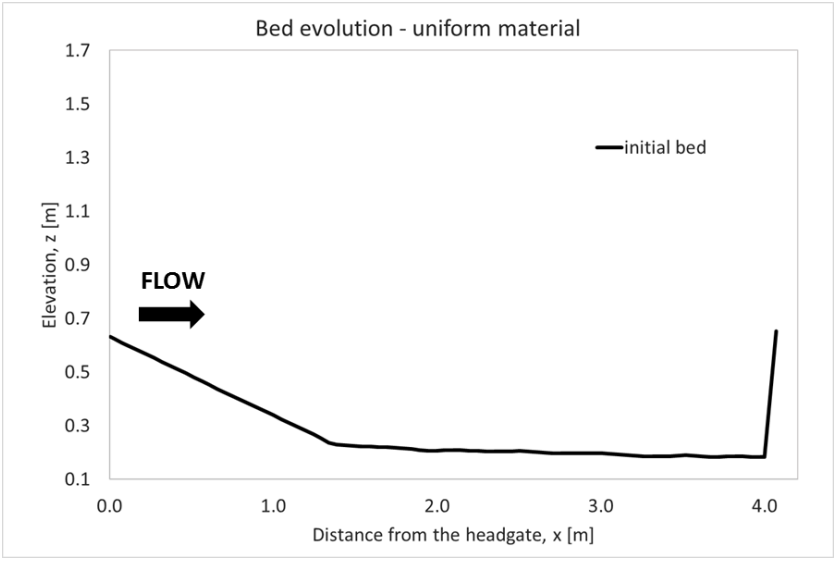

Figure 4.2: Initial bed profile used for the 2D laboratory scale simulations on minibasin

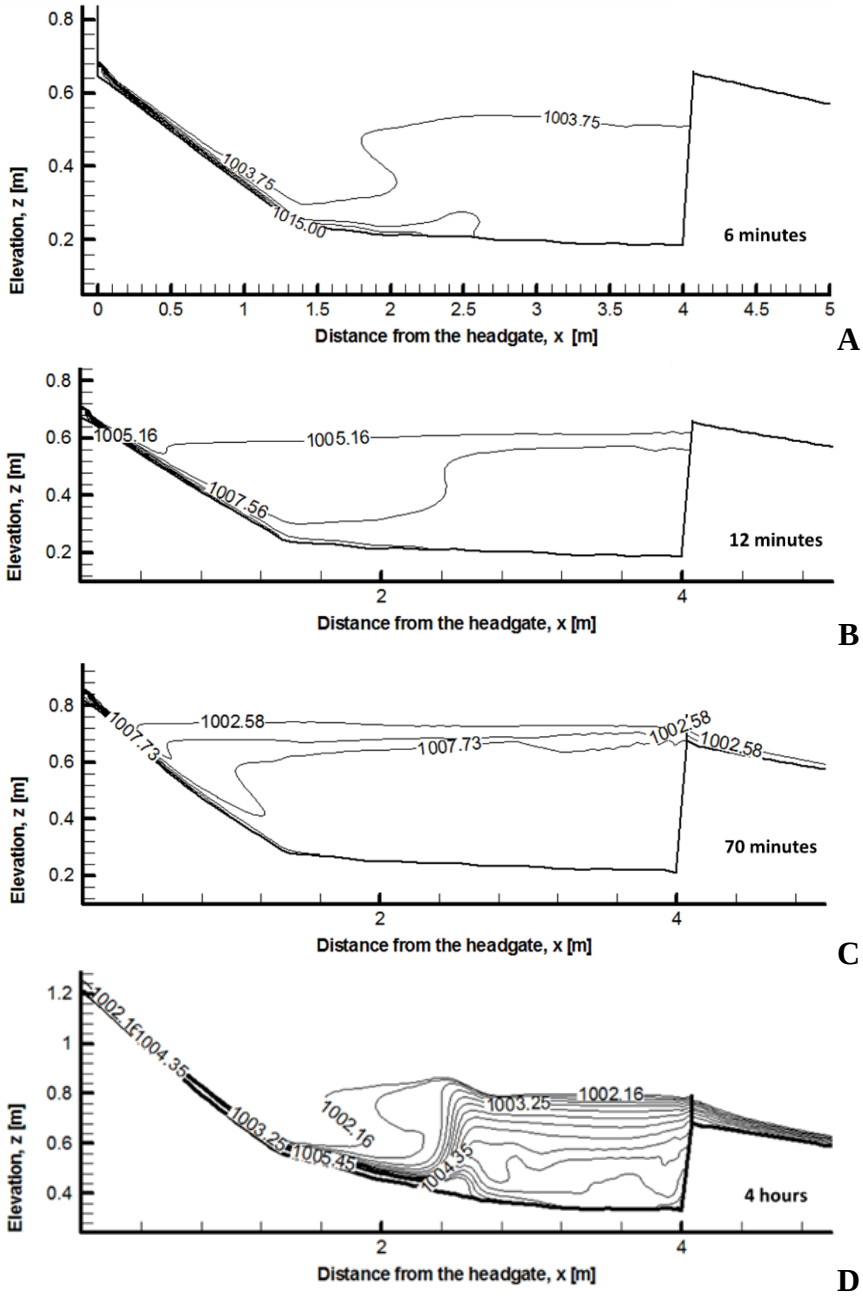

Figure 4.3: Density field of a turbidity current flowing through the basin (from left to right) at 6 min (A), 12 min (B), 72 min (C) and 4 hours (D). Contour legends are given in kg/m^3

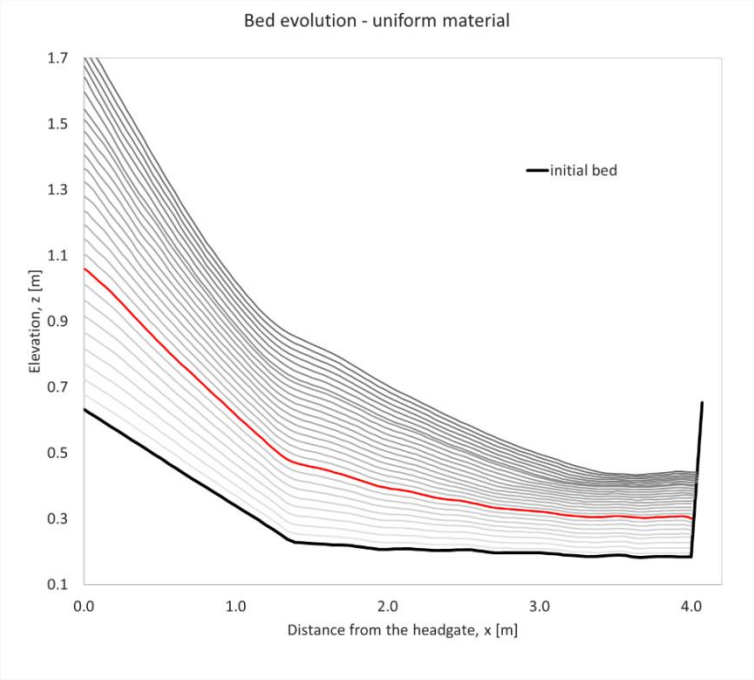

Figure 4.4: Bed elevation every 20 minutes (grey lines) until 5 hours of simulation at laboratory scale, using uniform material. The black line represents the initial bed and the red line represents the bed elevation at the time when the current starts to overspill

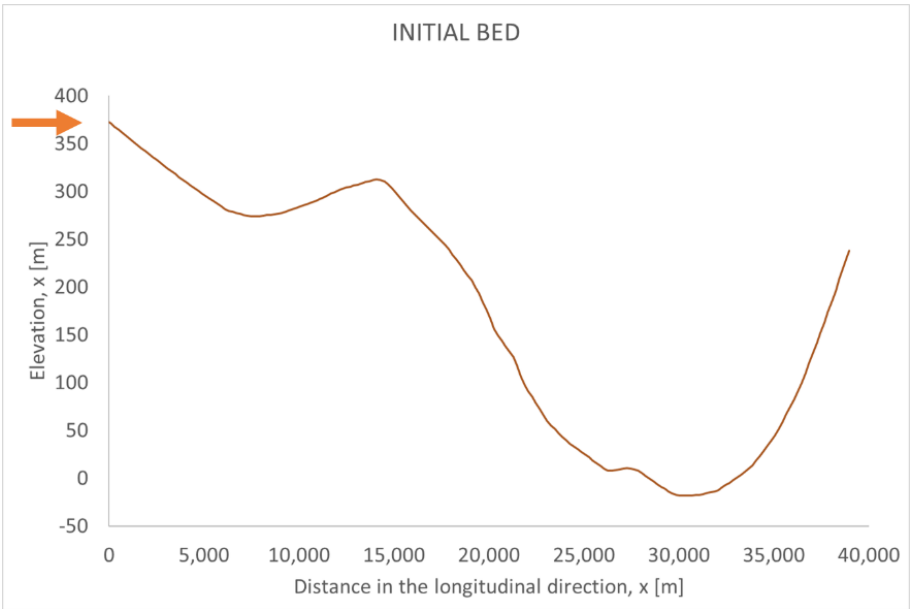

Figure 4.5: Initial bed profile of the two basins in series (Basin II and IV) used for the field scale applications, seismic series 10 from Prather et al. (2012).

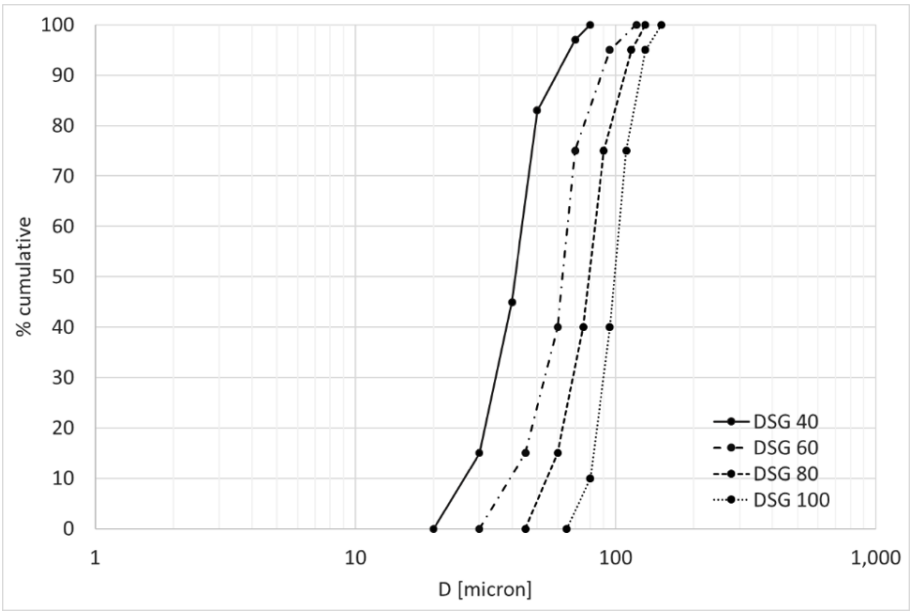

Figure 4.6: Grain size distribution of the sediment mixtures used for the 2D field scale simulations on minibasins

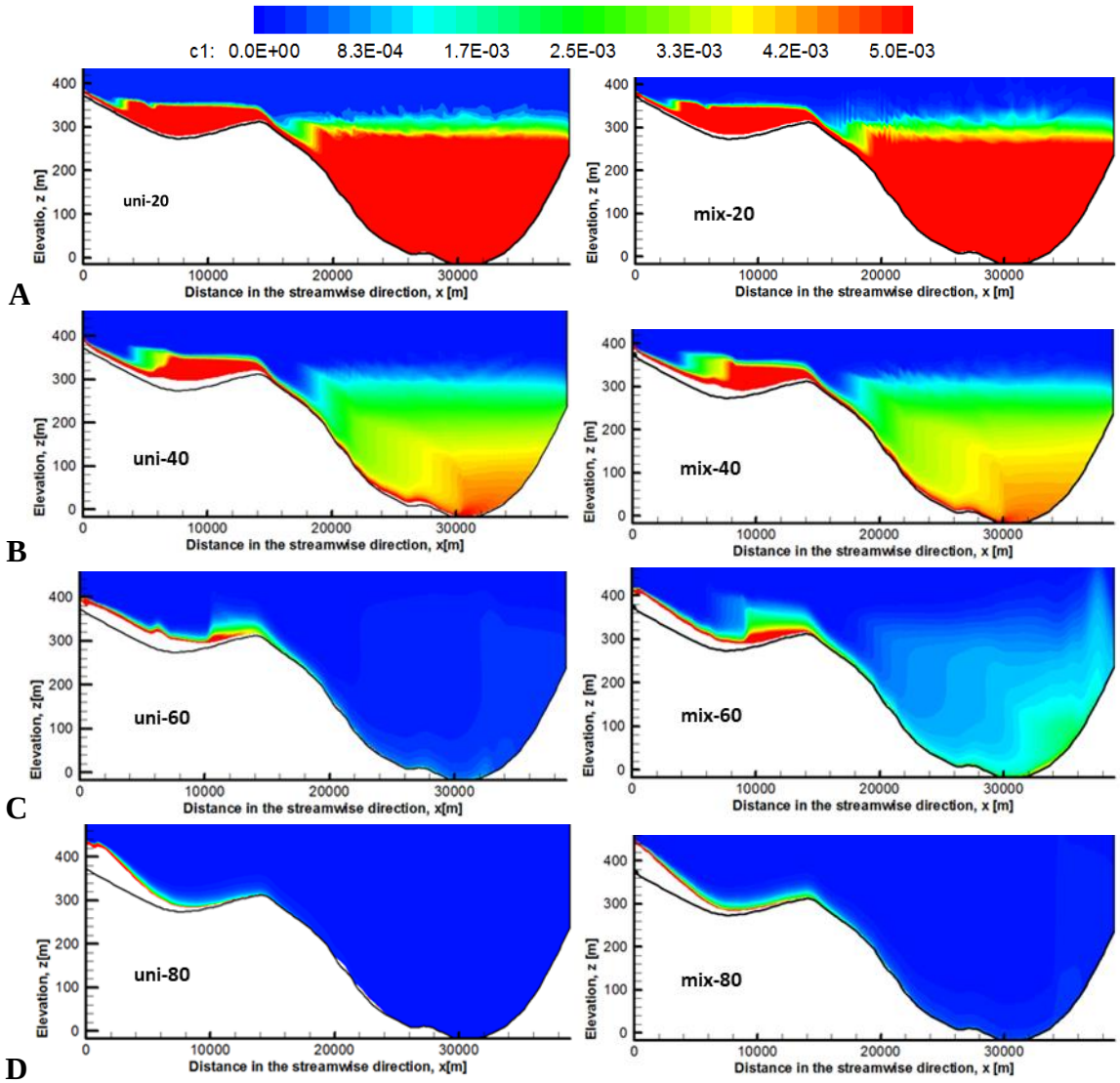

Figure 4.7: Total concentration profiles after two days of field scale simulations, turbidity current with different grain sizes, for the case of uniform material (left panel; uni20, uni40, uni60, uni80) and sediment mixture (mix20, mix40, mix60, mix80). The black line represents the initial bed.

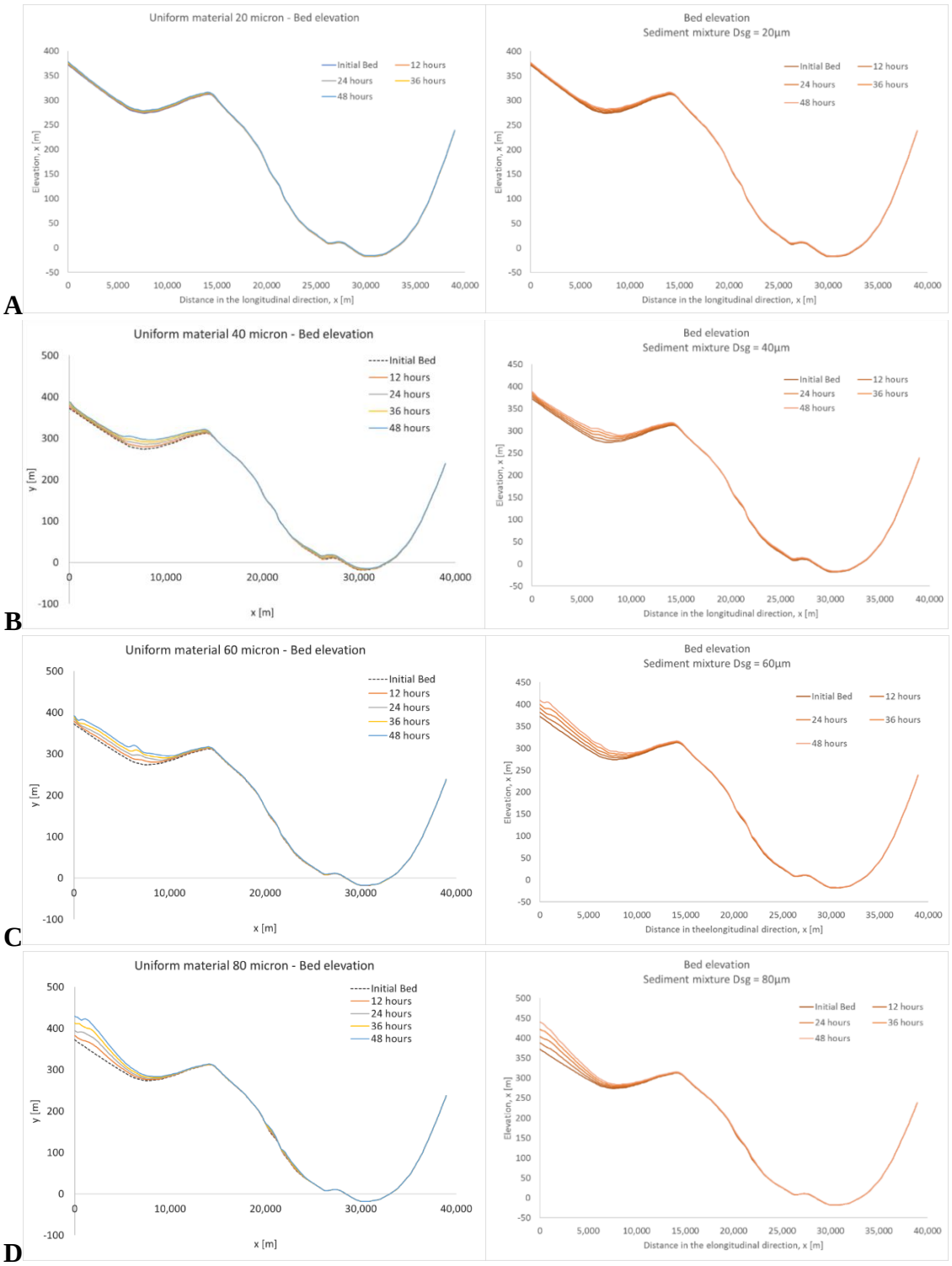

Figure 4.8: Bed evolution in time (every 12 hours) of field scale simulations of turbidity current with uniform material (uni20, uni40, uni60, uni80) on the left panel, and mixture on the right panel (mix20, mix40, mix60, mix80)

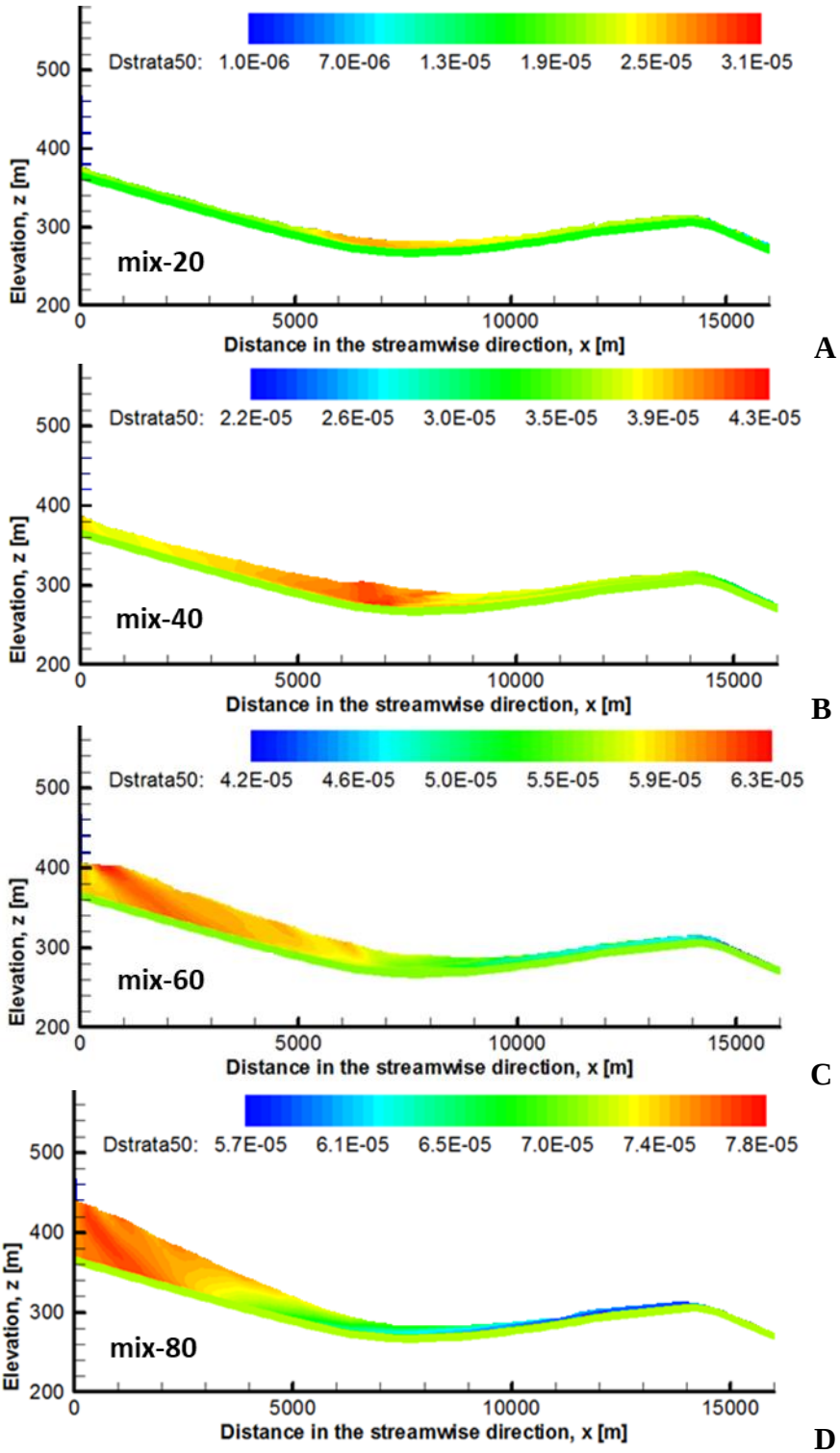

Figure 4.9: Median diameter (D_{50}) of the stratigraphy of the deposit in Basin II, after two days of simulated flow. Case of turbidity currents with sediment mixtures with different mean size diameter (mix20, mix40, mix60, mix80)

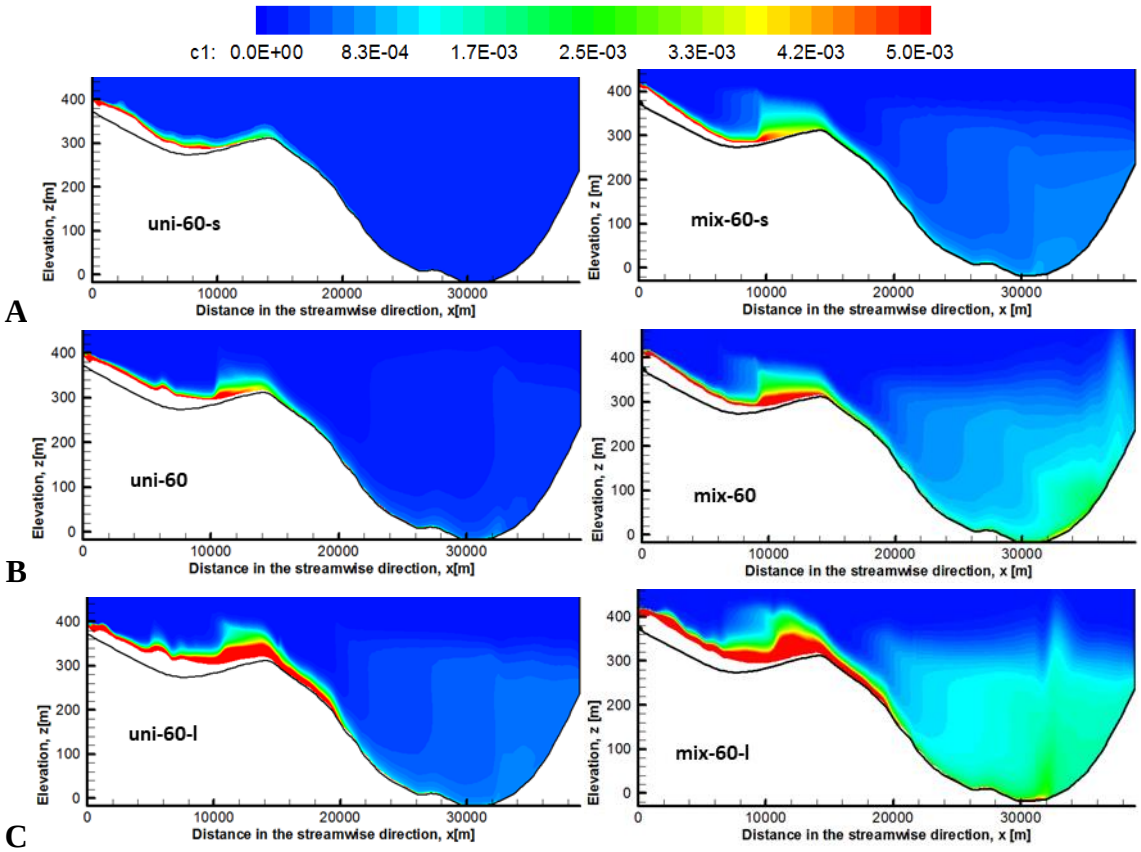

Figure 4.10: Total concentration profiles after two days of field scale simulations (uni60-s, uni60, uni60-l), with turbidity current with uniform material (60 μm) and different inflow velocities (u = 1.5, 2.0, 2.5 m/s) on the left panel. The case with mixtures (mix60-s, mix60, mix60-l) on the right pannel. The black line reppresent the initial bed.

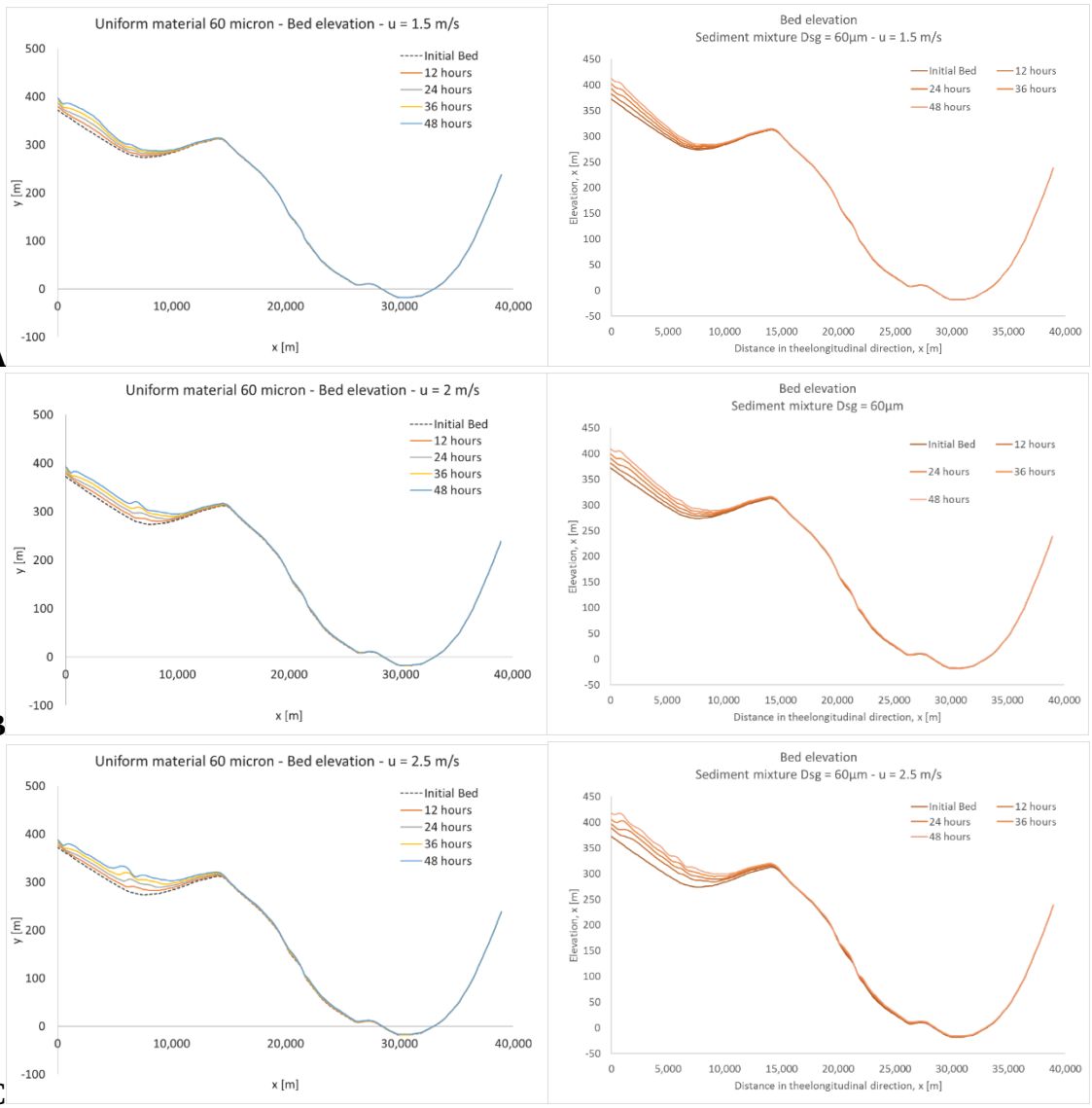

Figure 4.11: Bed evolution in time (every 12 hours) of field scale simulations, turbidity current with uniform material (60 µm) and different inflow velocities (uni60-s, uni60, uni60-l) on the left panel. The case of sediment mixture is reported in the right panel (mix60-s, mix60, mix60-l)

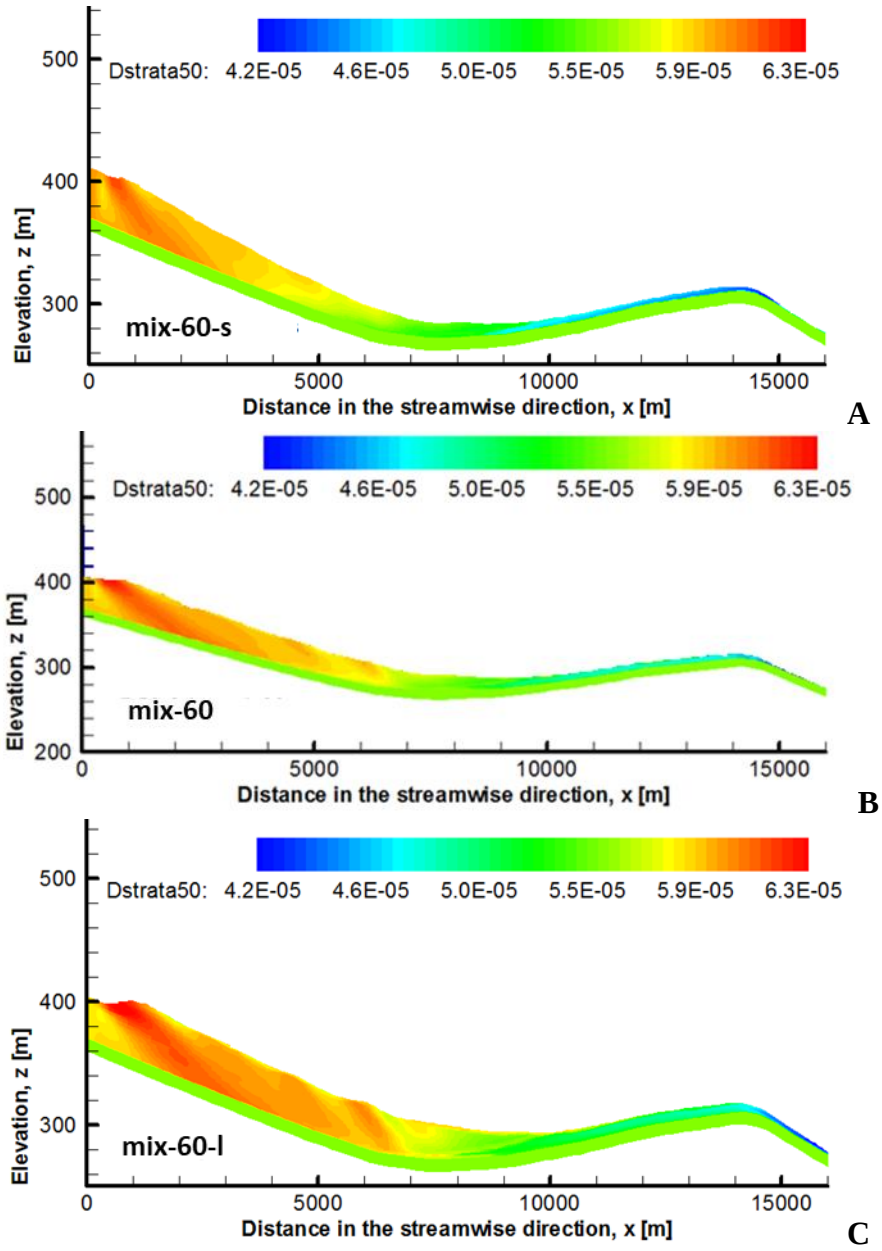

Figure 4.12: Median diameter (D_{50}) of the stratigraphy of the deposit of sediment mixture simulations with different current. Small, medium and large current (mix60-s, mix60, mix60-l) in Basin II.

CHAPTER 5

NUMERICAL INVESTIGATION OF DEPOSITION IN INTRASLOPE MINIBASINS

Intraslope salt- or shale-based basins or minibasins can be observed in both modern and ancient sedimentary settings, for example on the seafloor of the Gulf of Mexico (Pratson and Ryan, 1994; Badalini et al., 2000; Beaubouef and Friedmann, 2000), offshore of Trinidad and Tobago (Brami et al., 2000) and offshore Angola (Schollnberger and Vail, 1999). Minibasins were formed by the movement of layers of salt or mud in the subsurface (Violet et al. 2005), and they trapped thick layers of sediments transported by turbidity currents and other type of submarine flows, some of which contain excellent hydrocarbon reservoir properties (Toniolo, 2006).

Submarine minibasins are in general characterized by an elliptical or spherical shape with a steep inlet or proximal zone followed by an almost horizontal zone and an overflow zone near the distal end of the basin (Worrall and Snelson, 1989; Sumner et al., 1991; Pratson and Ryan, 1994), and they may or may not be connected by submarine canyons (Satterfield and Behrens, 1990; Winker, 1996; Beaubouef and Friedmann, 2000; Pirmez et al., 2000, Liu and Bryant 2000).

This chapter focuses on the simulation of the three-dimensional characteristics of the turbidity currents and their deposits in intraslope minibasins. The study is performed with the in-house built numerical model presented in Chapter 2. The model is applied at the field scale using the modern seafloor bathymetry of the Brazos-Trinity system in the Gulf of Mexico.

Sedimentation in intraslope minibasins has been studied with the collection and interpretation of field observations (i.e. Winker, 1996; Badalini et al., 2000; Beaubouef and Friedmann, 2000; Prather et al., 2000; Prather et al., 2012; Pirmez et al., 2012), the performance of laboratory experiments (i.e. Lamb et al., 2004 and 2006, Toniolo et al., 2006) and numerical modeling (Beaubouef et al., 2003a-b; Toniolo et al., 2006; Khan and Imran, 2008). This notwithstanding, questions regarding how the characteristics of the turbidity currents and of the deposit vary depending on the turbidity current magnitude, and on the grain size distribution of the transported sediment still need to be answered. The numerical simulations presented in this chapter were specifically designed to answer the above questions.

This chapter is organized as follows: first a brief description of the turbidity current characteristics relevant to this study is presented. The validated model (Chapter 2) is used to simulate turbidity currents on the present seafloor of the Gulf of Mexico in the area of the Brazos-Trinity system. The results of the field scale simulations are discussed, and the main finding are summarized.

5.1. TURBIDITY CURRENT MORPHODYNAMICS RELEVANT TO THIS STUDY

When a turbidity current reaches the distal flank of a minibasin, it is reflected, and an upstream migrating bore forms (Kneller et al., 1991; Edwards, 1993). Laboratory

experiments by Lamb et al. (2005), Toniolo et al. (2006) and Sequeiros et al. (2009, a b) with sustained currents in 2D configuration, i.e. no changes in the direction transverse to the main flow direction, demonstrated that after the current reflection the migrating bore travels upstream until it stabilizes, i.e. reaches a relatively stable position in space. This stable position slowly migrates downstream due to the deposition of sediment in the minibasin (Lamb et al. 2004, Toniolo et al., 2006 and 2007). Downstream of the stable bore position, the current is characterized by relatively small velocities with a sharp, clearly identifiable interface separating the turbidity current from the ambient water. Turbidity currents with these characteristics are called ponded currents and the portion of the basin occupied by a ponded turbidity current is called ponded area (Prather, 2000).

Experimental work performed in a 2D configuration with well sorted sediment showed that the vertical profiles of suspended sediment concentration in the ponded zone are relatively uniform, i.e. there is a small variation of concentration in the direction normal to the basin floor (i.e. Lamb et al., 2004, 2006).

A parameter commonly used to characterize the turbidity current is the densimetric Froude number (Sequeiros et al., 2009; Sequeiros 2010, Sequeiros 2010; Garcia, 1990, Parker et al. 1986) defined as:

$$Fr_d = \frac{U}{\sqrt{RgCh}}$$

where U, h and C are the depth-averaged velocity, flow thickness and suspended sediment concentration respectively, R is the submerged specific gravity of the sediment and g is the acceleration of gravity. When Fr_d is smaller than unity, the flow is called subcritical. Ponded turbidity currents have very small values of Fr_d.

5.2. 3D MODEL VALIDATION AT LABORATORY SCALE

The model was tested against the results of 3D experiments performed at the University of Illinois, Urbana-Champaign. The experimental setup is presented in Figure 5.1. Water and sediment were mixed in a head tank. The mixture was then released in a model canyon connected to two linked fiberglass minibasins. The model was located in a larger flume filled with tap water. Data collected in the first basin were used for model validation.

During the experiments, repeated sustained 20 minutes-long turbidity currents were released to study sedimentation in 3D intraslope minibasins in the case of non-uniform material. The experiments commenced with the release of a turbidity current in the empty fiberglass model and the successive currents were released on the previously emplaced deposit. High-resolution, laser-based bathymetry measurements were collected at the end of each release to characterize the depositional pattern.

Initial conditions

The laser-based bathymetry of the fiber-glass laboratory minibasin was used as initial condition for the first numerical simulation. The numerically generated bed from the flow was used as the initial condition for the following run. The information on five different runs considered for numerical modeling are presented in Table 5.1.

The grain size distributions of the sediment used in the experiments and in the model validation runs are shown in Figure 5.3. The geometric mean size of this material was 15 μm, the median grain size was 19 μm and the geometric standard deviation was 2.27.

In the model validation runs the following parameters were specified: submerged specific gravity of the sediment, $R = 1.60$; porosity of the deposit, $\lambda = 0.4$; and ambient

fluid density, $\rho = 1{,}000$. The computational domain of the basin consisted of 45 x 31 nodes, 56 nodes in the vertical direction and the near bed size of the cell was 1 mm.

Results

The comparison between the experimental results and the numerical simulations is presented in terms of bed elevation at the end of each run in Figure 5.4 where the color scale represents the deposit thickness in meters. The experimental results are reported in the left panels and the numerical simulations in the right panels. In run 1 and 2 preferential deposition occurs in the deepest area, at the center of the basin. A reasonably good agreement between numerical and experimental simulations can be observed especially at the end of the second run. The differences between numerical and experimental deposits on the proximal flank of the basin are partially due to details of the experimental setup that are not reproduced in the numerical model. Notwithstanding the differences in depositional pattern, the comparison between numerical and experimental data shows a reasonably good agreement.

The good agreement between model simulations and experiments is also shown in Figure 5.5, where the temporal evolution of the deposit in the strike direction at 2.87 m and 3.31 m from the basin entrance (location of siphon 1 and 3) is presented. At 2.87 m from the basin entrance the model is able to capture the formation of an asymmetric deposit with respect to the center of the cross section. A similar deposit asymmetry was observed in the experiments in runs 3-5. In the distal part of the basin, at a distance of 3.31 m from the basin entrance, the deposit in runs 3-5 was not as thick as in the proximal part of the basin and remained symmetric with respect to the center of the cross section.

Figure 5.6, Figure 5.7, and Figure 5.8 report the comparison of the vertical profiles of the total sediment concentration at the three siphon locations, highlighted in Figure 5.2 (1, 2, 3) (left panel). The concentration measured during the experiments is the dashed series, and the continuous line is the numerical simulated profile

The right panel of Figure 5.6, Figure 5.7, and Figure 5.8 present the comparison of the fraction (vertical axes) of each grain size (horizontal axes). Each series represents a location in the vertical direction (with z1, z2, z3 the locations in the vertical direction which are the same as those used for the comparison of the total vertical concentration). The series *z1-s* represents the sediments fractions of the turbidity current at the closest point to the bed computed numerically, while *z1-e* is the sediment fractions measured during the experiments. Moving in the vertical direction of the profile so that the point is located farther from the bed, increases the series number (z2-e and z2-s). In each of the three figures, the profiles at the end of every run are reported: the top panel represents Run 1, and the bottom panel represents Run 5. The simulations capture the trend of the vertical total concentration; a better agreement between experimental and simulated profiles is found in successive runs (Run 4 and Run 5).

5.3. APPLICATION OF THE MODEL AT FIELD SCALE - TURBIDITY CURRENTS IN SUBMARINE MINIBASINS IN THE GULF OF MEXICO

The minibasin system on the continental slope in the Gulf of Mexico is in the proximity of the shelf-slope break. It has an area approximately of 84 km in the lateral direction and 108 km in the longitudinal direction, characterized by the presence of four minibasins (Figure 5.9): Basin I is the basin closest to the shelf; a canyon connects this basin with Basin II and Basin III. Basin II and III are both connected by two different canyons to Basin IV.

The study area is a 25 km wide and 35 km long portion of the Brazos-Trinity system where Basins II, III, and IV are located. The canyon that connects Basin II to Basin IV is steeper than the canyon connecting Basin III to Basin IV. Basin IV is a large basin located in the distal part of the study area; it is bounded by steep flanks and it is only connected by canyons to Basin II and III. In other words, the modern seafloor of the Gulf of Mexico does not show any canyon connecting Basin IV to the rest of the continental slope in the downdip direction.

To perform the 3D simulations presented in this chapter the seafloor bathymetry has been smoothed to avoid numerical problems induced by grid skewness. In particular, the smoothing was done with MATLAB using the function interp2, which applies linear interpolation between points. The computational domain has been discretized with 229 x 93 nodes in the horizontal plane, 61 nodes in the vertical direction and with a near bed cell height of 0.5 m.

Description of the numerical runs

The modern seafloor bathymetry of the study area is presented in Figure 5.10 in terms of water depth, with blue colors denoting the deepest areas. Contour lines have been drawn every 20 m. The white dashed lines identify the locations of the stratigraphic sections described in the continuing of this chapter. The numerical simulations presented in the continuing of this chapter primary focus on the sedimentation in Basin IV.

Figure 5.10 clearly shows that turbidity currents can enter Basin IV from two canyons. Canyon I connecting Basin II to Basin IV, and Canyon II connecting Basin III to basin IV. To investigate how deposition in Basin IV changes with the turbidity current path, i.e. entrance from Canyon I or Canyon II, two different conditions were considered.

In one case, the turbidity current entered from Basin II (blue arrow in Figure 5.10). In the other case, the turbidity current entered from the canyon (red arrow in Figure 5.10) and reached Basin III. In the continuing of this chapter, the case of the turbidity current from Basin II is referred to as 'entrance from the basin' condition, and the case of the turbidity current entering Basin III from the canyon is referred as 'entrance from the canyon'.

The model upstream boundary condition was expressed in terms of flow velocity and suspended sediment concentration at the entrance cells either located in Basin II or in the canyon. In all the simulations the inlet velocity was set equal to 2.5 m/s and the volumetric suspended sediment concentration equal to 2%. The width of the entrance boundary condition for the flow was set constant, and different current heights were specified to vary the turbidity currents magnitudes (entrance velocity constant for all the simulations). The 'small' current occupied the lowermost ¼ of the inlet cross section (entrance from the basin: Q =15,000 m^3/s – entrance from the canyon: Q = 500 m^3/s.). The 'medium current' occupied the lowermost ½ cross section (entrance from the basin: Q = 30,000 m^3/s – entrance from the canyon: Q = 1,000 m^3/s.). The 'large current' occupied the entire height of the inlet cross section (entrance from the basin: Q = 60,000 m^3/s – entrance from the canyon: Q = 2,000 m^3/s.).

A schematic diagram of the different entrance conditions is presented in Figure 5.11. A close look at Figure 5.11 shows that the entrance cross section in Basin II was significantly wider and deeper than the cross section of the canyon entering Basin III and this resulted in larger turbidity currents in the simulations with entrance condition from Basin II than in the simulations with entrance condition from the canyon and Basin III.

To investigate the role of the sediment size distribution on the turbidity current flow and on the emplaced deposit, three simplified sediment size distributions were considered. These simplified distributions were made of the same volume fraction content (50%) of two grain sizes, one characterizing the fine sediment and equal to 20 μm and the other characterizing the coarse sediment fraction and equal to 80 μm, 100 μm or 130 μm.

An unimodal grain size distribution with five characteristic grain sizes with geometric mean diameter equal to 40 μm and median diameter (D_{50}) equal to 41.2 μm (Figure 5.12), close to the geometric mean size of the of the 20 μm – 100 μm simplified mixture, was considered to investigate the sensitivity of the model results to the specified sediment size distribution. The inlet concentration in these simulations was set equal to 5% and this resulted in higher sediment flow rates than the other simulations (inlet flow velocity used in this simulation was the same as the one used before, 2.5 m/s).

These conditions are summarized in Table 5.2 in terms of entrance conditions (entrance from the basin or from the canyon), flow rates (small-medium and large currents), sediment characteristics (sediment grain sizes and concentration). The duration of the simulated turbidity current was two days.

Results

This session is organized as follow. First results showing the time evolution of the large currents entering the study area from the basin and from the canyon are discussed in detail. Then, the effects of the sediment size distribution on the flow and deposit pattern are presented.

Effect of the entrance condition

The spatial changes in current velocity at 2.5 m from the basin floor is presented in Figure 5.13, where the color scale represents the velocity magnitude and the contour lines are the initial bathymetry. The top panels present the current velocity after 8 hours (left) and 16 hours (right), for the case of a large turbidity current entering from the basin. The current velocity after 8 hours (left) and 16 hours (right) for the large current entering from the canyon are shown in the two bottom panels.

The panels of Figure 5.13 show that, notwithstanding the entrance condition, in the case of a large turbidity current Canyon I and Canyon II are both active and the turbidity currents enter Basin IV from two different locations. In the case of the large current entering from the basin (top panels), the current reaches the downstream flank of Basin IV and is reflected in the first 8 hours of simulated time. Two zones of negative velocity, which are the result of the current reflection on the downstream flank, are clearly visible in the top right panel of Figure 5.13. Velocities up to 5 m/s characterize the flow in Canyon I, while the velocity magnitude in Canyon II is somewhat smaller suggesting that the turbidity current in Canyon I is larger than the turbidity current in Canyon II. After 16 hours of simulated time, the zones of negative velocity are still clearly visible in Basin IV (left top panel of Figure 5.13) but the velocity magnitude in the canyons is smaller than after 8 hours of simulated time. This suggests that after 16 hours of simulated time the current reflection on the downstream flank of Basin IV is playing a significant control on the flow characteristics in the canyons.

In the case of large turbidity current entering from the canyon (bottom panels) after 8 hours of simulated time the current has not yet reached the downstream flank and velocity

higher than 2 m/s are predicted in Canyon I and Canyon II. After 16 hours of simulated time a zone of negative velocities associated with the current reflection on the downstream flank is clearly visible in the distal part of Basin IV. A comparison between the areas of negative velocity of Figure 5.6 suggests that the magnitude and the entrance condition of the turbidity current play a significant control on the characteristics of the current reflection. It is thus reasonable to expect that these differences in the flow reflection will affect sedimentation patterns in Basin IV.

The comparison of the densimetric Froude number for the cases of large turbidity currents entering from the minibasin (top) and from the canyon (bottom) after two days i.e. at the end of the simulations, is reported in Figure 5.14 where the color scale represents the magnitude of Fr_d and the contour lines are the initial bathymetry.

Densimetric Froude numbers close or greater than one were observed in Canyon I (the canyon connecting Basin II with Basin IV) and in the upstream part of Canyon II (the canyon connecting Basin III with Basin IV) with largest values of F_{rd} occurring in canyon I. The densimetric Froude number in Basin IV is smaller than 0.4 suggesting the formation of a ponded turbidity current and the presence of the transition from a relatively fast to a ponded current occurring in Canyon II and at the exit of Canyon I, when the flow becomes laterally unconfined.

The evolution of the deposit thickness for a large current entering from Basin II is presented in Figure 5.15 where the color scale represents the deposit thickness and the contour line the initial bathymetry. The panels of Figure 5.15 (from the top to the bottom) show the deposit thickness after 8, 16, 24 and 48 hours of simulated time. In the first day simulated time (8, 16 and 24 hours) the turbidity current preferentially deposits in Basin II

and in the central part of Basin IV at the exit of Canyon I. Limited deposition is observed at the exit of Canyon II confirming that the turbidity current in Canyon I was significantly larger than the current in Canyon II, as suggested by the velocity distribution of Figure 5.13. Erosional areas are predicted in and around the canyons.

After two days of simulated time (fourth panel of Figure 5.15) the highest deposit thickness occurs in Basin II, in the central and deepest part of Basin IV, and on the proximal flank of Basin IV. Minor deposition can also be observed in Basin III confirming that a relatively small turbidity current spilled from Basin II into Basin III. Finally, significant erosion was observed in the neighboring areas of the canyons.

The thickness of the deposit emplaced by the large current entering from the canyon after 8, 16, 24 and 48 hours of simulated time is presented in the panels of Figure 5.16 (8 hours at the top and 48 hours at the bottom), where the color map represents the deposit thickness, and the contour lines characterize the initial bathymetry.

After 8 hours of simulated time (top panel of Figure 5.16), i.e. prior to the current reflection on the distal basin flank (Figure 5.13), the deposit in Basin IV is located at the exit of the two canyons on the proximal flank of the basin. After 16 and 24 hours of simulated time (second and third panels of Figure 5.16), i.e. after the current reflection, preferential deposition is still observed on the proximal flank of Basin IV. Erosional areas are predicted around the connecting canyons. After two days of simulated time (panel 4 of Figure 5.16) the highest deposition is still observed at the exit of the canyons, but significant deposition also occurred in the central and deep part of the basin.

In summary, in the case of a relatively large turbidity current entering Basin IV (entrance from the basin) the maximum thickness of the deposit is observed in the central

and deep part of Basin IV. When the turbidity current magnitude decreases (entrance from the canyon), the maximum deposit thickness is observed at the exit of Canyon I and Canyon II, i.e. on the proximal flank of Basin IV. This result suggests that the magnitude of the turbidity current relevant to the basin size controls the depositional pattern in submarine minibasins and should be accounted for in the interpretation of field data.

Effect of the sediment size distribution on the deposit

The influence of the sediment size distribution on the characteristics of the emplaced deposit have been investigated by comparing the deposit thickness and the fraction of the coarse grain of the bed surface sediment after two days of simulated time, for the case of medium current with simplified sediment distributions with characteristic grainsizes equal to 20 μm and 80 μm; 20 μm and 100 μm; and 20 μm and 130 μm.

The results are presented in Figure 5.17 in terms of deposit thickness at the end of the numerical simulations for medium current with the entrance condition from the basin. The color map of Figure 5.17 is the deposit thickness and the contour lines represent the initial bathymetry. The top panel of Figure 5.17 represents the deposit thickness for a turbidity current transporting relatively fine sediment (20 μm – 80 μm), the middle panel of Figure 5.17 pertains of the case of turbidity current transporting sediment with characteristic grain sizes of 20 μm for the fine material and 100 μm for the coarse material. The bottom panel of Figure 5.17 refers to the case of a turbidity current transporting relatively coarse material (20 μm – 130 μm).

The comparison between the three panels of Figure 5.17 shows that i) preferential deposition of sediment occurred at the canyon exits and in the central and deep part of basin IV; ii) as the size of the coarse sediment of the simplified mixture increased from 80 μm to

130 μm, the Basin IV deposits became thicker and wider; and iii) the maximum erosion of the areas surrounding Canyon I were observed in the run with the coarsest sediment size. It is important to note here that a significant portion of the Basin IV deposits in the runs with coarse sediment sizes equal to 100 μm and 130 μm might be associated with the erosion of Canyon I and Canyon II.

Deposit thickness maps at the end of the simulations for the case of medium turbidity currents entering from the canyon are presented in Figure 5.18, where the top panel refers to the case of simplified grain size distribution with characteristic grain sizes equal to 20 μm and 80 μm. The results of the central panel pertain to the simulations with a simplified sediment size distribution and coarse grain size equal to 100 μm. The results of the simulation with an idealized sediment size distribution and coarse grain size equal to 130 μm are in the bottom panel of Figure 5.18.

Noting that the magnitude of the medium turbidity entering from the canyon is smaller than the magnitude of the current entering from the basin, the depositional pattern is significantly different than that presented in Figure 5.17 (entrance condition from the basin). In the case of a relatively small turbidity current (Figure 5.18) preferential deposition occurs on the proximal flank of Basin IV at the exit of the canyons.

The spatial distribution of the coarse sediment fraction at the end of the simulations is presented in Figure 5.19 and Figure 5.20, where the color maps represents the volume fraction content of coarse sediment and the contour lines are the initial bathymetry. The results in Figure 5.19 pertain to the simulations with entrance condition from the basin, and the result in Figure 5.20 refer to the simulations with entrance condition from the canyon. The results of the simplified sediment mixture 20 μm - 80 μm, 20 μm - 100 μm, and 20 μm

- 130 μm are in the top, middle and bottom panels of Figure 5.19 and Figure 5.20 respectively.

Figure 5.19 shows that in the case of a turbidity current entering from the basin the grain size distribution of the bed surface sediment in the areas characterized by erosion is equal to the grain size distribution of the parent material. In the areas characterized by deposition, the surface sediment is coarsest where the deposit is thickest. It is interesting to note here that the largest spatial variability of the coarsest sediment size is observed in the run with the coarsest grain size equal 80 μm, i.e. when the difference between the two characteristic grain sizes is smallest and the deposit thickness is relatively small.

In the case of a medium turbidity current entering from the canyon (Figure 5.20), which is smaller than the turbidity current of Figure 5.19, coarse bed surface sediment is still deposited where the deposit is thickest, i.e. on the proximal flank of the basin at the canyon exits, but the spatial variability of the volume fraction content of coarse sediment in Basin IV is larger than in Figure 5.19.

Effect of the current intensity on the deposit

The effect of the current intensity (small – medium – large) on the deposit thickness and the grain size distribution of the bed surface sediment is investigated for the case of a simplified sediment size distribution and characteristic grain sizes equal to 20 μm and 100 μm, and duration of two days of simulated time.

Figure 5.21 shows the deposit thickness for the case of turbidity currents entering from the basin, with bimodal gran size distribution characterized by small diameter of 20 μm and coarse diameter of 80 μm. The color map denotes the deposit thickness and the contour lines represent the initial bathymetry. The top, middle and bottom panels of Figure

5.21 respectively show the results of the simulations with small, medium and large turbidity currents. The comparison between the panels of Figure 5.21 reveals that the deposit thickness increases with the current intensity, but the main features of the depositional pattern do not change. The deposit is located on the proximal flank of the basin at the canyon exits and in the central and deep part of the basin. In the case of the large current, which overspills to Basin III significant deposition is also observed in Basin III.

The deposit thickness for the case of a turbidity current entering from the canyon is presented in Figure 5.22. Due to the small current intensity compared to the case of Figure 5.21, the deposits in Basin IV present similar characteristics, i.e. preferential sediment deposition occurred on the proximal basin flank at the canyon exits. A close look at Figure 5.15 reveals a slight increase in deposit thickness with increasing turbidity current intensity.

The comparison of the volume fraction content of surface sediment with characteristic diameter equal to 100 μm at the end of the numerical runs is presented in Figure 5.23 and Figure 5.24, for the cases of current entering from the basin or from the canyon respectively. The color scale represents the volume fraction content of coarse sediment in the bed surface and the contour lines the initial bathymetry. The top, central and bottom panels of Figure 5.23 and Figure 5.24 respectively refer to the cases of small, medium and large turbidity currents.

Figure 5.23 and Figure 5.24 show the presence of coarse bed surface sediment in the area characterized by net deposition. As previously observed in Figure 5.19 and Figure 5.20, a larger variability of coarse surface sediment fraction is observed in the case of relatively small currents suggesting that the characteristics of the flow may significantly change based on the turbidity current magnitude relative to the basin size.

The spatial distribution of grain sizes in the deposit created by a large current entering from the basin (grain size distribution of the current: 20-100 μm) at the three cross sections indicated in Figure 5.10, Figure 5.21 and Figure 5.23 (bottom panels) is presented in Figure 5.25, where the color scale represents the volume fraction content of coarse sediment (D = 100 μm). The top, central and bottom panels of Figure 5.25 respectively refer to the strike sections respectively located at 20 km, 23 km and 27 km from the proximal boundary of the computational domain (Figure 5.21 and Figure 5.23, bottom panels), i.e. where the numerical turbidity currents are released. The cross sections of Figure 5.25 show that the final deposit has a tabular shape, it is thickest in the deepest areas of the basin and is entirely composed of coarse material.

Effect of the turbidity current sediment size distribution

To investigate how the number of sediment sizes used to describe the sediment size distribution may affect the numerical results in terms of 1) deposit thickness, 2) surface sediment characteristics, and 3) spatial distribution of the sediment sizes in the deposit, a simulation with a small and a large turbidity current carrying a sediment size distribution with 5 characteristic grain sizes was performed. The inlet volumetric suspended sediment concentration was equal to 5%.

The deposit thickness, and spatial distribution of surface sediment sizes and sediment sizes in the deposit of the run with 5 characteristic grain sizes is presented in Figure 5.26 - Figure 5.29, for the case of a large and a small turbidity currents entering from the basin respectively.

The deposit thickness at the end of the simulations are presented in Figure 5.26 in which the results pertaining to the simulation with the small current are in panel (a) and

those pertaining to the simulation with the large current are in panel (b). The deposits of Figure 5.19 present the same characteristics of the deposits emplaced in the simulations with the simplified sediment mixture. In the case of a small current, preferential deposition occurs on the proximal basin flank at the canyon exits. In the simulation with a large current, preferential deposition occurs in the central and deep part of the basin. A close look at Figure 5.26a reveals that the deposit in the simulations with 5 characteristic grain sizes is not as thick and localized as in the case of the simplified grain size distribution of Figure 5.21.

The spatial distribution of the median grain size (D_{50}) of the surface sediment at the end of the simulations is presented in Figure 5.20, with the results for the simulation with a small current in panel (a) and the results of the large current simulation in panel (b). The color scale represents the median grain size, the black arrow indicate the median grain size of the sediment mixture used in the simulation (40.2 μm) and the contour lines are the initial bathymetry. The comparison between Figure 5.27 and the spatial distributions of bed surface sediment in the case of the simplified sediment mixtures considered above (Figure 5.23, top and bottom panels) reveals that when more characteristic grain sizes are used to describe the sediment size distribution the difference in grain size between erosional and depositional areas is not as strong as in the case of two characteristic grain sizes. Notwithstanding the number of grain sizes used in the simulations, coarse material is deposited on the bed surface where the deposit is thickest, and finest material is deposited in the distal part of Basin IV. Interestingly, the bed surface sediment in the distal part of Basin IV is coarsest at the end of the simulation with the large turbidity current.

The spatial distribution of grain sizes in the three strike sections of Basin IV indicated in Figure 5.10 is presented in Figure 5.28, for the case of the large turbidity current of Figures Figure 5.26b and Figure 5.27b. The color map of Figure 5.28 represents the sediment median diameter (D_{50}). The most upstream cross section located at 20 km from the proximal boundary of the computational domain is the top panel, the cross sections at 23 km and 27 km from the proximal boundary of the domain respectively are in the middle and in the bottom panels of Figure 5.28. The comparison between Figure 5.25 and Figure 5.28 clearly shows that the number of characteristic grain sizes and the inlet concentration play a significant control on the shape of the deposit. The deposit at the end of the 2 day-long simulation with 5 characteristic grain sizes and inlet volumetric concentration of 5% (Figure 5.28) is not tabular. The deposit is localized at the canyon exit (top panel Figure 5.28) in the proximal part of the basin, and it is characterized by a relatively uniform thickness in the other two cross sections. Further, the sediment deposited close to the exit of Canyon II is coarser than the sediment deposited close to the exit of Canyon I showing a spatial distribution of grain sizes that was not captured in the simulation with a simplified sediment size distribution. The preferential deposition of coarse sediment at the exit of Canyon I is also visible in the plots of the volume fraction content of surface sediment with characteristic grain size equal to 34.6 μm and 60 μm respectively presented with color scales in the top and bottom panels of Figure 5.30. A small fraction of fine sediment was found on the surface of the deposit in the areas characterized by high deposition, while the fraction of coarse surface sediment on the thick deposit was larger than the fraction in the original sediment mixture.

The spatial distribution of fine (D = 34.6 μm) and coarse (D = 60 μm) surface sediment at the end of the simulation with 5 characteristic grain sizes and a small turbidity current is presented in Figure 5.30, where the color scale represents the volume fraction content of surface sediment with fine and coarse grain size. As in the case of a large turbidity current, the coarse surface sediment was found where the deposit was thickets and the fine sediment was on the surface of the basin floor in the distal area. In this run the coarse surface sediment was found close to the exit of Canyon I and not of Canyon II confirming that the magnitude of the turbidity current relative to the basin size might have played a very important role in the definition of the shape and the grain size characteristics of the deposit.

5.4. SUMMARY

This study was specifically designed to investigate the effects of turbidity current magnitude relative to the basin size and sediment size distribution on the sedimentation in an intraslope minibasin, i.e. Basin IV of the Brazos-Trinity system on the continental slope of the Gulf of Mexico.

The 3D numerical model with deforming bottom boundary and with a subroutine able to store the stratigraphy of the deposit presented in Chapter 2 was used in to perform the simulations. The field scale simulations confirm that the model is able to reasonably reproduce current characteristics and deposit geometries in linked submarine minibasins. In particular, the model reproduces the current reflection on the distal flank of the minibasin and the consequent formation of a ponded current. The main results of the simulations are summarized as follows:

- The deposit emplaced by relatively large currents are thickest in the central portion of the basin with a sedimentation pattern that resembles what Prather et al. (2012) call *low-relief ponded apron*;
- The deposits emplaced by relatively small currents are thickest on the proximal flank of the basin, resembling what Prather et al. (2012) called *high-relief ponded apron*;
- The simulations with sediment size distributions specified in terms of 2 characteristic grain sizes show preferential deposition of coarse material in the areas in which the deposit is thickest;
- The simulations with a grain size distribution specified in terms of 5 characteristic grain sizes show preferential deposition of coarse sediment where the deposit it thickest and in correspondence of the canyon exits;
- The comparison between strike sections of deposits obtained in simulations with 2 and 5 grain sizes shows that the deposit in the simulations with 2 grain sizes tends to be thickest where the basin is deepest. On the contrary, in the simulations with 5 grain sizes the shape of the deposit tends to follow the shape of the minibasin floor. Further investigation on the causes of the different sedimentation patterns in the simulations with 2 and 5 characteristic grain sizes is necessary.

Table 5.1: 3D model validation - Experimental conditions

Q = 0.30 l/s		
Run	**Duration [min]**	**Initial concentration [%]**
1	20	2.34
2	20	4.36
3	20	4.89
4	20	5.75
5	20	5.56

Table 5.2: Characteristics of the numerical runs. The runs are indicated with asterisk refer to the simulations with the unimodal sediment mixture.

Entrance from the basin						
	Small	**Medium**			**Large**	
	20-100	**20-80**	**20-100**	**20-130**	**20-100**	**D_g40 ***
Flow velocity [m/s]	2.5	2.5	2.5	2.5	2.5	2.5
Flow depth [m]	1.5	3.0	3.0	3.0	6.0	6.0
Discharge [m3/s]	15,000	30,000	30,000	30,000	100,000	100,000
Sediment characteristics	20 µm - 100 µm	20 µm - 80 µm	20 µm - 100 µm	20 µm - 130 µm	20 µm -100 µm	D_g = 40 µm
Sediment total concentration	2%	2%	2%	2%	2%	5%
Entrance from the canyon						
	Small	**Medium**			**Large**	
	20-100	**20-80**	**20-100**	**20-130**	**20-100**	**D_g40 ***
Flow velocity [m/s]	2.5	2.5	2.5	2.5	2.5	2.5
Flow depth [m]	1.0	2.0	2.0	2.0	4.0	4.0
Discharge [m3/s]	500	1,000	1,000	1,000	2,000	2,000
Sediment characteristics	20 µm - 100 µm	20 µm - 80 µm	20 µm - 100 µm	20 µm - 130 µm	20 µm - 100 µm	D_g = 40 µm
Sediment total concentration	2%	2%	2%	2%	2%	5%

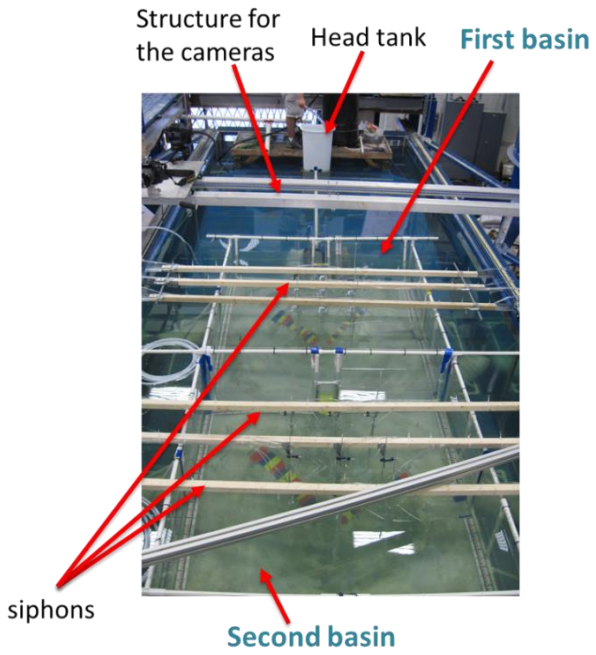

Figure 5.1: Three-dimensional experimental setup of minibasins (University of Illinois, Urbana-Champaign, courtesy Enrica Viparelli)

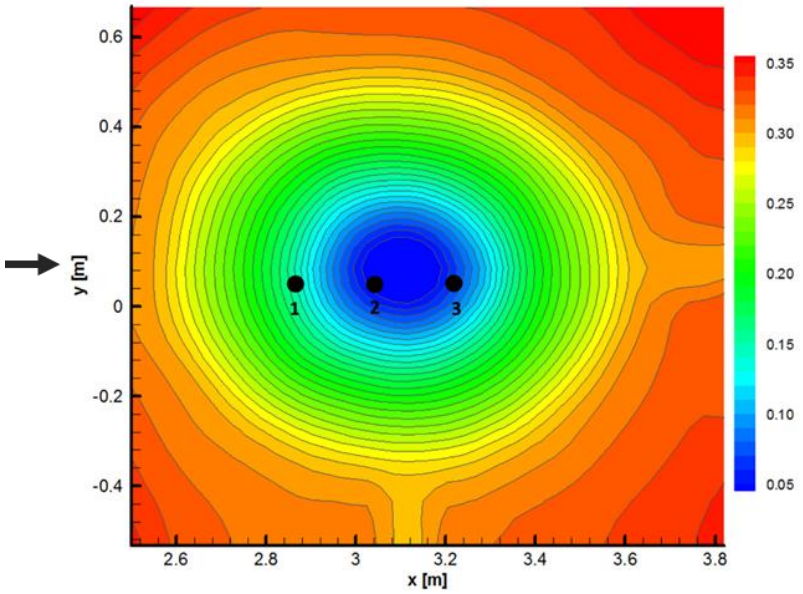

Figure 5.2: Initial bed for the 3D model validation at laboratory scale (courtesy Shell Exploration)

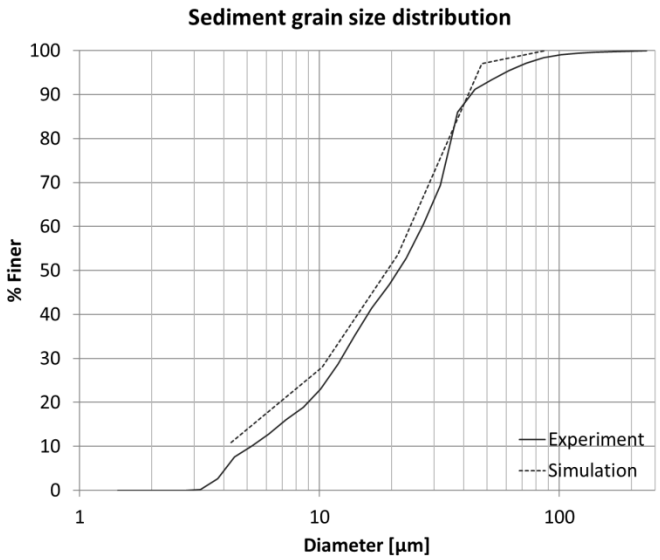

Figure 5.3: Sediment grain size distributions used for the experiments and the numerical simulations (courtesy Shell Exploration)

Experiment Simulation

RUN 1

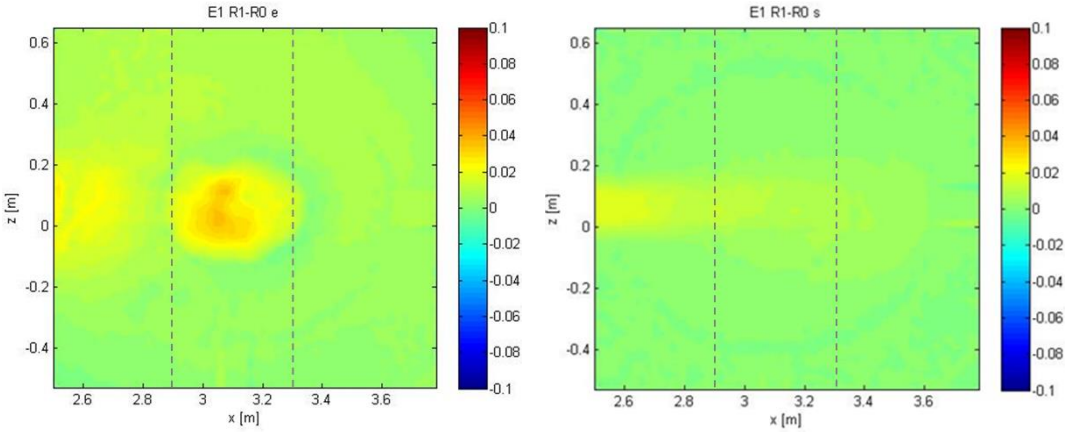

RUN 2

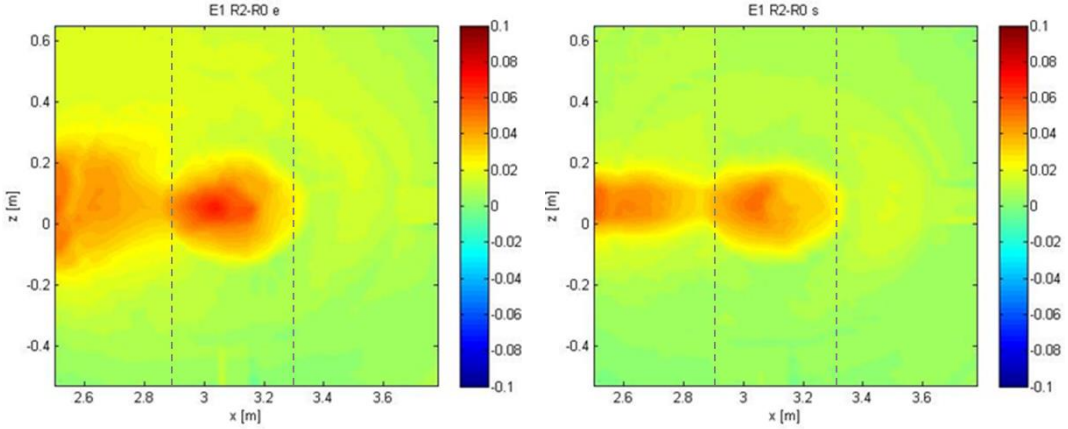

RUN 3

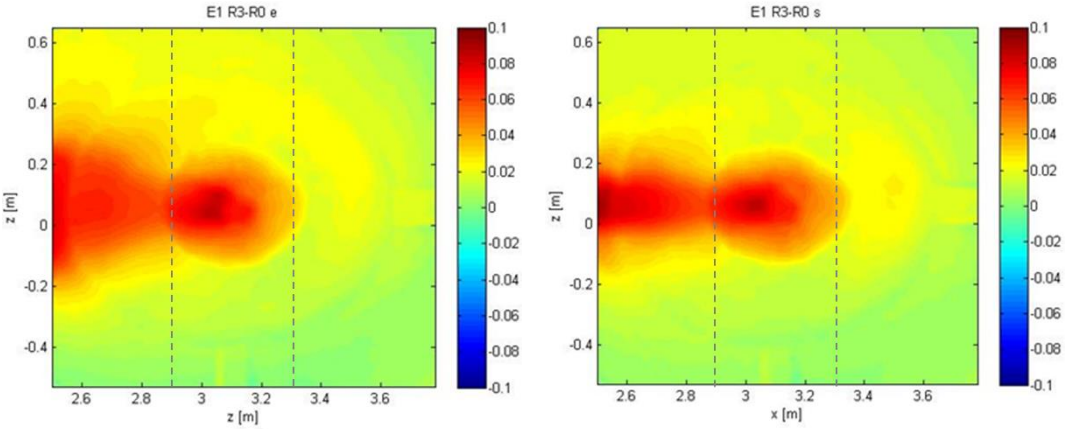

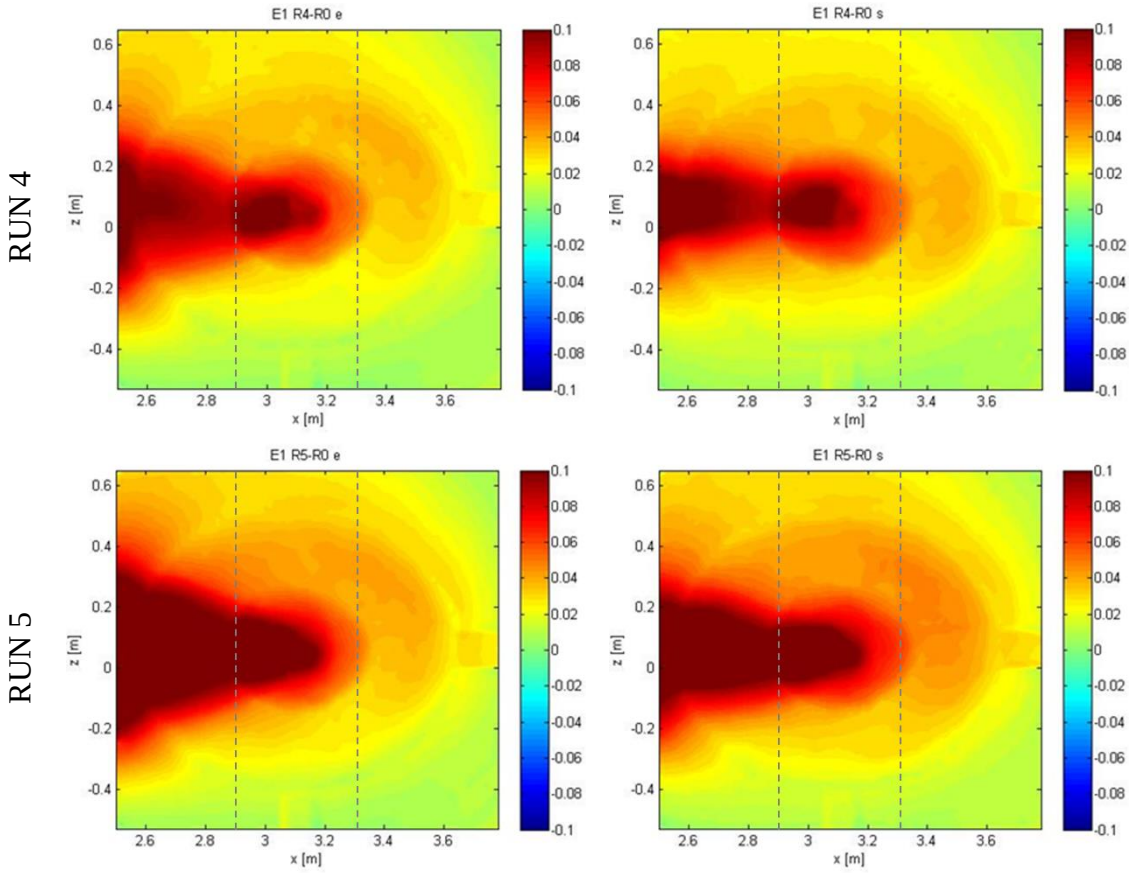

Figure 5.4: Comparison of the shape of the bed deposit at the end of each run between laboratory data (left panel) and simulations (right panel). The dashed lines are located at x = 2.87 m and 3.31 m. (courtesy Shell Exploration)

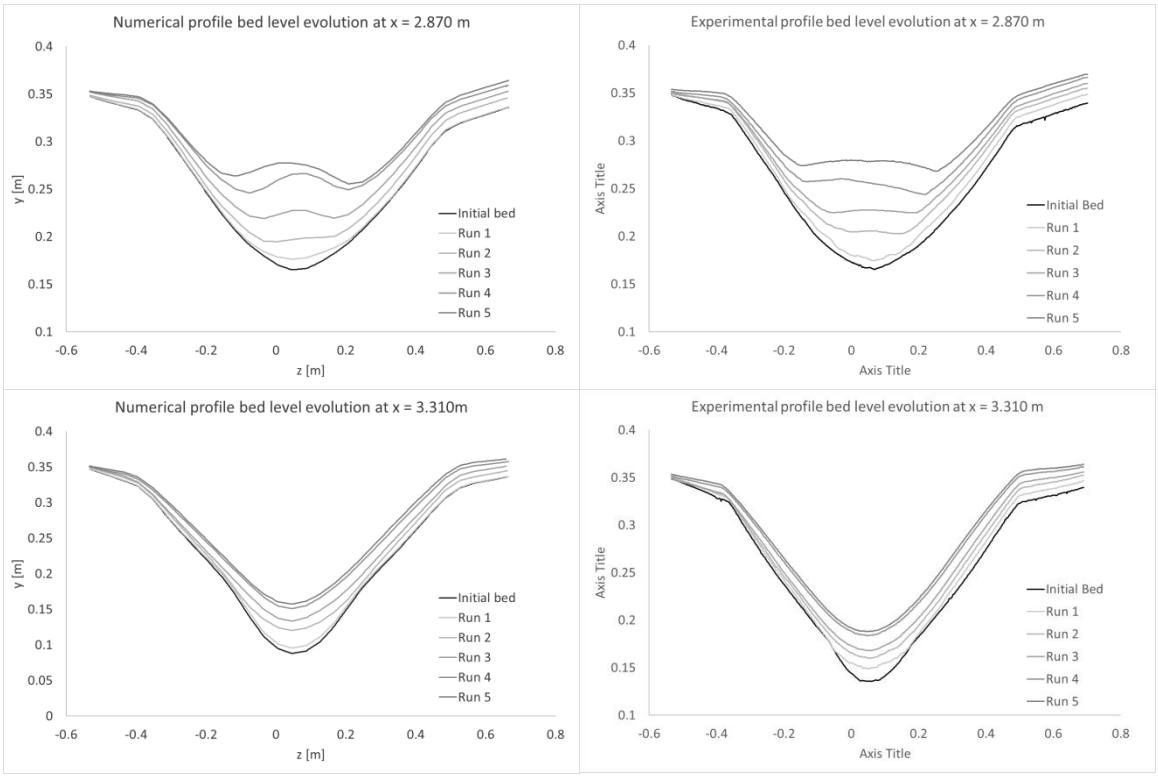

Figure 5.5: Bed elevation profiles after two cross sections located at x = 2.87 m and x = 3.31 m, respectively upstream and downstream of the deepest point of the basin. Bed elevation is shown at the end of each run.

Total Concentration

Sediment Fraction

Run 1

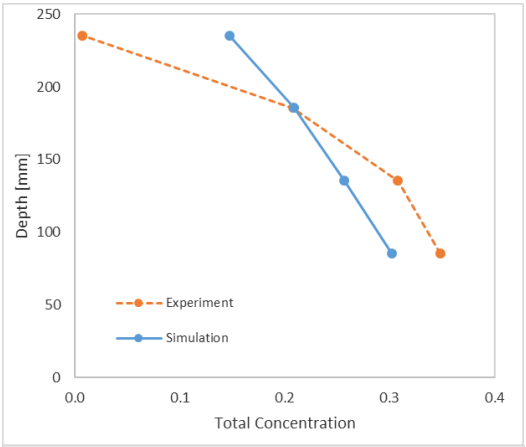

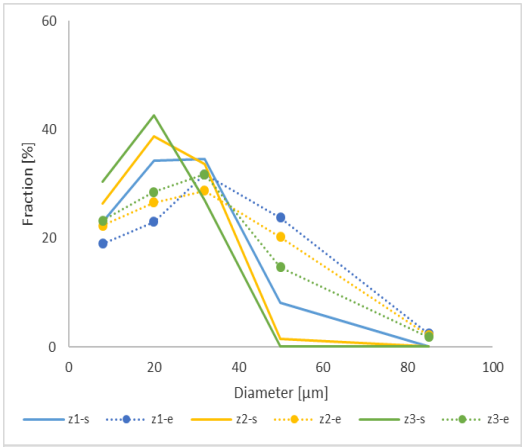

Run 2

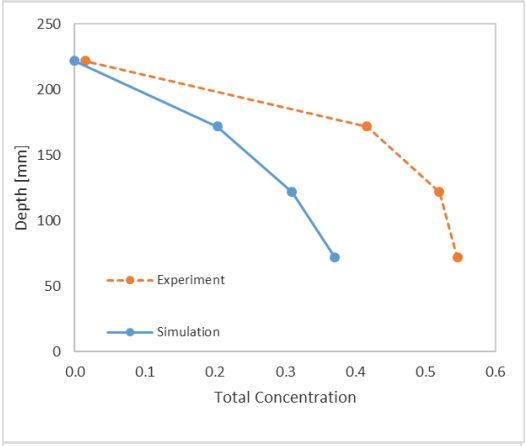

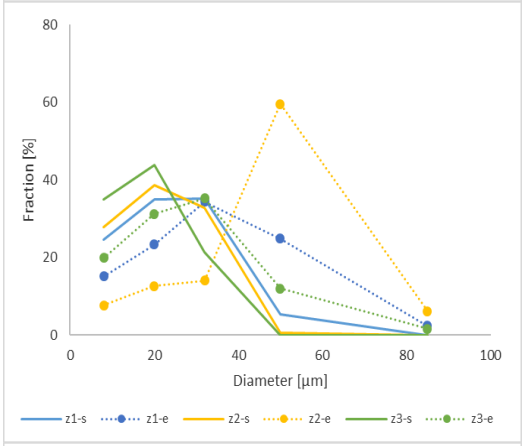

Run 3

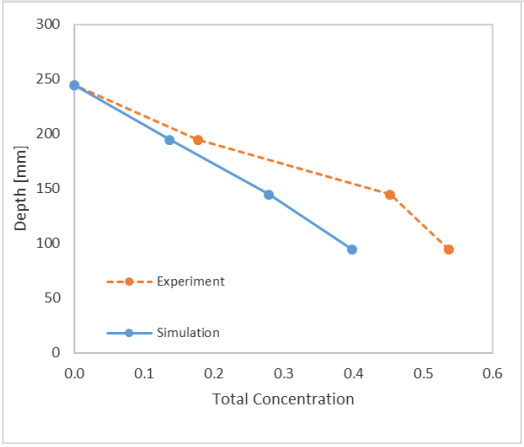

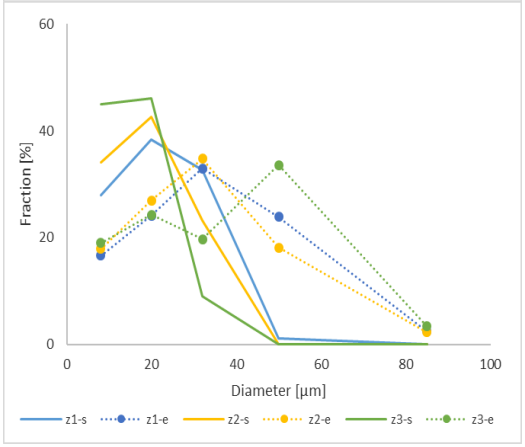

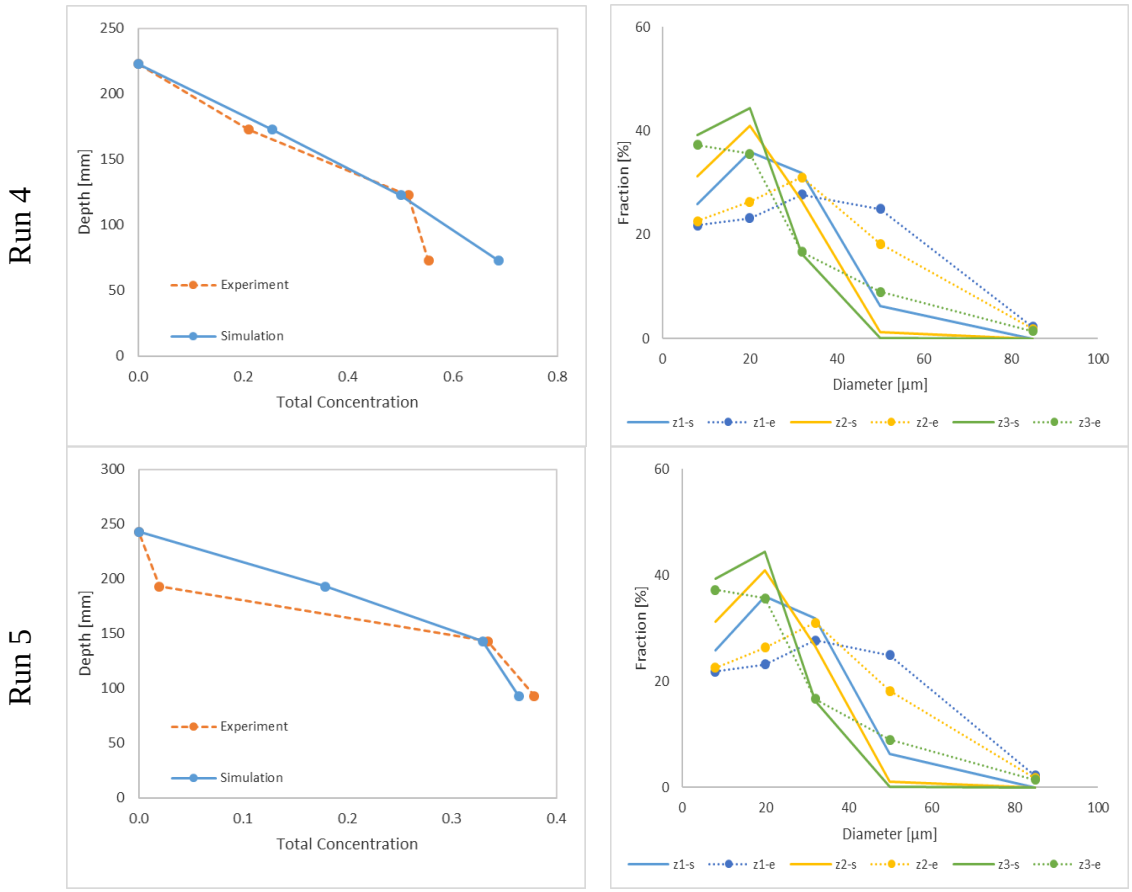

Figure 5.6: Vertical profile of the total sediment concentration (left panel) and the sediment fraction of each grain size of the mixture (right panel), at siphon 1. The profiles of the fractions are plotted at different locations in the vertical direction (zi, which correspond with the points of the total concentration vertical profile) (courtesy Shell Exploration)

Total Concentration

Sediment Fraction

Run 1

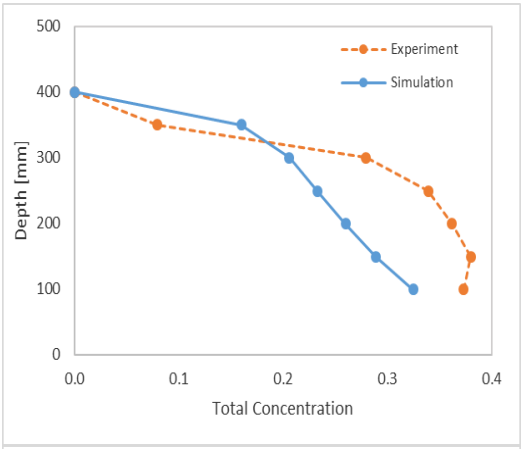

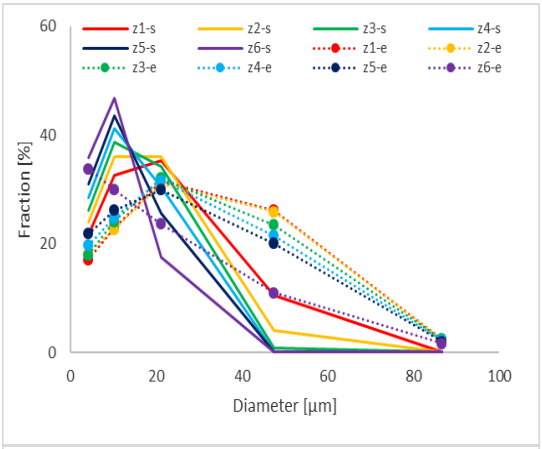

Run 2

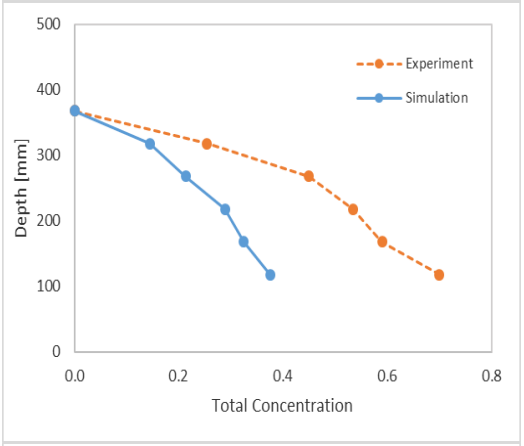

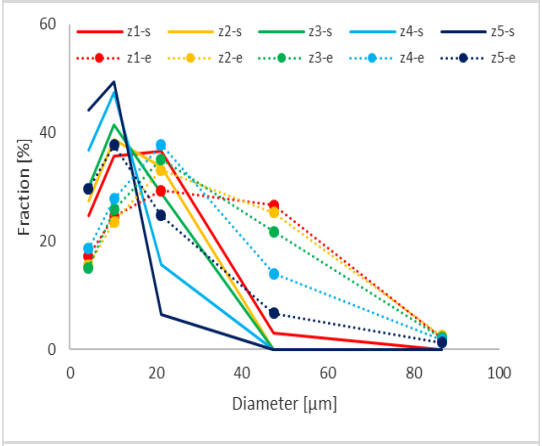

Run 3

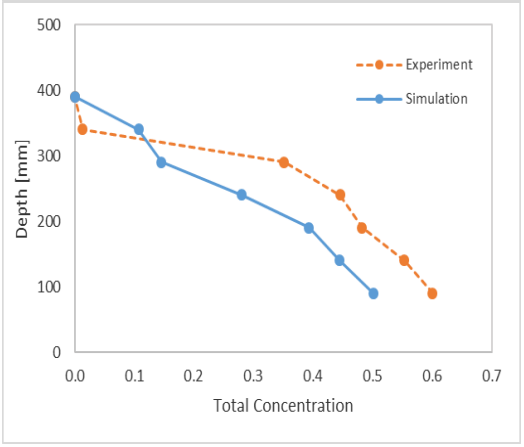

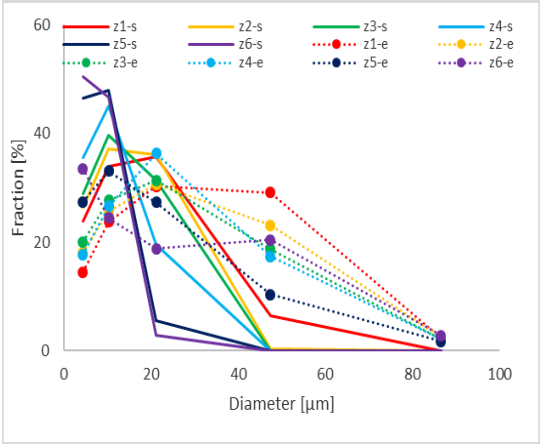

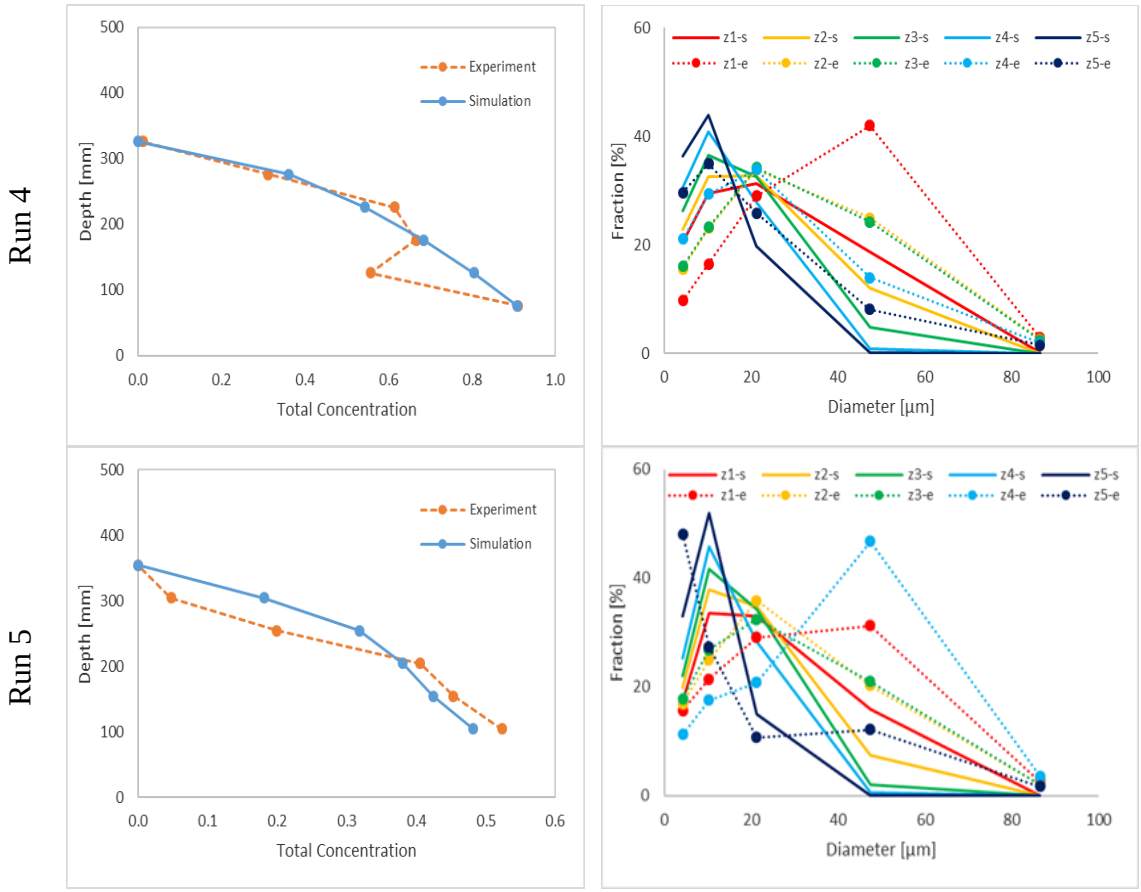

Figure 5.7: Vertical profile of the total sediment concentration (left panel) and the sediment fraction of each grain size of the mixture (right panel), at siphon 2. The profiles of the fractions are plotted at different locations in the vertical direction (zi, which correspond with the points of the total concentration vertical profile) (courtesy Shell Exploration)

Total Concentration

Sediment Fraction

Run 1

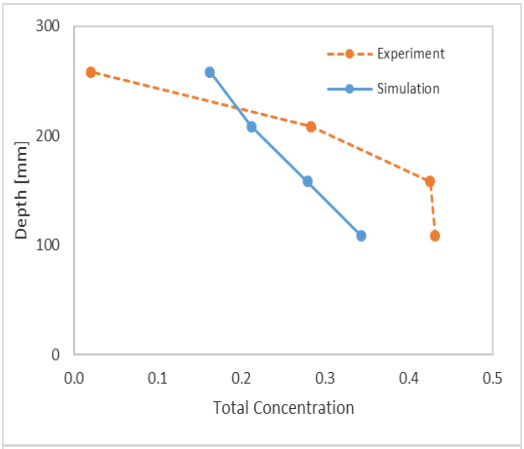

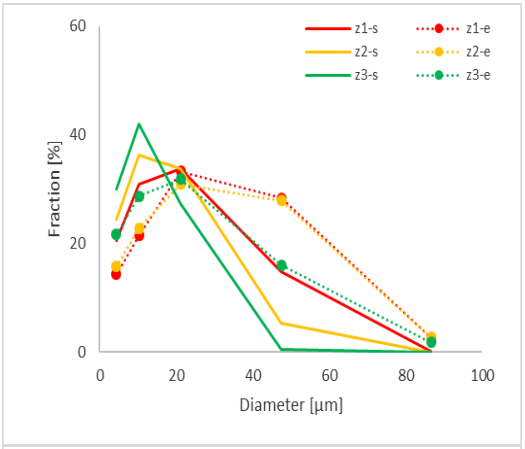

Run 2

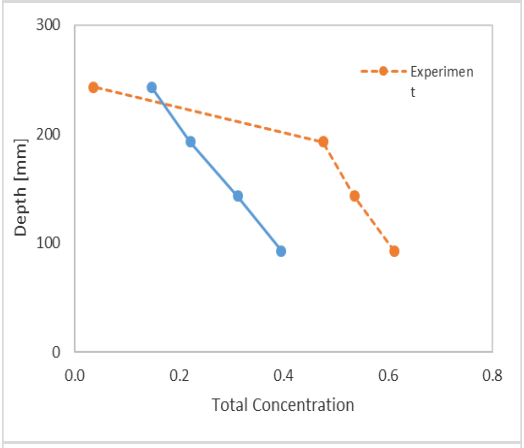

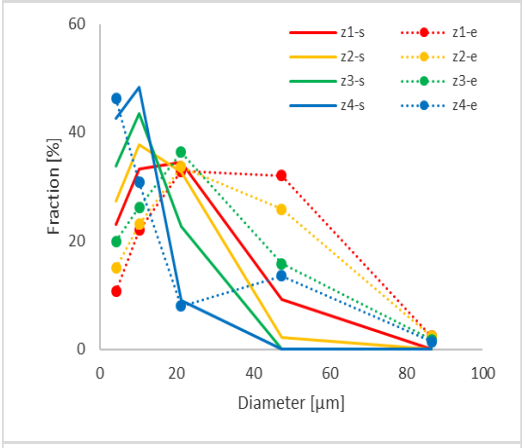

Run 3

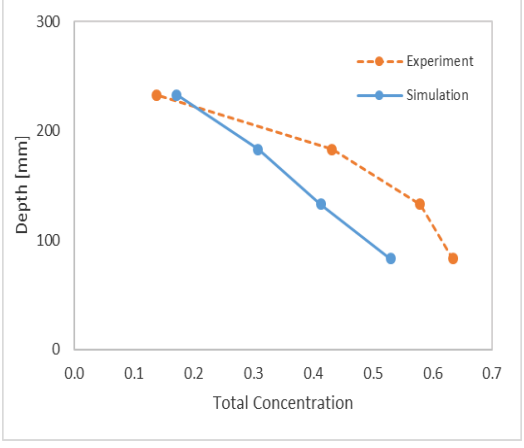

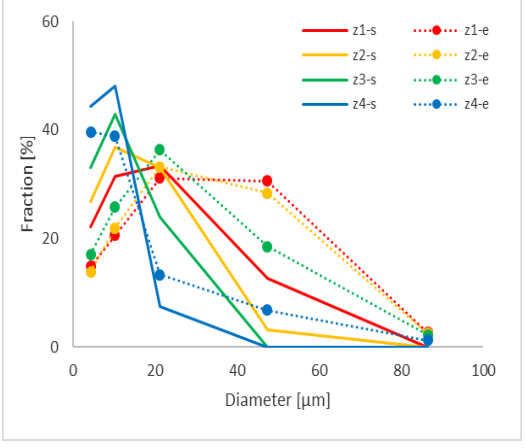

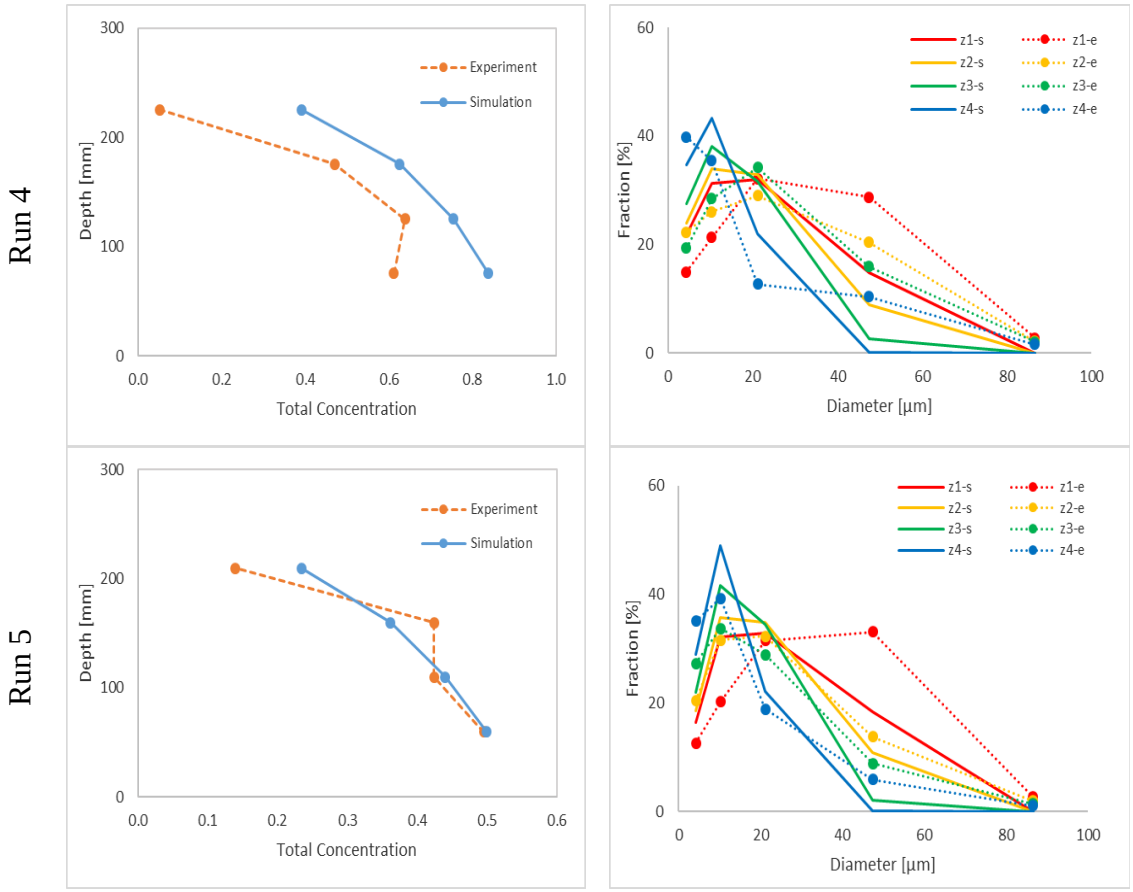

Figure 5.8: Vertical profile of the total sediment concentration (left panel) and the sediment fraction of each grain size of the mixture (right panel), at siphon 3. The profiles of the fractions are plotted at different locations in the vertical direction (zi, which correspond with the points of the total concentration vertical profile) (courtesy Shell Exploration)

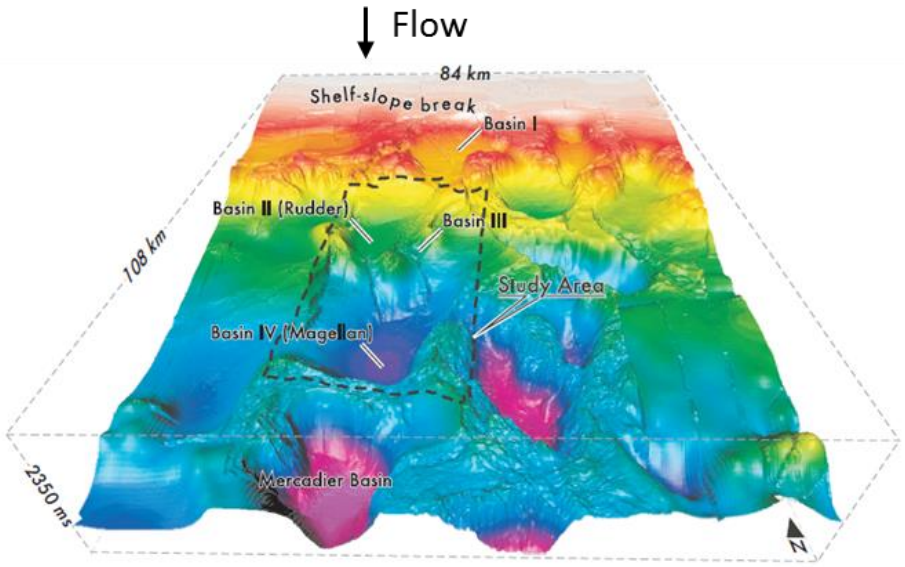

Figure 5.9: Minibasins system on the continental slope in the Gulf of Mexico (modified Prather et al., 2012)

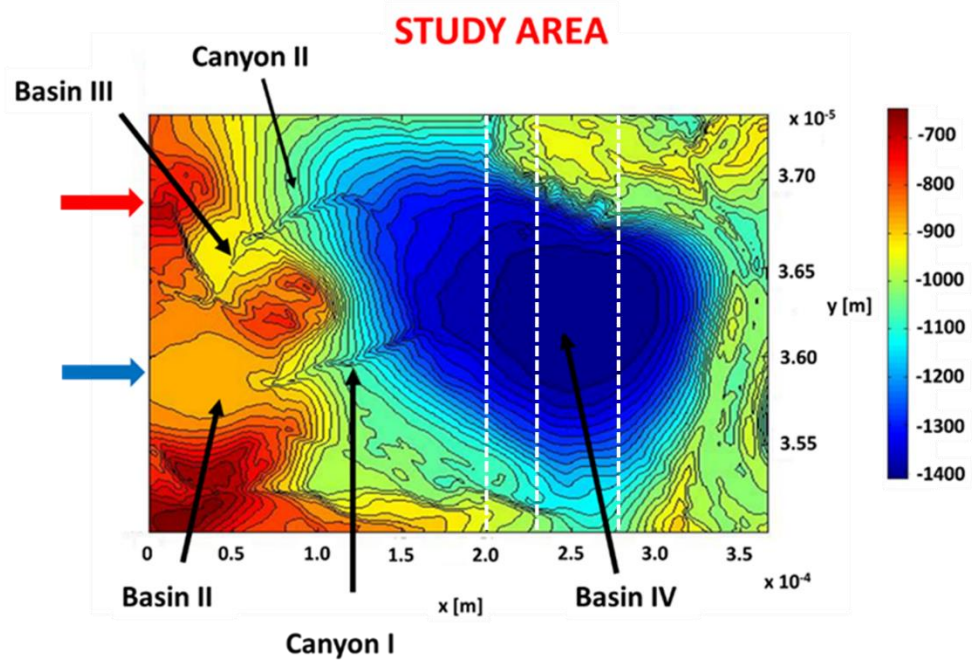

Figure 5.10: Initial bathymetry of the study area

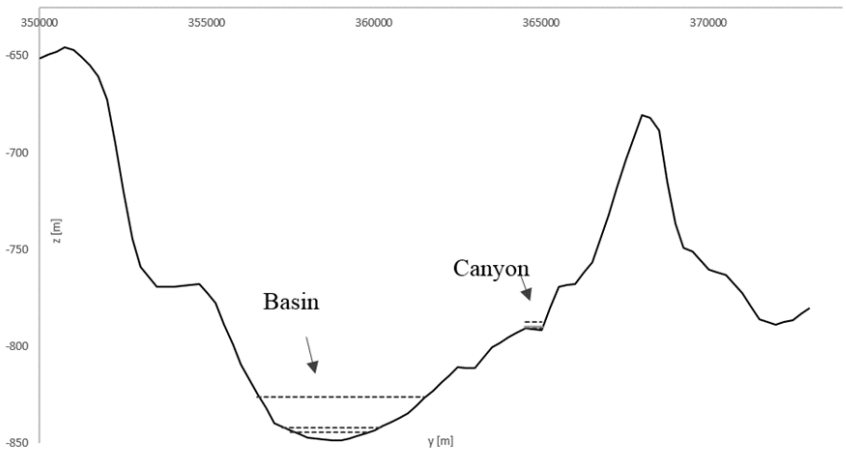

Figure 5.11: Inflow conditions of the turbidity current at the enter cross section (entrance from the canyon and entrance from the basin). The dashed lines show the current thickness at the entrance for the different conditions investigated (Small, Medium, and Large)

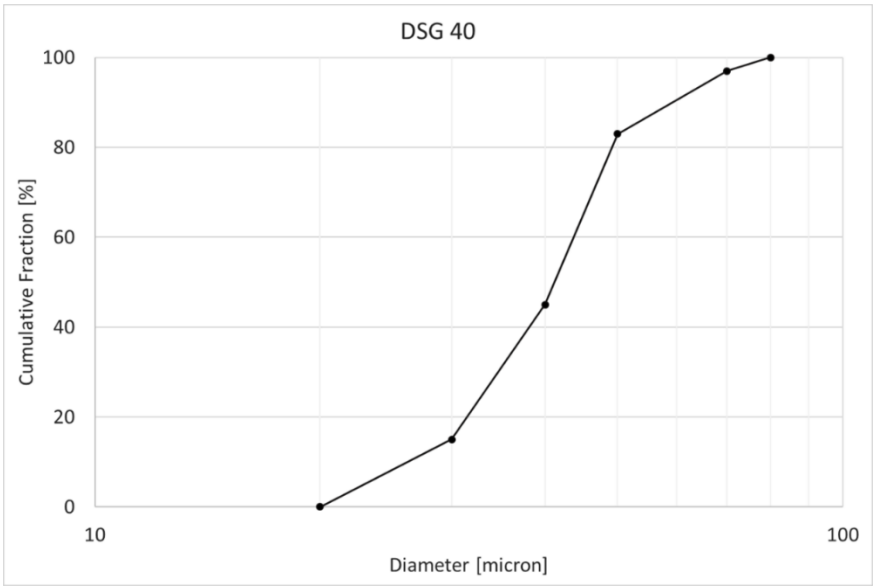

Figure 5.12: Grain size distribution of the turbidity current with unimodal grain size distribution with five characteristic grain sizes (D_g = 40 µm)

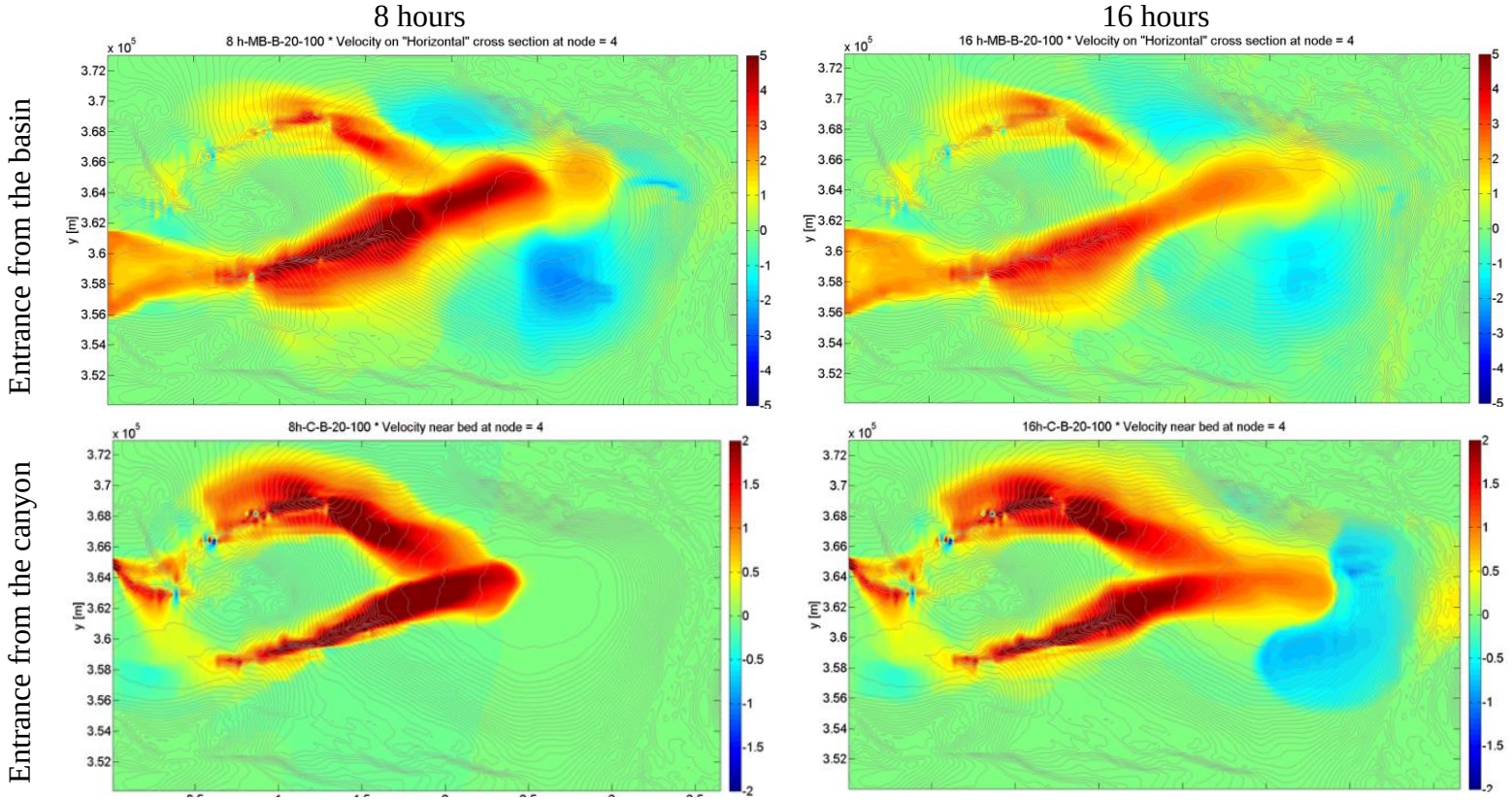

Figure 5.13: Near bed velocity (at 2.5 m from the bed) for the case of large current with bimodal grain size distribution (20-100 μm). The top panels represent the case in which the current enters from the basin, while in the bottom panels the current enters the domain from the canyon. On the left panels are the velocities profiles after 8 hours of simulated flow, while on the right is after 16 hours.

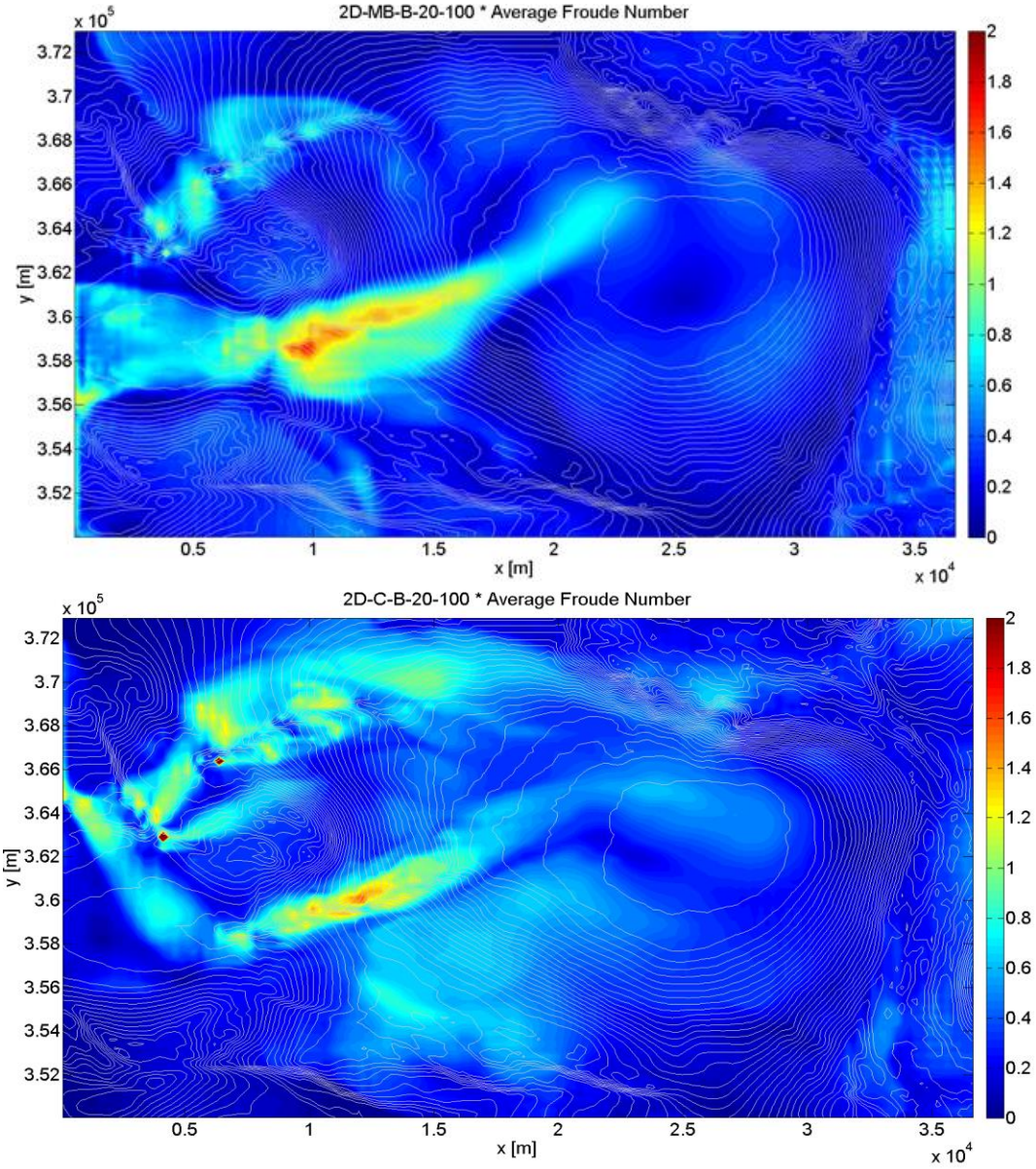

Figure 5.14: Densimetric Froude number after 2 days, for the case of large current from the minibasin (top) and from the canyon (bottom)

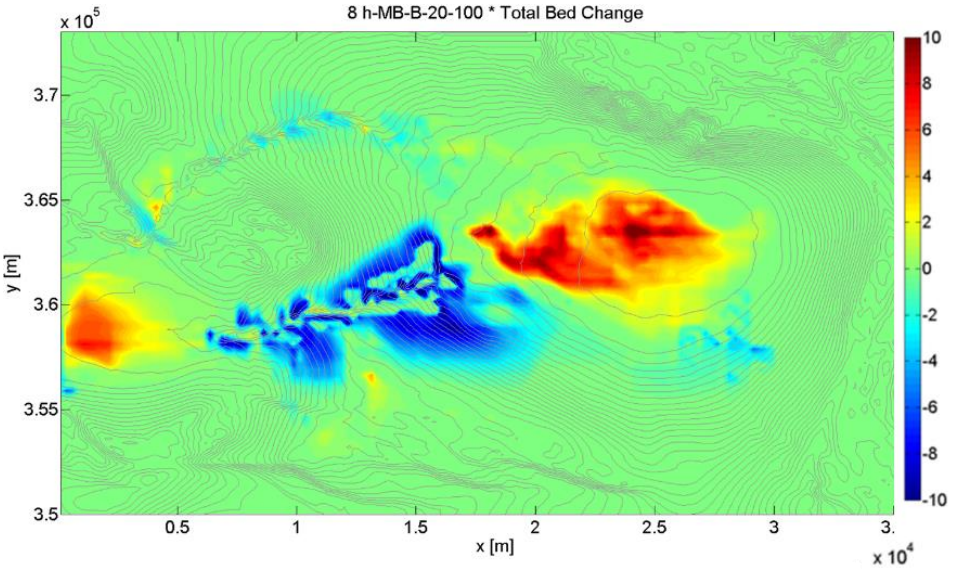
8 h-MB-B-20-100 * Total Bed Change
x 10^5
3.7
3.65
3.6
3.55
3.5
y [m]
0.5
1
1.5
2
2.5
3
3.
x [m]
x 10^4
10
8
6
4
2
0
-2
-4
-6
-8
-10

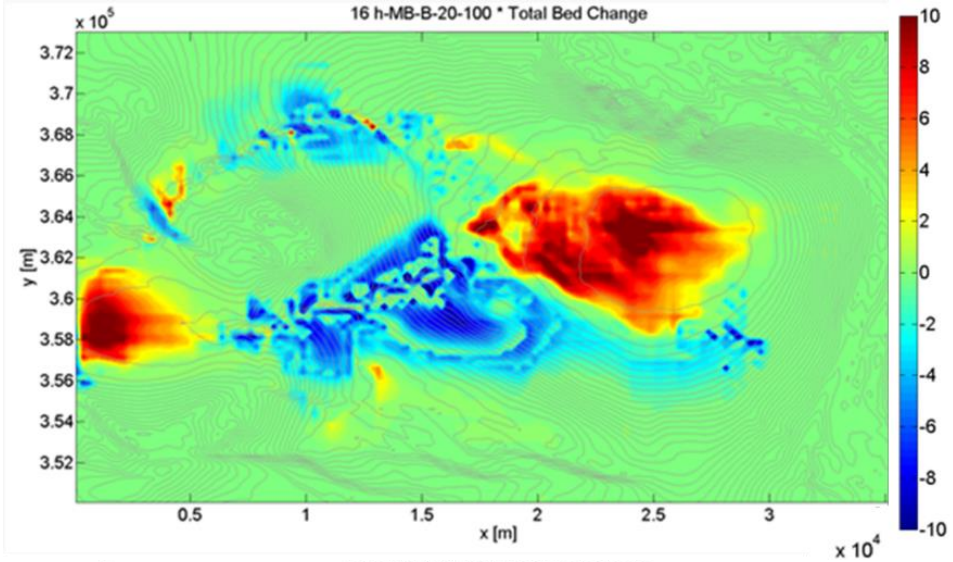
16 h-MB-B-20-100 * Total Bed Change
x 10^5
3.72
3.7
3.68
3.66
3.64
3.62
3.6
3.58
3.56
3.54
3.52
y [m]
0.5
1
1.5
2
2.5
3
x [m]
x 10^4
10
8
6
4
2
0
-2
-4
-6
-8
-10

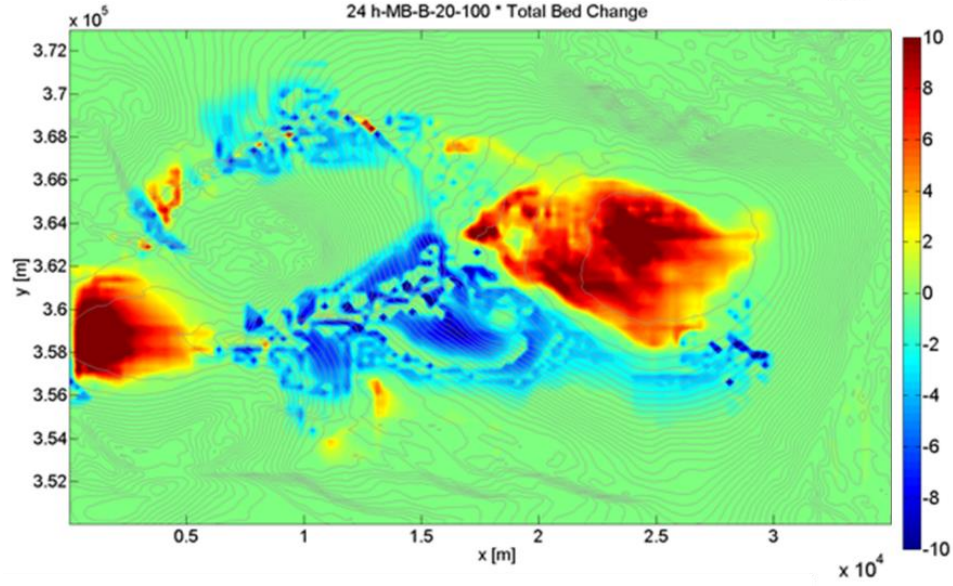
24 h-MB-B-20-100 * Total Bed Change
x 10^5
3.72
3.7
3.68
3.66
3.64
3.62
3.6
3.58
3.56
3.54
3.52
y [m]
0.5
1
1.5
2
2.5
3
x [m]
x 10^4
10
8
6
4
2
0
-2
-4
-6
-8
-10

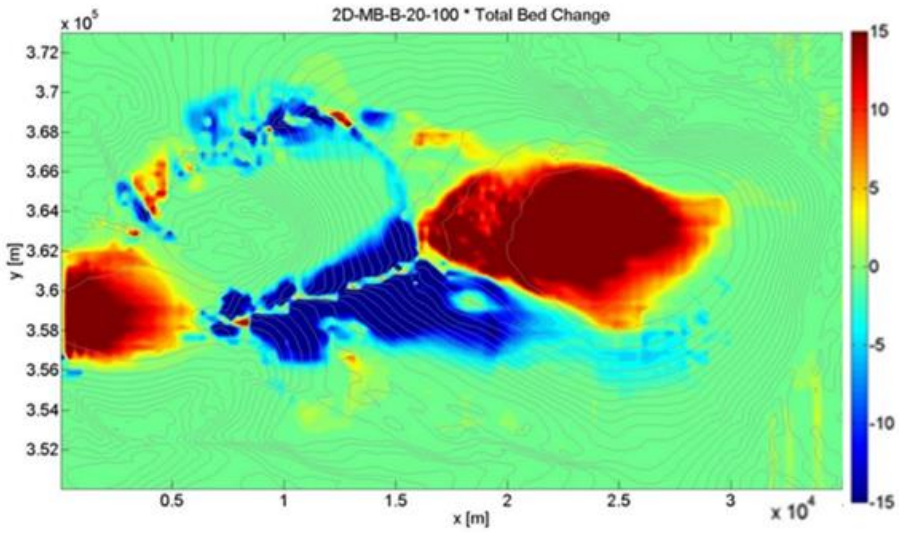

Figure 5.15: Total bed change after 8, 16, 24 and 48 hours for the case of a large current entering from the basin (20-100 μm)

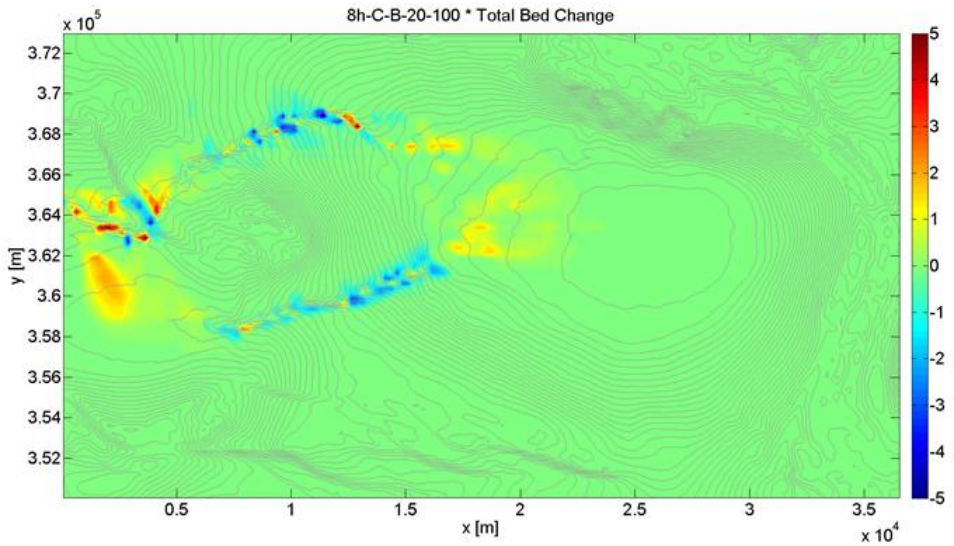
8h-C-B-20-100 * Total Bed Change
x 10^5
3.72
3.7
3.68
3.66
3.64
3.62
3.6
3.58
3.56
3.54
3.52
y [m]
0.5
1
1.5
2
2.5
3
3.5
x [m]
x 10^4
5
4
3
2
1
0
-1
-2
-3
-4
-5

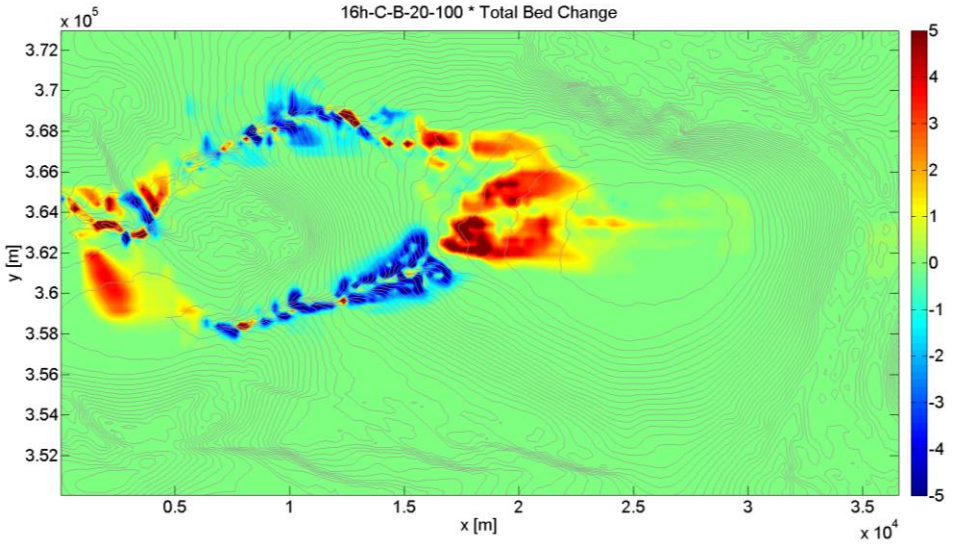
16h-C-B-20-100 * Total Bed Change
x 10^5
3.72
3.7
3.68
3.66
3.64
3.62
3.6
3.58
3.56
3.54
3.52
y [m]
0.5
1
1.5
2
2.5
3
3.5
x [m]
x 10^4
5
4
3
2
1
0
-1
-2
-3
-4
-5

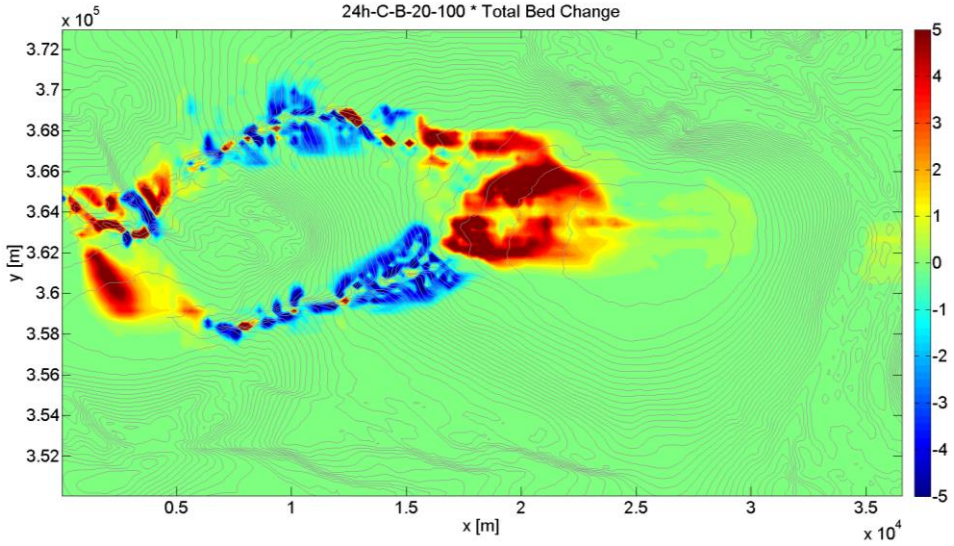
24h-C-B-20-100 * Total Bed Change
x 10^5
3.72
3.7
3.68
3.66
3.64
3.62
3.6
3.58
3.56
3.54
3.52
y [m]
0.5
1
1.5
2
2.5
3
3.5
x [m]
x 10^4
5
4
3
2
1
0
-1
-2
-3
-4
-5

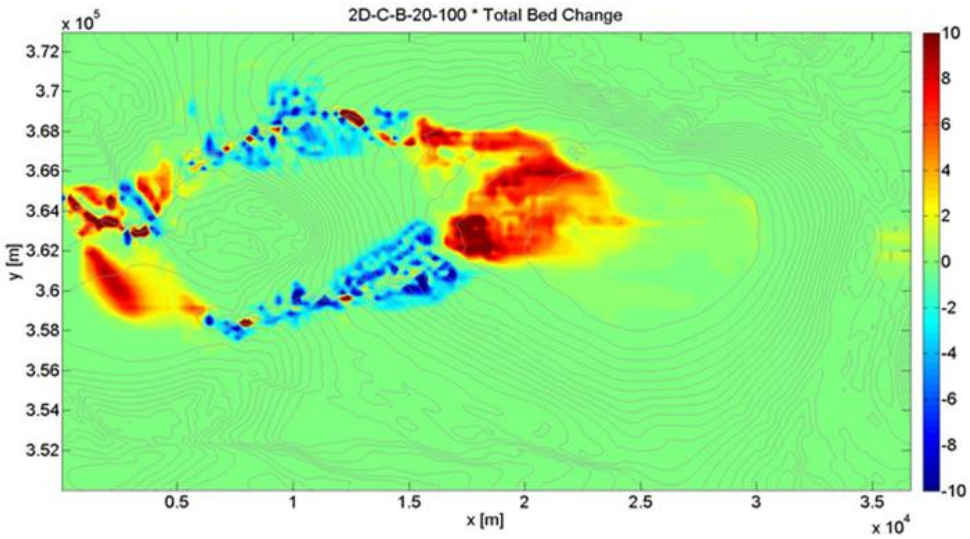

Figure 5.16: Total bed change after 8, 16, 24 and 48 hours for the case of a large current entering from the canyon (20-100 µm)

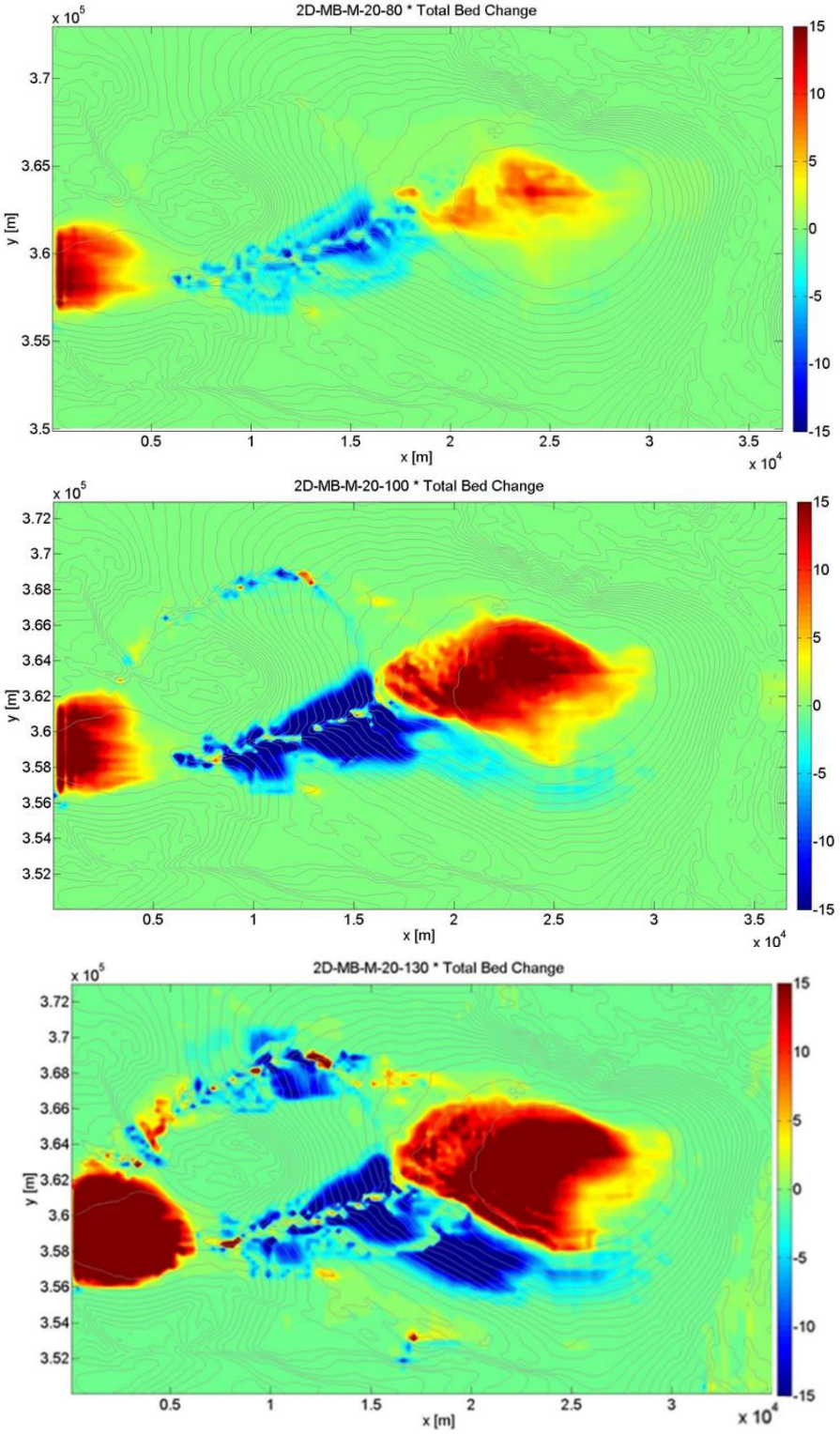

Figure 5.17: Deposit thickness after 2 days of the medium current entering from the basin; for fine (20-80 μm – top), medium (20-100 μm – middle) and coarse (20-130 μm – bottom) grain size distribution

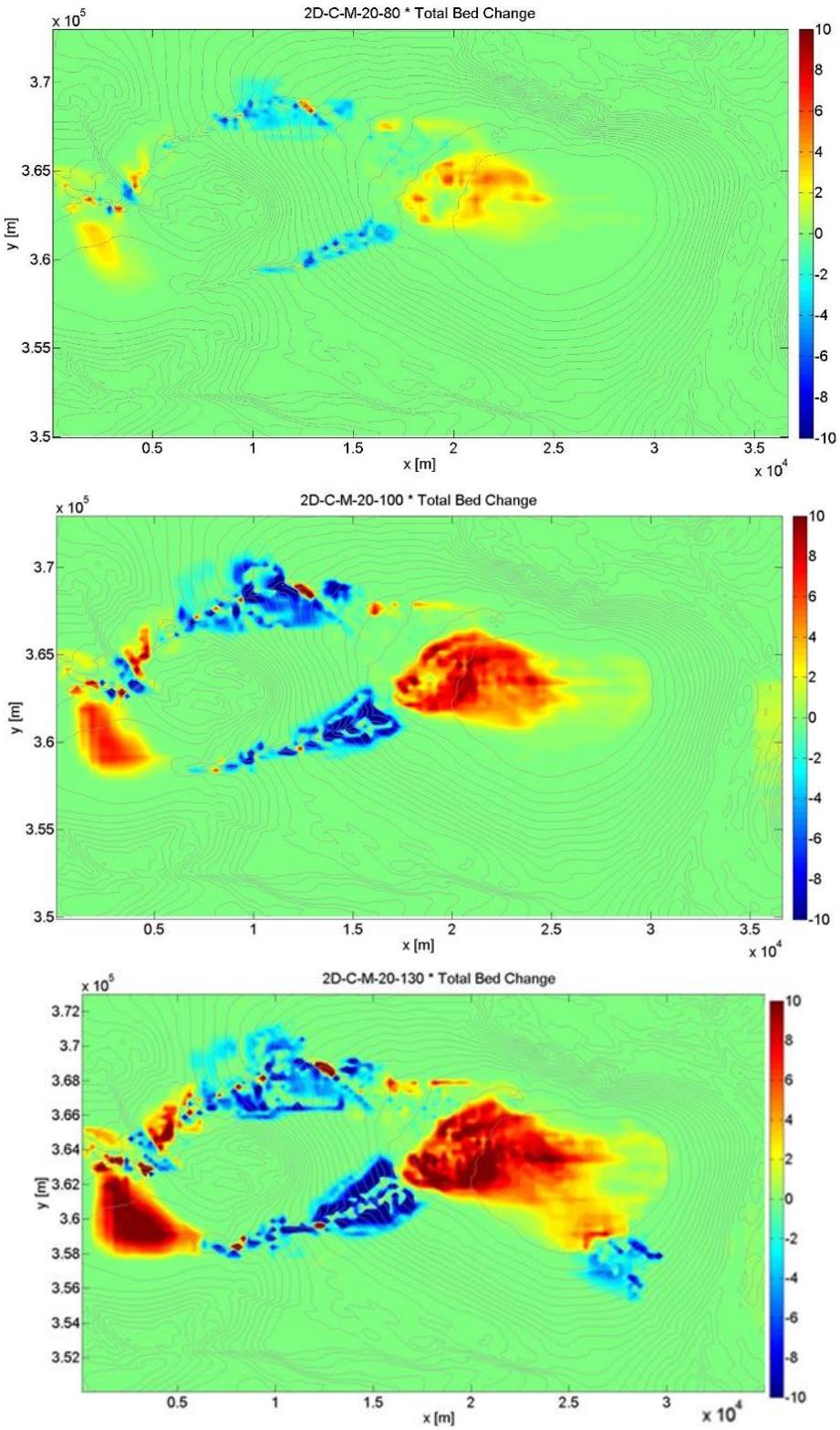

Figure 5.18: Total bed change after 2 days of the medium current entering from the basin; for fine grain (20-80 μm – top), medium (20-100 μm – middle) and coarse (20-130 μm – bottom) size distribution

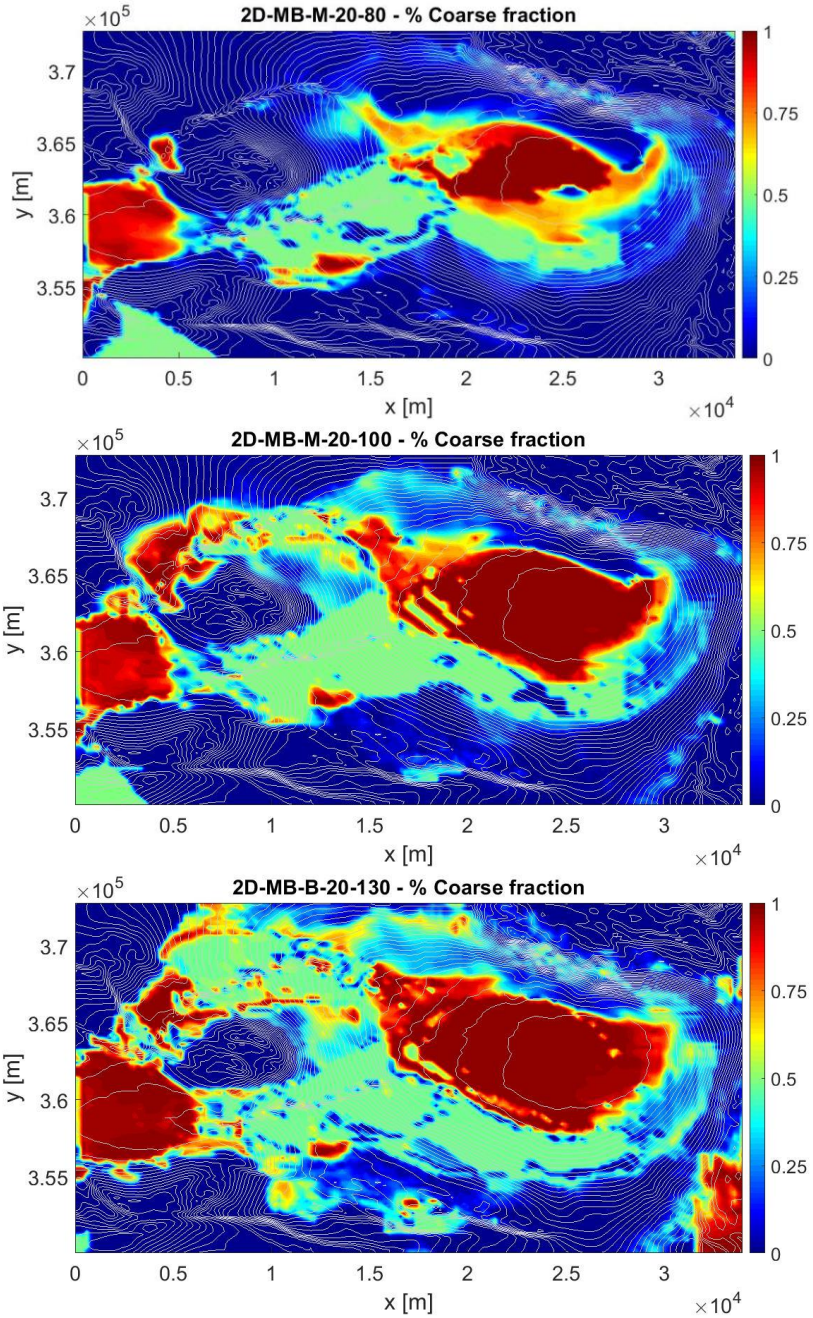

Figure 5.19: Volume fraction content of the coarse grain size (initial fraction: 0.5) after 2 days for the medium current entering from the basin; for fine (20-80 μm – top), medium (20-100 μm – middle) and coarse (20-130 μm – bottom) grain size distribution

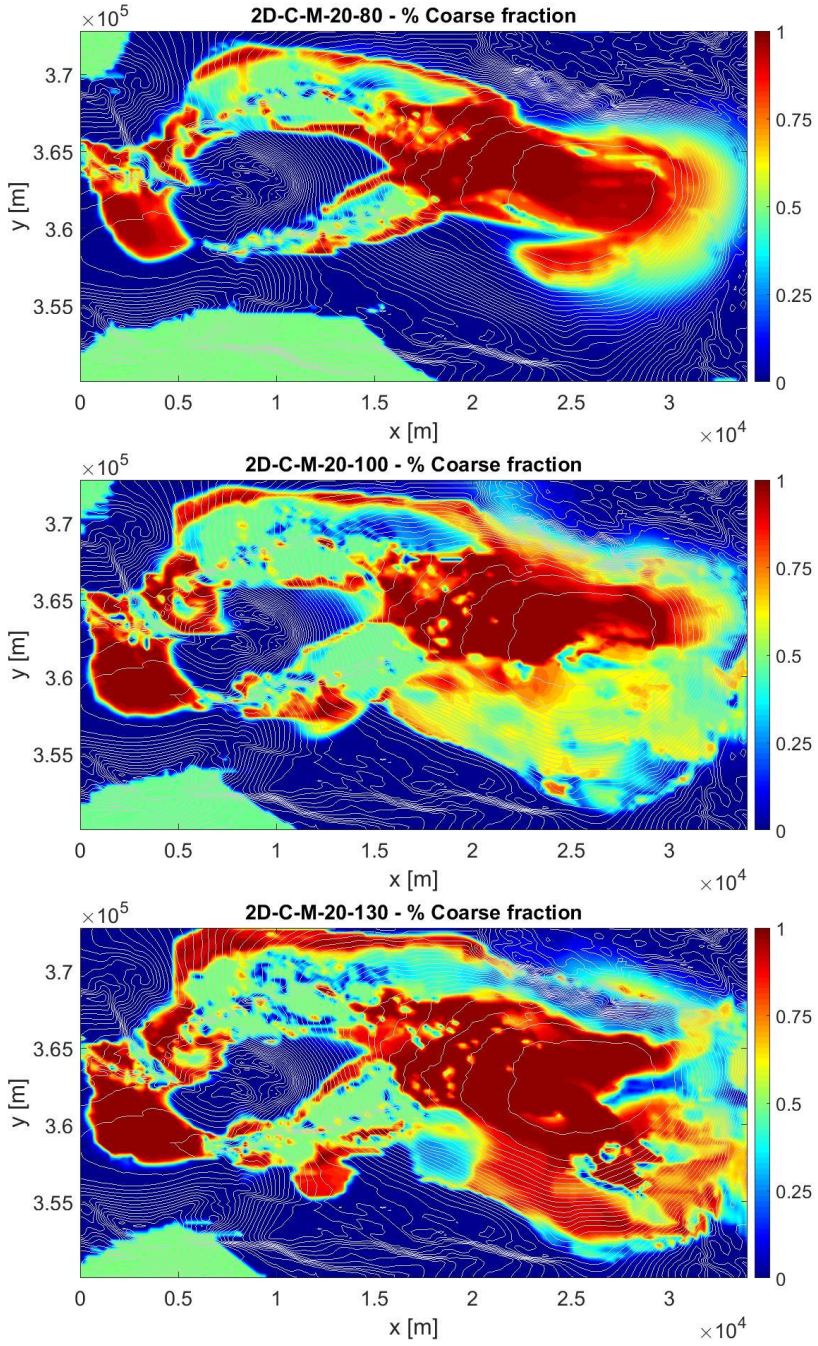

Figure 5.20: Volume fraction content of the coarse grain size (initial fraction: 0.5) after 2 days for the medium current entering from the canyon; for fine (20-80 μm – top), medium (20-100 μm – middle) and coarse (20-130 μm – bottom) grain size distribution

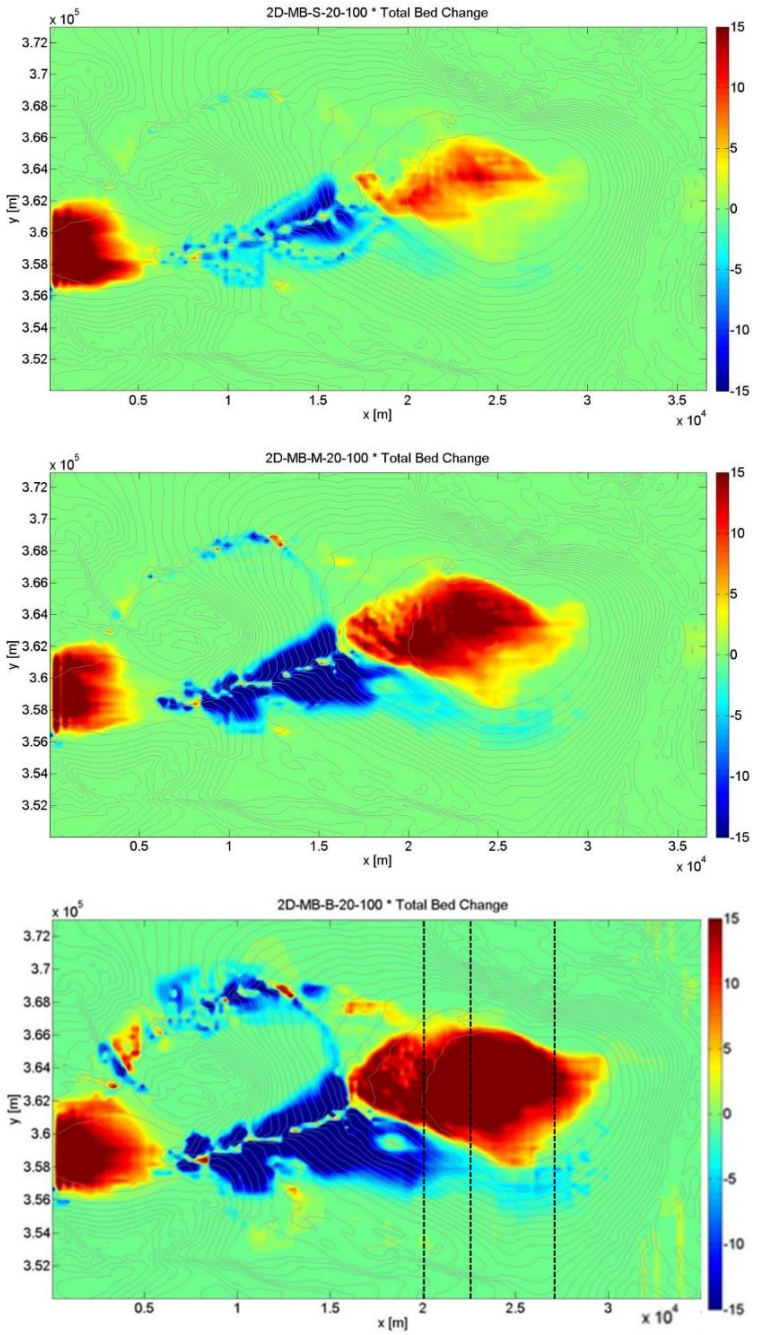

Figure 5.21: Total bed change after 2 days of a current entering from the basin with bimodal sediment distribution (20-100 μm); of a small (top), medium (middle) and large (bottom) current

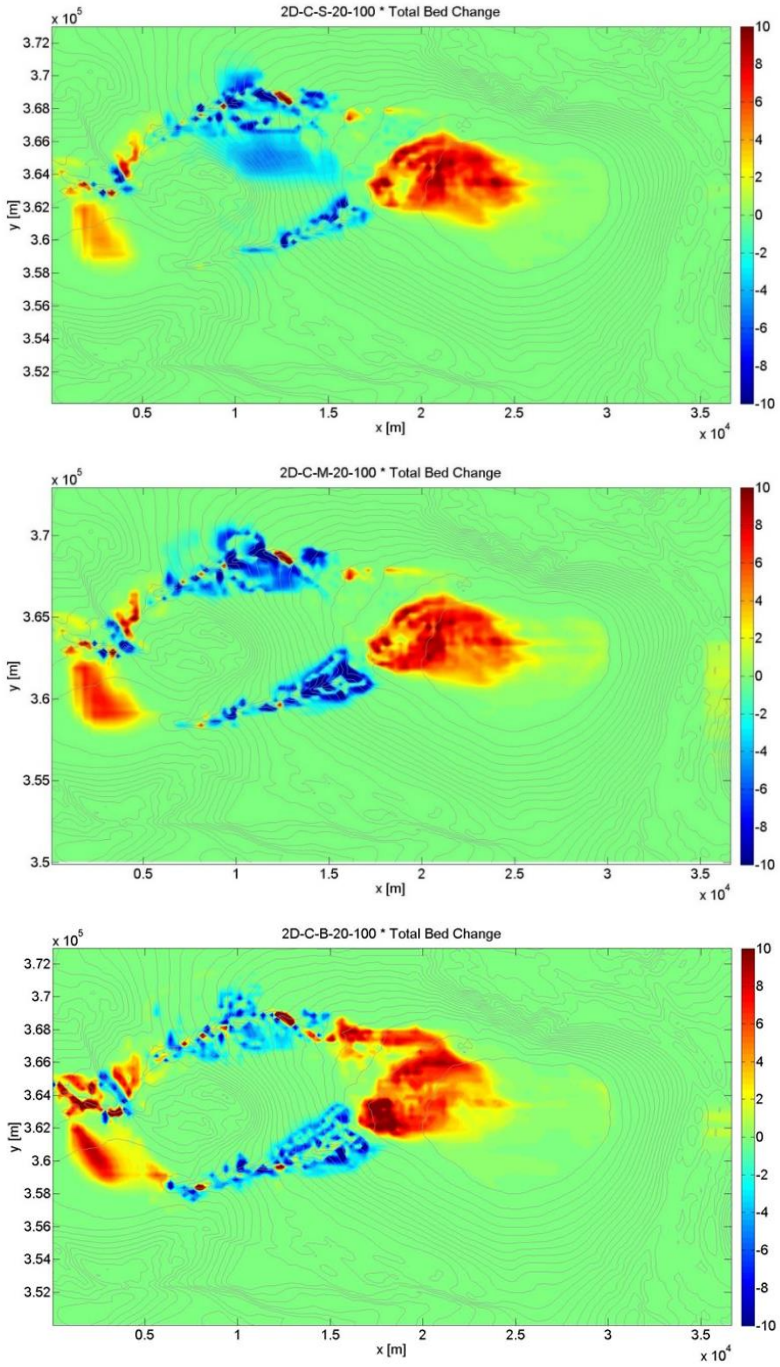

Figure 5.22: Total bed change after 2 days of a current entering from the canyon with bimodal distribution (20-100 μm); with small (top), medium (middle) and large (bottom) current

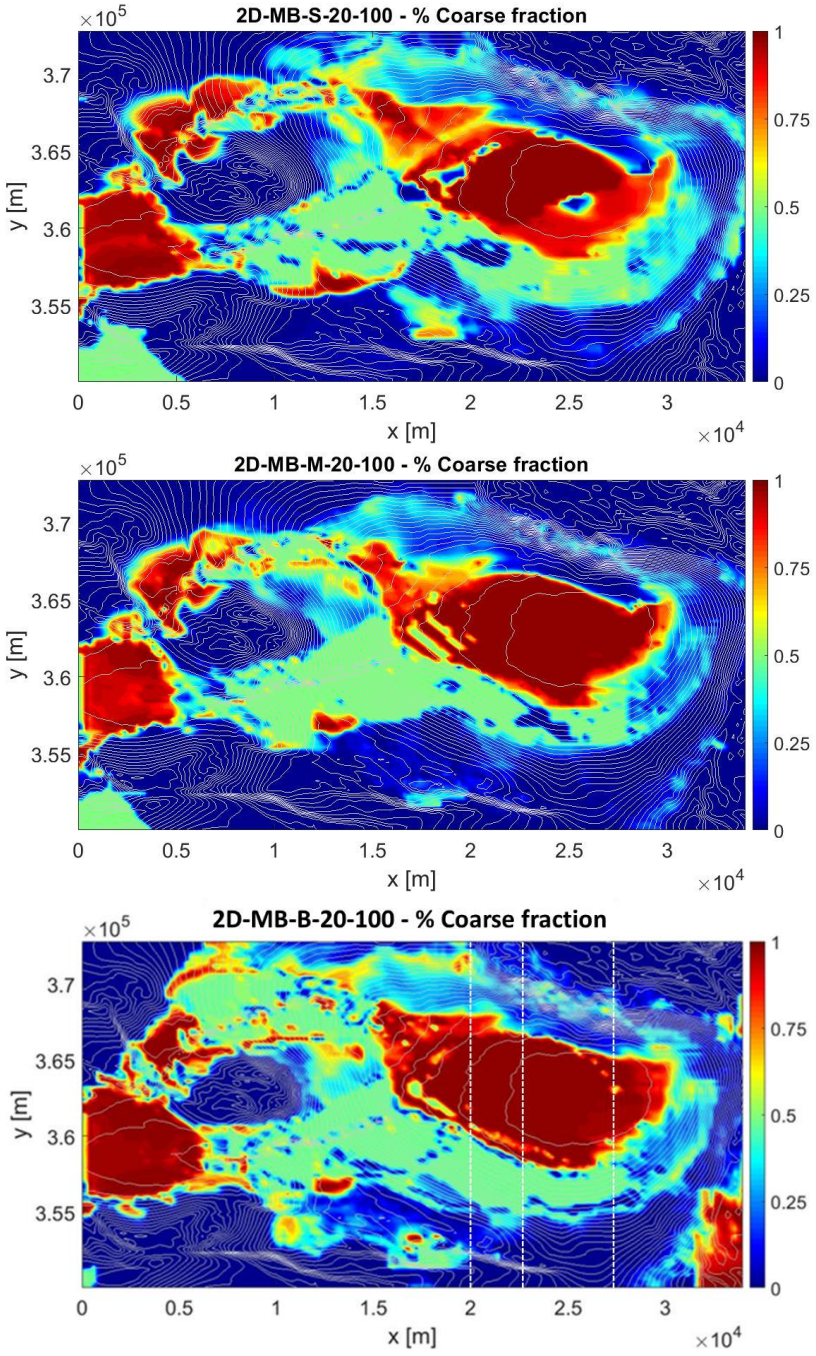

Figure 5.23: Volume fraction content of the coarse grain size (initial fraction: 0.5) after 2 days of a simulated current entering from the basin with bimodal distribution (20-100 μm); with small (top), medium (middle) and large (bottom) current

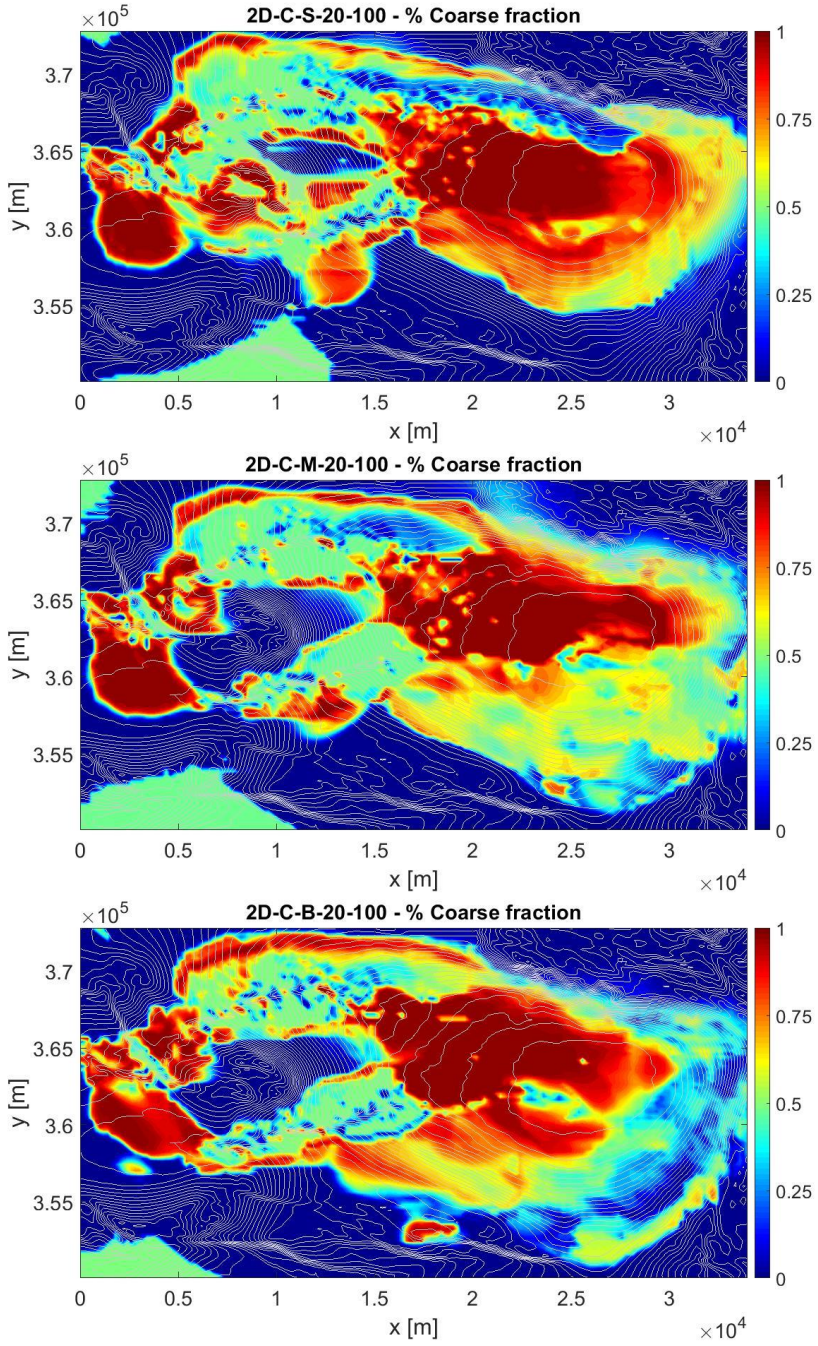

Figure 5.24: Volume fraction content of the coarse grain size (initial fraction: 0.5) after 2 days of a current entering from the canyon with bimodal distribution (20-100 μm); with small (top), medium (middle) and large (bottom) current

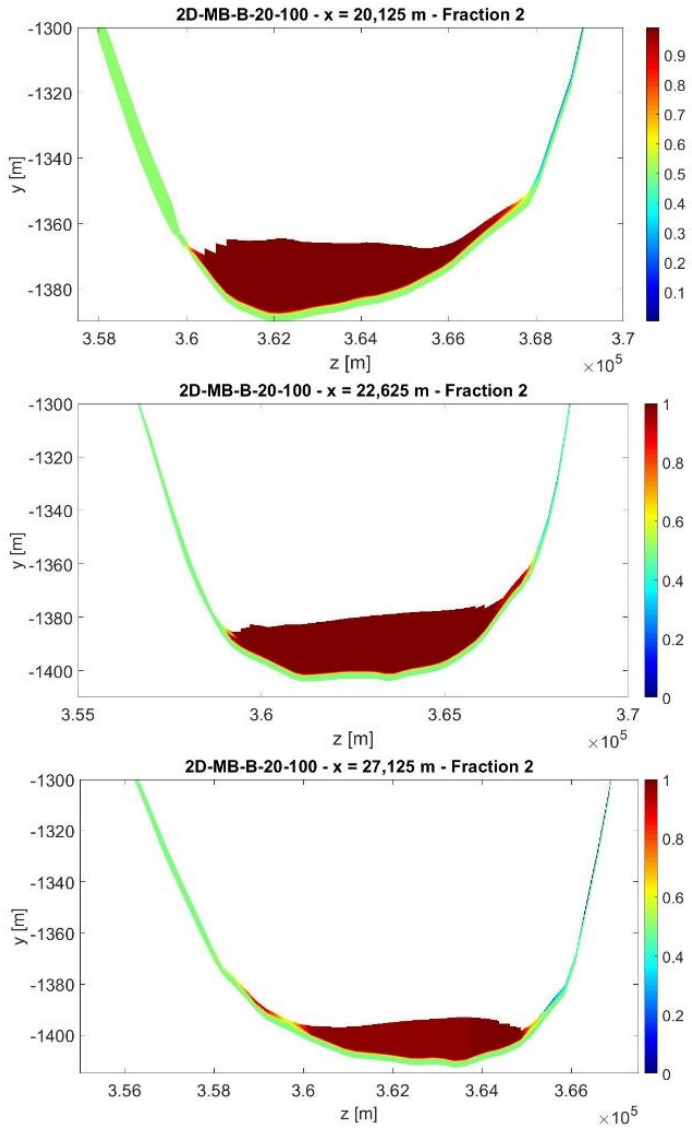

Figure 5.25: Volume fraction content of the coarse grain size (initial fraction: 0.5) after 2 days of a large current entering from the basin with bimodal distribution (20-100 μm), at different cross section as highlighted in Figure 5.21 (bottom panel)

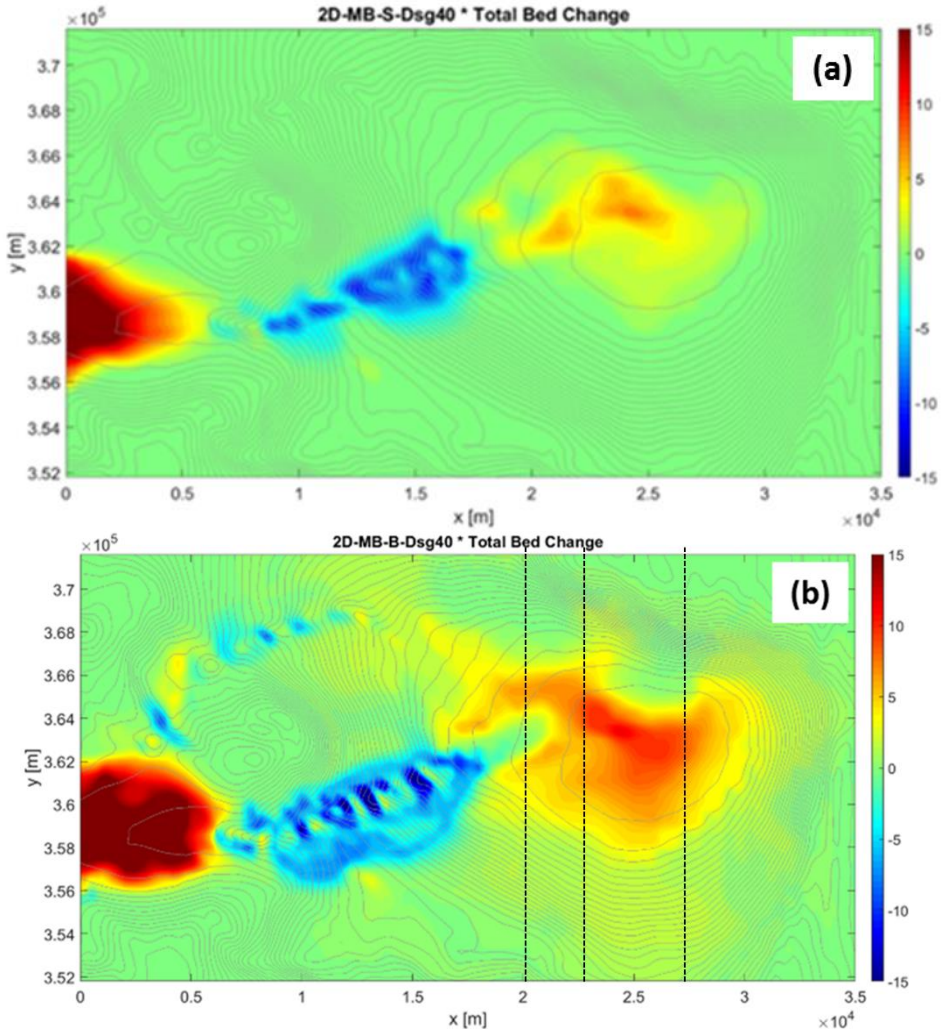

Figure 5.26: Deposit thickness after two days of simulated flow, for the case of small (a) and a large (b) current characterized by sediment mixture, entering from the basin

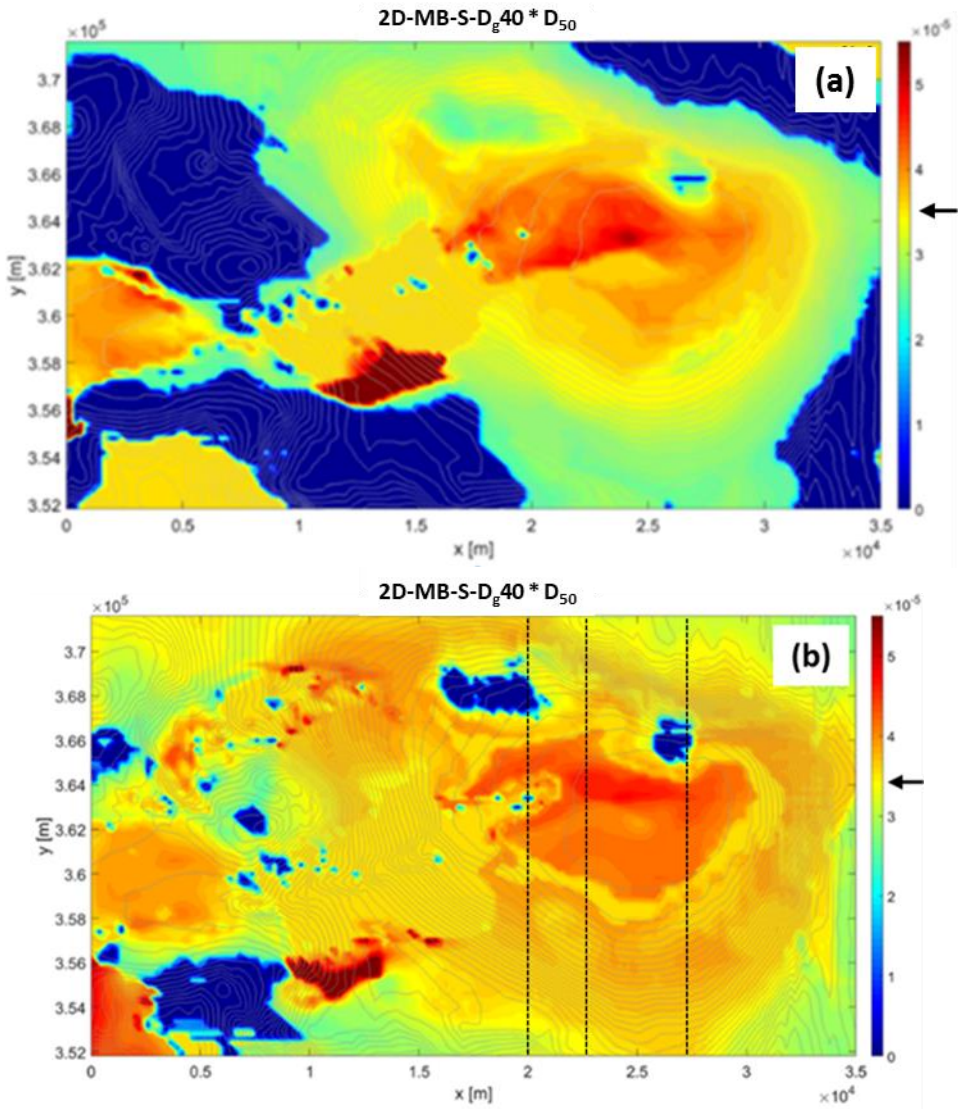

Figure 5.27: Sediment median diameter of the deposit after two days of simulated flow for the case of a small (a) and a large (b) current characterized by sediment mixture, entering from the basin

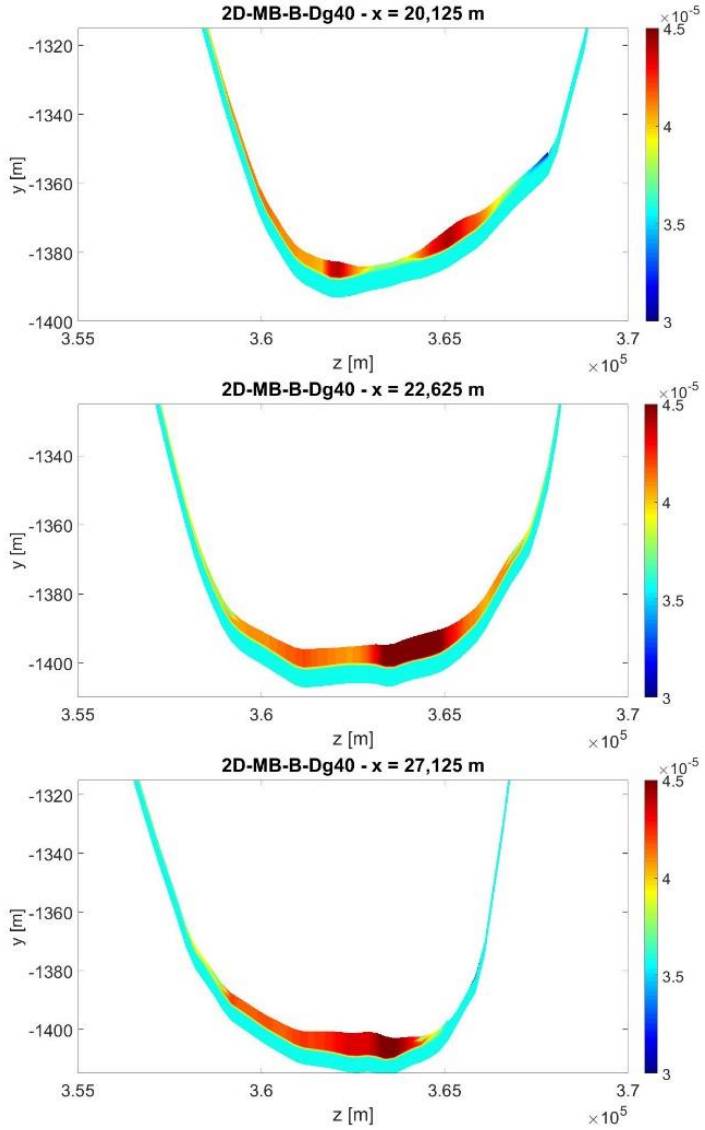

Figure 5.28: Median diameter (D_{50}) after 2 days of a large current entering from the basin a grain size distribution characterized by D_{50} = 41.2 µm, at different cross section as highlighted in Figure 5.10

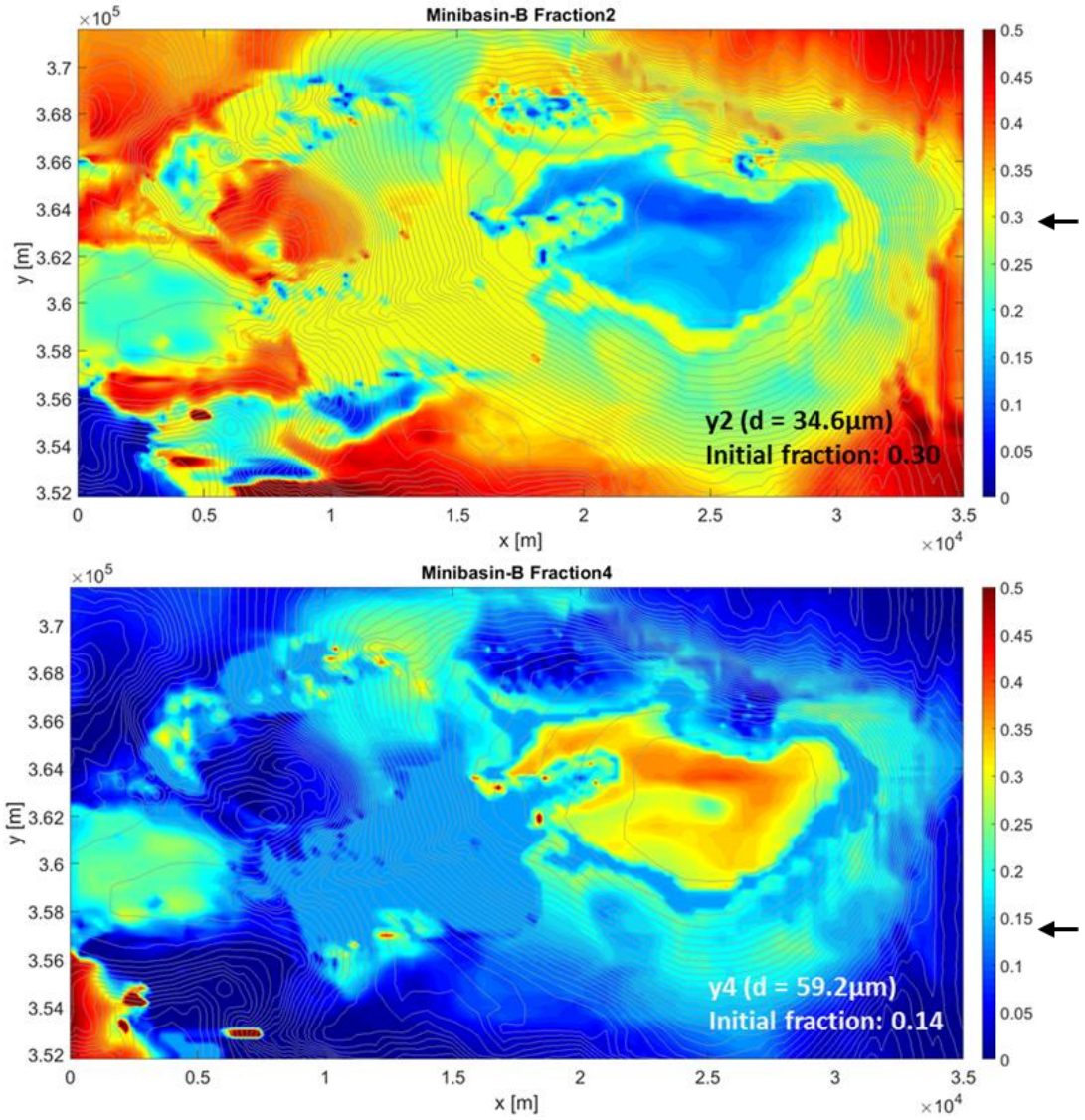

Figure 5.29: Fraction of D2 (34.6 µm) and D4 (60 µm) on the deposit, after two days for the case of large current characterized by sediment mixture, entering from the basin

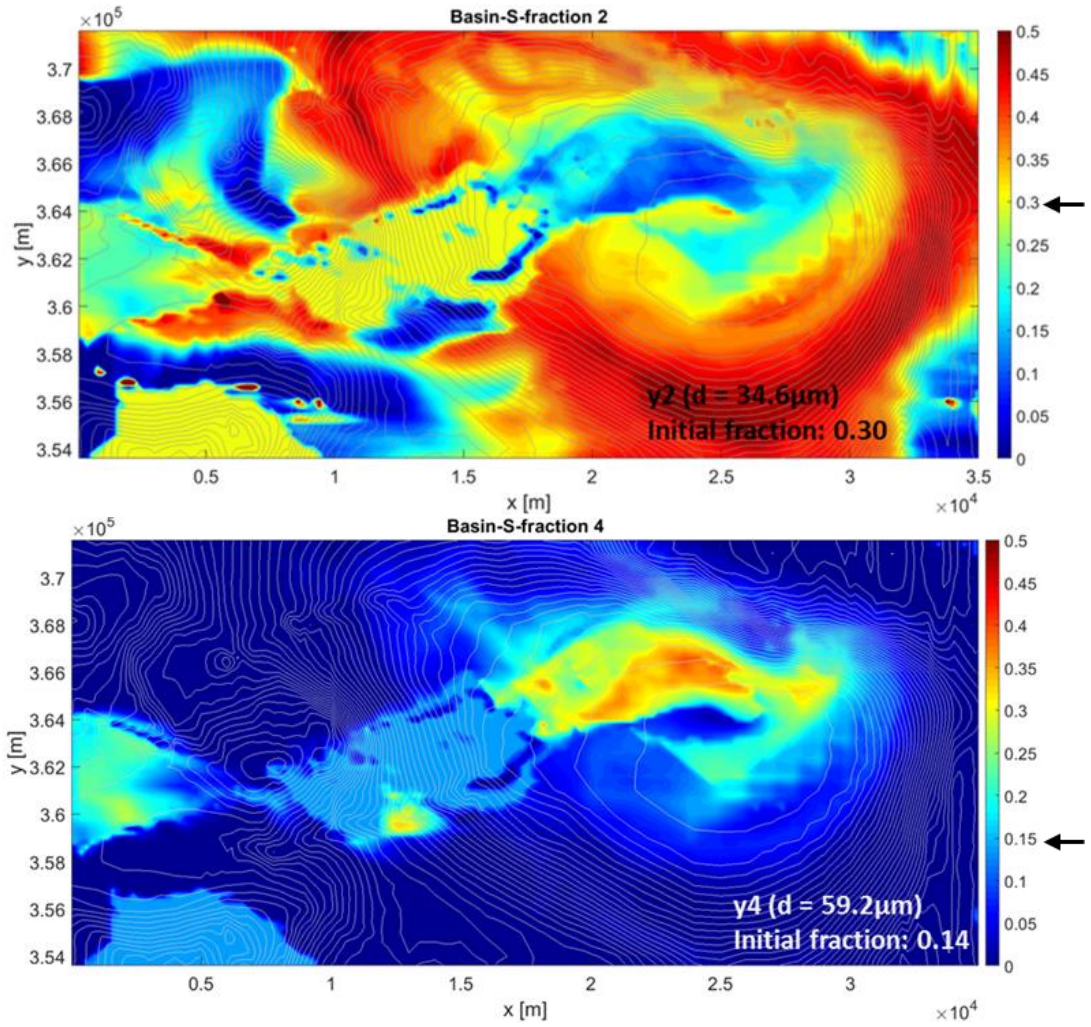

Figure 5.30: Fraction of D2 (34.6 µm) and D4 (60 µm) on the deposit, after two days for the case of small current characterized by sediment mixture, entering from the basin

CHAPTER 6

SUMMARY AND CONCLUSIONS

Submarine minibasins are seafloor morphological features with a nearly elliptical shape that are prime targets for hydrocarbon exploration. Sedimentation in submarine minibasins driven by turbidity currents and other types of submarine flows has been studied with the collection and analysis of field data, laboratory experiments and numerical models. These studies notwithstanding questions regarding how the characteristics of minibasin deposits emplaced by turbidity currents depend on the magnitude of the turbidity current relative to the minibasin size, the minibasin geometry and the grain size characteristics of the transported sediment remain largely unanswered. The study presented in this dissertation was designed to answer these questions with the aid of a numerical model.

The numerical model used herein, TC-SOLVER, is a three dimensional in-house developed code of turbidity current morphodynamics with a deforming bottom boundary that solves the Reynolds Averaged Navier-Stokes equations with different turbulence models. A k-ε turbulence model has been used in the simulations presented in Chapters 2-5 of this dissertation.

For this study TC-SOLVER has been modified with the implementation of 1) a procedure to store and access the grain size stratigraphy of the deposit, and 2) a procedure

to reduce the computational cost of the morphodynamic simulations. The implementation of the procedure to store and access the grain size stratigraphy of the deposit consists in the definition of a storage grid, as illustrated in Chapter 2. The reduction of the computational cost of the morphodynamic calculation is performed using a Morphological Acceleration Factor (MORFAC) that amplifies the morphodynamic time step compared to the time step controlling the hydraulic calculations, as illustrated in Chapters 3.

The modified TC-SOLVER is first validated against 2D and 3D laboratory experiments on 1) turbidity currents flowing over a break in slope (2D), 2) turbidity currents in a 2D model submarine minibasin, and 3) turbidity currents in a 3D model submarine minibasin. The main differences between the 2D and 3D model minibasin relevant for this study is that in the 3D case the minibasin width changed in the flow direction and thus the current was allowed to expand laterally.

The validated model is then used to determine if the morphological acceleration factor, commonly used in studies of tidal morphodynamics can be reasonably applied to study sedimentation processes driven by turbidity currents, and to perform 2D and 3D field scale simulations on sedimentation in intraslope minibasins using the present seafloor bathymetry of the Gulf of Mexico in the area of the Brazos-Trinity system.

The study on the application of the Morphological Acceleration Factor (MORFAC) to study turbidity current morphodynamics is performed in two phases. The model is first applied at laboratory scale to simulate the case of a turbidity current flowing over a break in slope and the results are compared against measured data of changes in bed elevation and suspended sediment concentration. The model is then applied to simulate field scale

simplified geometries to investigate if the results of the laboratory simulations can be used for large scale morphodynamic studies.

The simulations are performed with values of MORFAC equal to 2, 5 and 10. Further, noting that the passage of a turbidity current front may result in significant morphodynamic changes, MORFAC is applied in two different ways: 1) MORFAC is applied from the beginning of the simulations, i.e. the time step for the morphodynamic calculations is always multiplied by MORFAC, or 2) MORFAC is applied to model the morphodynamics of the turbidity current body, i.e. the morphodynamic time step is equal to the hydraulic time step when the turbidity current front is in the model domain, and it is larger than the hydraulic time step when the turbidity current body occupies the entire computational domain.

The simulations presented in Chapter 3 of this dissertation show that the agreement between laboratory experiments and morphodynamic simulations performed with MORFAC is reasonable when the acceleration factor is applied at the beginning of the simulations. On the contrary, the comparison between numerical results performed with and without MORFAC at field scales in simplified settings reveals that the acceleration factor should be applied to simulate the morphodynamics of the turbidity current body only. In other words, the results presented in Chapter 3 show that at field scales MORFAC should only be applied after the passage of the turbidity current front. Finally, the simulations presented herein show that for the case of turbidity current morphodynamics values of MORFAC greater than 5 should only be used with great care at laboratory and field scales.

Two-dimensional simulations are performed on a dip section from Basin II to Basin IV of the present seafloor of the Trinity-Brazos system in the Gulf of Mexico. The objective

of these simulations is to study the characteristics of the turbidity current flow and of the emplaced deposit in terms of deposit thickness and spatial distribution of the sediment sizes. To study the effects of the sediment size characteristics of the deposit simulations are performed with uniform and non-uniform sediment sizes and different characteristic diameters.

The numerical results presented in Chapter 4 of this dissertation show that TC-SOLVER is able to capture the spatial and temporal evolution of the turbidity current as it enters the minibasin, reflects on the downstream flank creating an upstream migrating bore which eventually stabilizes. Downstream of the bore a sharp interface separates the turbidity current from the clear water above, as observed in laboratory experiments. In the cases of relatively large turbidity current relative to the size of the proximal basin (Basin II), or after significant deposition in the proximal basin, the current spills in the canyon connecting the two minibasin and reaches the distal basin (Basin IV).

In the simulations with uniform sediment the turbidity current spilling from Basin II to Basin IV is very small compared to the turbidity current released in Basin II. A comparison between the different conditions shows that the spilling current it is smallest in the simulations with relatively coarse sediment.

In the simulations with non-uniform sediment the turbidity current spilling from Basin II to Basin IV is generally larger than in the simulations with uniform material. In these simulations, relatively coarse sediment is trapped in Bain II and the fine sediment is transported further downslope by the spilling current and it reaches Basin IV.

Sedimentation in Basin II in the case of relatively fine sediment mostly occurs in the central part of the basin below the spill point. In the case of very fine sediment

(characteristic grain size of ~20 μm) the deposit thickness is nearly uniform in space. As the characteristic sediment size increases to 40 μm the majority of the deposit is still located at elevations that are smaller than the elevation of the spill point. In the case of uniform material, the deposit is nearly tabular and can be interpreted as what Prather et al. (2012) call low relief ponded apron. In the case of non-uniform sediment with geometric mean size of 40 μm, significant deposition occurs on the proximal flank of the basin at elevations that are lower than the elevation of the spill point. This depositional pattern may correspond to what Prather et al. (2012) call a high relief ponded apron.

As the characteristic sediment size increases up to ~80 μm, preferential deposition occurs on the proximal flank of Basin II at elevations that are higher than the elevation of the spill point. Interestingly, the deposits of the simulations with characteristic grain size equal to ~60 μm are characterized by sediment waves that resemble cyclic steps observed in laboratory experiments and in field data collected in submarine settings.

The spatial distribution of grain sizes in the emplaced deposits confirms that TC-SOLVER is able to capture some of the features of the minibasin deposits observed in the field, i.e. the Basin II deposit is generally coarser than the inlet sediment. In the simulation with characteristic grain size of 40 μm a pattern of downstream coarsening characterizes the deposit on the entrance flank and the deposit fines in the dip direction in the central part of the basin. A clear pattern of downstream fining characterizes the deposit in the simulations with relatively coarse material (60 μm and 80 μm), clearly showing preferential deposition of coarse sediment on the proximal flank.

These results show that the different flow characteristics between the runs with relatively fine and relatively coarse sediment, which resulted in the presence of a significant

reflection bore in the case of fine sediment, control the deposition pattern in intraslope minibasins.

Three-dimensional turbidity current simulations have been performed for the area of the Brazos-Trinity system that extends from Basin II to Basin III and Basin IV. A canyon connects Basin II and Basin III to the upstream part of the system, which is not modeled in this study. Overspill canyons connect Basin II and Basin III to Basin IV.

The objectives of this study are the investigation of the three dimensional effects of turbidity current magnitude relative to basin size, inlet conditions and sediment size distribution on the characteristics of turbidity current deposits emplaced in intraslope minibasins. Thus, different turbidity current magnitudes, sediment sizes and inlet geometries are considered to study the depositional pattern in Basin IV, i.e. the distal basin of the Trinity-Brazos system.

The main results of this numerical study is that turbidity current magnitude relative to the basin size play a significant control on the depositional pattern in intraslope minibasins. In the case of relatively small turbidity currents preferential deposition occurs on the proximal flank of the minibasin. In the case of relatively large turbidity currents relative to the basin size, preferential deposition occurs in the central and deep part of the basin.

Noting that in Basin IV the deposition occurs at elevations that are lower than the elevation of the spill point, and thus the deposits may be interpreted as ponded aprons (sensu Prather et al., 2012), this result suggests that relatively small turbidity currents relative to the basin size may tend to emplaced high relief ponded aprons, while large, strong currents may be responsible for the emplacement of low relief ponded aprons.

The analysis of the numerical results on the characteristics of the turbidity current flow reveals that the characteristics of the turbidity current reflection on the distal basin flank changes with the turbidity current magnitude and inlet condition. Further investigation on the characteristics of the pre- and post-reflection turbidity current hydrodynamics is necessary to link the flow characteristics to the observed depositional patterns.

In all the simulations, the grain size distribution of the emplaced deposit is coarsest where the deposit is thickest. The comparison between numerical results performed with a sediment size distribution specified in terms of 2 or 5 characteristic grain sizes and inlet volumetric concentrations of suspended sediment equal to 2% (2 characteristic grain sizes) and 5% (5 characteristic grain sizes) reveals different depositional patterns. The deposit of the simulation with 2 characteristic grain sizes is thickest where the initial minibasin bathymetry is deepest resulting in a nearly tabular deposit. On the contrary, in the simulations with 5 characteristic grain sizes the emplaced deposit has nearly uniform thickness with coarse material preferentially deposited downdip of the canyon exit(s). Further analysis of the flow hydrodynamics is necessary to explain this result and to use it to interpret the characteristics of minibasin deposits in the field.

REFERENCES

Abdulah K.C., 1995. T*he Evolution of the Brazos and Colorado Fluvial/ Deltaic Systems during the Late Quaternary: An Integrated Study, Offshore Texas*. Rice University, Houston, 284 p.

Alexander J., Morris S., 1994. *Observations on experimental, non-channelized, high-concentration turbidity currents and variations in deposits around obstacles*. Journal of Sedimentary Research, v. 64, p. 899–909.

Al Ja' Aidi O.S., McCaffrey W.D., Kneller B.C., 2004. *Factors influencing the deposit geometry of experimental turbidity currents: implications for sand-body architecture in confined basins*. In Lomas, S.A., and Joseph, P., eds., Confined Turbidite Systems. Geological Society of London, Special Publication 222, p. 45–58.

Amy L. A., McCaffrey W. D., Kneller B. C., 2004. *The influence of a lateral basin-slope on the depositional patterns of natural and experimental turbidity currents*. Geological Society, London, Special Publications, 221, 311-330.

Anderson, J.B., 2005. *Diachronous development of late Quaternary shelf- margin deltas in the northwestern Gulf of Mexico: Implications for sequence stratigraphy and deep-water reservoir occurrence*, in Giosan, L., and Bhattacharya, J.P., eds., Deltas—Concepts, Models, and Examples. SEPM, Special Publication 83, p. 257–278.

Ashida, K., M. Michiue, 1972. *Study on hydraulic resistance and bed load transport rate in alluvial streams*. Transactions, Japan Society of Civil Engineering, 206: 59-69 (in Japanese).

Badalini G., Kneller B., Winker C. D., 2000. *Architecture and processes in the Late Pleistocene Brazos-Trinity Turbidite System. Gulf of Mexico Continental Slope*. SEPM, Gulf Coast Section, 20th Annual Research Conference, Deep-Water Reservoirs of the World, Proceedings, p. 16–34.

Barley B., 1999. *Deepwater problems around the world*. Leading Edge, v. 18, p. 514-519.

Beaubouef R.T., Friedman S.J., Alwin B.W., 1998. *High resolution seismic/sequence stratigraphy of intra-slope basins, western Gulf of Mexico*. AAPG international conference and exhibition; abstracts. Tulsa, American Association of Petroleum Geologists, p. 1890.

Beaubouef R.T., Friedman, S.J., 2000. *High resolution seismic/sequence stratigraphic framework for the evolution of Pleistocene intra slope basins, western Gulf of Mexico: depositional models and reservoir analogs.* Gulf Coast Section, Society of Economic Paleontologists and Mineralogists, 20th Annual Research Conference, Deep-Water Reservoirs of the World, Dec. 3–6, p. 40–60.

Beaubouef, R.T., Abreu V., 2006. *Basin 4 of the Brazos-Trinity Slope System: anatomy of the terminal portion of an intra-slope low stand system tract*. Gulf Coast Association of Geological Societies Transactions, v. 56, p. 39-49.

Beaubouef R.T., Abreu V., Adair N.L., 2003a. *Ultra-High Resolution 3-D Characterization of Deep-Water Deposits-I: A New Approach to Understanding the Stratigraphic Evolution of Intra-Slope Depositional Systems*. AAPG Annual Meeting, May 14, 2003, Salt Lake City, Utah.

Beaubouef R.T., Van Wagoner J.C., Adair, N.L., 2003b. *Ultra-high resolution 3-D characterization of deep-water deposits II: Insights into the evolution of a submarine fan and comparisons with river deltas.* Search and Discovery Article # 40084.

Bohn IV C.W., Flemings P.B., Singerland R.L., 2012. Accommodation change during bypass across a late-stage in the shallow Auger Basin. Application of the Principles of Seismic Geomorphology to Continental-Slope and Base-of-Slope Systems: Case Studies from Seafloor and Near-Seafloor Analogues SEPM Special Publication No. 99, p. 225–242.

Booth J.R., Duvernay A.E., Pfeiffer D.S., Styzen M.J., 2000. *Sequence stratigraphic framework, depositional models, and stacking patterns of ponded and slope fan systems in the Auger Basin: central Gulf of Mexico slope*, in Weimer, P., Slatt, R.M., Coleman, J., Rosen, N.C., Nelson, H., Bouma, A.H., Styzen, M.J., and Lawrence, D.T., eds., Deep-Water Reservoirs of the World. Gulf Coast Section SEPM Foundation, 20th Annual Bob F. Perkins Research Conference, p. 82– 103.

Booth J.R., Dean M.C., Duvernay A.E., Pfeiffer D.S., Styzen M.J., 2003. *Paleo-bathymetric controls on the stratigraphic architecture and reservoir development of confined fans in the Auger Basin: central Gulf of Mexico slope.* Marine and Petroleum Geology, v. 6– 8, p. 563–586.

Bouma A.H., 1962. *Sedimentology of some flysch deposits: a graphic approach to facies interpretation.* Amsterdam, Elsevier, p. 168.

Bouma A.H., 1981. *Depositional sequences in clastic continental deposits, Gulf of Mexico*. Geo-Marine Letters, v. 1, p.115-121.

Bouma A.H., 1982. *Intraslope basins in the norther west Gulf of Mexico: a key to ancient submarine canyons and fans,* in Watkins J.S. and Drake C.L., eds., Studies in the Continental Margin Geology. AAPG Memoir 34, p. 567-581.

Bouma A.H., Bryant W.R., 1994. *Physiographic features on the northern Gulf of Mexico continental slope.* Geo-Marine Letters, v. 14, p. 252–263.

Brami T.R., Pirmez C., Archie C., Holman K.L. 2000. *Late Pleistocene deep-water stratigraphy and depositional processes, offshore Trinidad and Tobago.* In. Deep-Water Reservoirs of the World (Eds P. Weimer, R.M. Slatt, J. Coleman, N.C. Rosen, H. Nelson, A.H. Bouma, M.J. Styzen and D.T. Lawrence), pp. 104–115. Gulf Coast Section SEPM, Houston, TX.

Bryant W.R., Bryant J.R., Feeley M.H., Simmons G.R., 1990. *Physiography and bathymetric characteristics of the continental slope, northwest Gulf of Mexico*. Geo-Marine Letters, v. 10, p. 182-199.

Bursik M.I., Woods A.W., 2000. *The effects of topography on sedimentation from particle-laden turbulent density currents*: Journal of Sedimentary Research, v. 70, p. 53–63.

Cooper C., Wood J., Andrieux O., 2013. *Turbidity current measurements in the Congo Canyon.* In Offshore Technology Conference, OTC-23992-MS.

Damuth J.E., Kolla V., Flood R.D., Kowsmann R.O., Moonteiro M.C., Gorini M.A., Palma J.J.C., Belderson R.H., 1983. *Distributary channel meandering and bifurcation patterns on Amazon deep-sea fan as revealed by long-range side-scan sonar (GLORIA).* Geology, v. 11, p. 94–98.

Diegel F.A., Karlo J.F., Schuster D.C., Shoup R.C., Tauvers P.R., 1995. *Cenozoic structural evolution and tectonostratigraphic framework of the northern Gulf Coast continental margin,* in Jackson M.P.A., Roberts D.G., Snelson S. eds., Salt Tectonics: a global perspective. AAPG Memoir 65, p. 109-151.

Dietrich W.E., 1982. *Settling velocity of natural particles*. Water Resources Research, v. 18, p. 1626–1982.

Ferziger J. H., Peric M., 2002. *Computational methods for fluid dynamics*, 2nd Ed., Springer, New York.

García M., 1990. *Depositing and eroding sediment-driven flows: Turbidity Currents*. Ph.D. Dissertation., Univ. of Minnesota, Minneapolis. García, M., 1990. Depositing and eroding sediment-driven flows: Turbidity Currents. Ph.D. Dissertation., Univ. of Minnesota, Minneapolis.

García, M., G. Parker, 1991. *Entrainment of bed sediment into suspension.* Journal of Hydraulic Engineering, 117(4): 414-435.

Garcia M. H., 1993. *Hydraulic jumps in sediment-driven bottom currents*. Journal of Hydraulic Engineering, Vol. 119, No. 10, October 1993.

Gardner J.V., Field M.E., Twichell D.C., 1996. *Geology of the United States' Seafloor: The View from GLORIA.* Cambridge, U.K., Cambridge University Press, p. 364.

Haughton P.D.W., 1994. *Deposits of deflected and ponded turbidity currents, Sorbas Basin, Southeast Spain.* Journal of Sedimentary Research, v. 64, p. 233–246.

Henkes R. A., Flugt W. M, Hoogendoorn C. J., 1991. *Natural convection flow in a square cavity calculated with low-Reynolds number turbulence models*. Int. J. Heat Mass Transfer 34, 1543–1557.

Holman W.E., Robertson S.S., 1994. *Field development, depositional model, and production performance of the tubiditic ''J'' sands at Prospect Bullwinkle, Green Canyon 65 fields, outer-shelf Gulf of Mexico,* in Weimer, P., Bouma, A.H., and Perkins, B.F., eds., Submarine Fans and Turbidite Systems—Sequence Stratigraphy, Reservoir Architecture, and Production Characteristics. SEPM, Gulf Coast Section, Fifteenth Annual Research Conference, p. 139–150.

Huang H., Imran J., Pirmez C., 2005. *A numerical model of turbidity currents with a deforming bottom boundary.* Journal of Hydraulic Engineering 131 (4), 283–293.

Huang H., Imran J., Pirmez C., 2007. *Numerical modeling of poorly sorted depositional turbidity currents.* Journal of Geophysical Research 112 (C1) (URL http://www.agu. org/pubs/crossref/2007/2006JC003778.shtml).

Huang H., Imran J., Pirmez C., 2012. *The depositional characteristics of turbidity currents in submarine sinuous channels*. Marine Geology 329–331 (2012) 93–102.

Imran J., Parker G., Katopodes N., 1998. *A numerical model of channel inception on submarine fans*. J. Geophysical Research 103, 1219–1238.

Jobe Z.R., Lowe D.R., Morris W.R., 2012, *Climbing-ripple successions in turbidite systems: depositional environments, sedimentation rates and accumulation times.* Sedimentology, v. 59, p. 867–898.

Karim M. F., Kennedy J. F., 1982. *IALLUVIAL: A computer based flow and sediment routing model for alluvial streams and its application to the Missouri River*. Rep. 250, Iowa Inst. of Hydraul. Res., Iowa City.

Khan S. M., Imran J. 2008. *Numerical investigation of turbidity currents flowing through minibasins on the continental slope*. Society for Sedimentary Geology v. 78, p. 245-257.

Kneller B.C., Edwards D.A., McCaffrey W.D., Moore, R., 1991. *Oblique reflection of turbidity currents.* Geology, v. 19, p. 250–252.

Khan S.M., Imran J. (2008) *Numerical investigation of turbidity currents flowing through minibasins on the Continental slope*. J. Sed. Res., 78, 245–257.

Kneller B. C., Winker C. D. 2000. *Architecture and processes in the Late Pleistocene Brazos-Trinity Turbidite System, Gulf of Mexico Continental Slope*. SEPM, Gulf Coast Section, 20th Annual Research Conference, Deep-Water Reservoirs of the World, Proceedings, p. 16–34.

Lamb M.P., Hickson T., Marr J.G., Sheets B., Paola C., Parker G., 2004. *Surging versus continuous turbidity currents: flow dynamics and deposits in an experimental intraslope minibasin.* Journal of Sedimentary Research, v. 74, p. 148–155.

Lamb M.P., Toniolo H., Parker G., 2006. *Trapping of continuous turbidity currents by intraslope minibasins.* Sedimentology, v. 53, p. 147–160.

Lesser G.R., Roelvink J.A., Van Kester J., Stelling G.S., 2004. *Development and validation of a three-dimensional morphological model.* Coastal Engineering, 51(8-9):883–915.

Lesser, G.R., 2009. *An approach to medium-term coastal morphological modelling*. Ph.D. thesis, UNESCO-IHE and Delft Technical University, Delft. CRC Press/Balkema. ISBN 978-0-415-55668-2.

Liu, J.Y., Bryant, W.R., 2000. *Sea floor morphology and sediment paths of the northern Gulf of Mexico deep-water, in Bouma,* A.H., and Stone, C.G., eds., Fine- Grained Turbidite Systems. American Association of Petroleum Geologists, Memoir 72, and SEPM, Special Publication 68, p. 33–45.

Lowe D.R., 1982. *Sediment gravity flows: II. Depositional models with special reference to the deposits of high-density turbidity currents.* Journal of Sedimentary Petrology, v. 52, p. 279–297.

Mahaffie, M.J., 1994. *Reservoir classification for turbidite intervals at the Mars discovery, Mississippi Canyon 807, Gulf of Mexico*, in Weimer, P., Bouma, A.H., and Perkins, B.F., eds., Submarine Fans and Turbidite Systems—Sequence Stratigraphy, Reservoir Architecture, and Production Characteristics. SEPM, Gulf Coast Section, Fifteenth Annual Research Conference, p. 233–244.

Malinverno A., Ryan W.B.F., Auffret, G., Pautot G., 1988. *Sonar images of the path of recent failure events on the continental margin off Nice, France*, in Clifton, E.H., ed., Sedimentologic Consequences of Convulsive Geologic Events. Geological Society of America, Special Paper 229, p. 59–76.

Mallarino G., Beaubouef R.T., Droxler V.A., Labeyrie L., 2006. *Sea level influence on the nature and timing of a minibasin sedimentary fill (northwestern slope of the Gulf of Mexico).* AAPG Bulletin, v. 90, no. 7, p. 1089–1119.

McGee D.T., Bilinski P.W., Gary P.S., Pfeiffer D.S., Sheiman J.L., 1994, *Geologic models and reservoir geometries of Auger Field, deep-water Gulf of Mexico*, in Weimer, P., Bouma, A.H. and Perkins, B.F. eds., Submarine Fans and Turbidite Systems: SEPM Foundation, Gulf Coast Section, Fifteenth Annual Research Conference, p. 245–256.

Mutti E., 1992. *Turbidite and stones*. San Donato Milanese, Agip - Istituto di Geologia, Università di Parma, p. 275.

Normark W.R., Posamentier H., Mutti E., 1993. *Turbidite systems: state of the art and future directions.* Reviews of Geophysics, 31, 2. P. 91-116.

Parker G., Fukushima Y., Pantin H. M., 1986. *Self-accelerating turbidity currents*. Journal of Fluid Mechanics, v. 171, 145–181.

Parker G., 1996. *Some speculations on the relation between channel morphology and channel-scale flow structures*. In: Proceedings, Coherent Flow in Open Channels. John Wiley and Sons, Ltd.

Patacci M., Haughton P. D.W., McCaffrey W. D., 2015. *Flow behavior of ponded turbidity currents.* Journal of Sedimentary Research, v. 85, 885–902.

Pettingill H.S., 1998a. *World turbidites, 1, Turbidite plays immaturity means big potential remains.* Oil and Gas Journal, v. 96, p. 106-112.

Pettingill H.S., 1998b. *World turbidites, 2, Lessons learned from 43 turbidite giant fields.* Oil and Gas Journal, v. 96, p. 93-95.

Pirmez C., Beaubouef R.T., Friedman S.J., Mohrig D.C., 2000. *Equilibrium profile and base level in submarine channels: Examples from late Pleistocene systems and implications for the architecture of deep-water reservoirs.* Gulf Coast Section. SEPM, 20th Annual Research Conference, Deep-Water Reservoirs of the World, December 3–6, p. 782–805.

Pirmez C., Prather B. E., Mallarino G., O'Hayer W. W., Droxler Andre W., Winker C. D., 2012. *Chronostratigraphy of the Brazos–Trinity depositional system, western Gulf of Mexico: implications for deep-water depositional models*. SEPM Special Publication No. 99, p. 111–143.

Prather B. E., Booth J. R., Steffens G. S., Craig P. A., 1998. *Classification, Lithologic Calibration, and Stratigraphic Succession of Seismic faces of intraslope Basins Deep-Water Gulf of Mexico*. AAPG Bulletin, v. 82, No. 5A (May 1998 Part A), p. 701–728.

Prather B.E., 2000. *Calibration and visualization of depositional process models for above-grade slopes: a case study from the Gulf of Mexico*. Marine and Petroleum Geology v. 17(5):619-638.

Prather B. E., Pirmez C., Winker C. D., 2012. *Stratigraphy of linked intraslope basins: Brazos–Trinity system Western Gulf of Mexico.* SEPM Special Publication No. 99, SEPM (Society for Sedimentary Geology), ISBN 978-1-56576-304-3, p. 83–109.

Pratson, L. F., and W. B. F. Ryan, 1994. *Pliocene to Recent infilling and subsidence of intraslope basins offshore Louisiana*. AAPG Bulletin, v. 78, no. 10, p. 1483–1506.

Rodi, W., 1984. *Turbulence models and their applications in hydraulics*, International Association for Hydraulic Research, Delft, The Netherlands, Monograph.

Roelvink J.A., 2006. *Coastal morphodynamic evolution techniques*. Coastal Engineering, 53(2-3):277–287.

Rottman, J.W., Simpson, J.E. and Hunt, J.C.R., 1985.*Unsteady gravity current flows over obstacles: some observations and analysis related to the Phase II trials*. J. Hazardous Mater., 11, 325–340.

Satterfield W. M., Behrens E. W., 1990. *A late Quaternary canyon/channel system, Northwest Gulf of Mexico Continental slope.* Marine Geology, v. 92, p. 54-67.

Schollnberger, E., Vail, P.R. 1999. Seismic sequence stratigraphy of the lower Congo, Kwanza, and Benguela basins, offshore Angola, Africa. Am. Assoc. Pet. Geol. Bull., 83, 1338.

Sequeiros, O. E., Cantelli A., Viparelli E., White J. D. L., García M. H., Parker G., 2009a. *Modeling turbidity currents with non-uniform sediment and reverse buoyancy.* Water Resour. Res., 45, W06408, doi:10.1029/ 2008WR007422.

Sequeiros, O. E., Naruse H., Endo N., García M. H., Parker G., 2009b. Experimental study on self-accelerating turbidity currents, J. Geophys. Res., 114, C05025, doi:10.1029/2008JC005149.

Sequeiros, O. E., Spinewine B., Beaubouef R. T., Sun T., García M. H., Parker G., 2010. *Characteristics of velocity and excess density profiles of saline underflows and turbidity currents flowing over a mobile bed.* J. Hydraul. Eng., 136(7), 412–433, doi:10.1061/(ASCE)HY.1943-7900.0000200.

Sequeiros O.E., 2012. *Estimating turbidity current conditions from channel morphology: a Froude number approach*. Journal of Geophysical Research, v. 117.

Sinclair H.D., 2000. *Delta-fed turbidites infilling topographically complex basins: a new depositional model for the Annot Sandstones, SE France*. Journal of Sedimentary Research, v. 70, p. 504–519.

Sinclair H.D., Tomasso M., 2002. *Depositional evolution of confined turbidite basins.* Journal of Sedimentary Research, v. 72, no. 4, p. 451-456.

Sumner H. S., Robinson B. A., Dirks W. K., Holliday J. C., 1991. *Morphology and evolution of salt/mini-basin systems: lower slope and upper slope, central offshore Louisiana* (abs.): AAPG Bulletin, v. 75, no. 6, p. 677.

Suter J.R., Berryhill H.L., 1985. *Late Quaternary shelf-margin deltas, northwest Gulf of Mexico.* American Association of Petroleum Geologists, Bulletin, v. 69, p. 77–91.

Toniolo H., Parker G., Voller V., Beaubouef R.T., 2006a. *Depositional turbidity currents in diapiric minibasins on the continental slope: experiments - numerical simulations and upscaling.* Journal of Sedimentary Research, v. 76, p. 798–818.

Toniolo H., Lamb M., Parker G., 2006b. *Depositional Turbidity Currents in Diapiric Minibasins on the Continental Slope. Formulation and Theory.* Journal of Sedimentary Research, v. 76, 783–797.

Van Andel T.H., Komar P.D., 1969. *Ponded sediments of the Mid-Atlantic Ridge between 22u and 23u north latitude*. Geological Society of America, Bulletin, v. 80, p. 1163–1190.

Violet J., Sheets B., Pratson L., C. Paola, Beaubouef R., Parker G., 2005, *Experiment on turbidity currents and their deposits in a model 3d subsiding minibasin.* Journal of sedimentary research, v. 75, 820-843.

Viparelli E., Sequeiros O. E., Cantelli A., Wilcock P. R., Parker G., 2010. *River morphodynamics with creation/consumption of grain size stratigraphy 2: numerical model*. Journal of Hydraulic Research, 48:6, 727-741.

Weimer P., Link M.H., 1991. *Global petroleum occurrences in submarine fans and turbidite systems.* Weimer P. and Link M.H. (eds.) Seismic Facies and Sedimentary Processes of Submarine Fans and Turbidite Systems. Springer, New York, 9-67.

Winker C.D., 1996. *High-resolution seismic stratigraphy of a late Pleistocene submarine fan ponded by salt-withdrawal mini-basins on the Gulf of Mexico continental slope*. 28th Annual Offshore Technology Conference, Proceedings, p. 619–628.

Woods A.W., Bursik M. I. Bukatov A.V., 1998. *The interaction of ash flows with ridges*. Bull. Volcanol., 60, 38– 51.

Worrall D. M., Snelson S., 1989. *Evolution of the northern Gulf of Mexico basin, with emphasis on Cenozoic growth faulting and the role of salt*. A. W. Bally and A. R. Palmer, eds. The geology of North America—an overview: Geological Society of America, p. 97–138.